



저작자표시-비영리-변경금지 2.0 대한민국

이용자는 아래의 조건을 따르는 경우에 한하여 자유롭게

- 이 저작물을 복제, 배포, 전송, 전시, 공연 및 방송할 수 있습니다.

다음과 같은 조건을 따라야 합니다:



저작자표시. 귀하는 원저작자를 표시하여야 합니다.



비영리. 귀하는 이 저작물을 영리 목적으로 이용할 수 없습니다.



변경금지. 귀하는 이 저작물을 개작, 변형 또는 가공할 수 없습니다.

- 귀하는, 이 저작물의 재이용이나 배포의 경우, 이 저작물에 적용된 이용허락조건을 명확하게 나타내어야 합니다.
- 저작권자로부터 별도의 허가를 받으면 이러한 조건들은 적용되지 않습니다.

저작권법에 따른 이용자의 권리는 위의 내용에 의하여 영향을 받지 않습니다.

이것은 [이용허락규약\(Legal Code\)](#)을 이해하기 쉽게 요약한 것입니다.

[Disclaimer](#)

공학박사학위논문

**A study on the synthesis and electrical
properties of one-dimensional Zinc-based
semiconductor structures**

1 차원 아연계 반도체 구조체의 합성
및 전기적 성질에 관한 연구

2017년 8월

서울대학교 대학원

재료공학부

김 정 한

**A study on the synthesis and electrical
properties of one-dimensional Zinc-based
semiconductor structures**

1 차원 아연계 반도체 구조체의 합성
및 전기적 성질에 관한 연구


지도교수 오 규 환

이 논문을 공학박사학위논문으로 제출함
2017년 6월

서울대학교 대학원
재료공학부
김 정 한

김정한의 공학박사 학위논문을 인준함
2017년 7월

위	원	장	한	홍	남	(인)	
부	위	원	장	오	규	환	(인)
위		원	선	정	윤	(인)	
위		원	정	연	웅	(인)	
위		원	정	희	석	(인)	



Abstract

A study on the synthesis and electrical properties of one-dimensional Zinc-based semiconductor structures

Jung Han Kim

Department of Materials Science and Engineering

The Graduate School

Seoul National University

Nanoscale one-dimensional (1D) structures have stimulated great interest recently owing to their unique electronic, optical, and mechanical properties as a result of their low-dimensionality and the quantum confinement effect. Their potential applications as building blocks, interconnects and functional units in electronic and optoelectronic devices and sensors have also been demonstrated.

Even though there are ongoing efforts to realize nano-devices using 1D nanowires building-block, the research on the control methods of chemical composition, structure, and size at nanoscale are still required with rational synthesis including reproducibility.

The work described in this thesis focuses on understanding the basic synthesis of Zinc-based semiconductor structures of interest for growth behavior and hetero-structure. The goal is to investigate nanostructures relevant to specific growth conditions, and then through careful analysis of these structures, gain new insights into the growth behavior governing their nucleation and growth.

In particular, this work is focused on the growth mechanism of ZnS nanowires, the analysis of nanostructures using 3D TEM tomography and 3D printing, the optical properties of ZnS / diamond-like carbon core-shell heterostructure nanowires and the electrical characteristics of a ZnO microwire.

Firstly, we report sublimation of crystalline ZnS nanowires at elevated temperatures in vacuum imaged by in situ transmission electron microscopy. The ZnS nanowires, 20-80 nm in diameter, were heated using a controllable heating system, and their melting temperature was studied. The results showed a significant reduction of the melting temperature of about 400°C, depending on the diameter of the nanowire, compared to the bulk melting point of 1185 °C. In addition, the in-situ heating experiment showed that the SLV process proceeds exactly in the reverse direction of VLS, and the synthesis mechanism of Ag₂S catalyzed ZnS NW was investigated.

Secondly, the work focus on recent developments in the field of 3D imaging at the nanoscale, when applied to nanomaterials and nanostructures. I demonstrate that recent progress in the use of electron microscopy techniques based on tomography allows one to fill the gap between the development of new materials and their structures and characterization. A special emphasis is put on two new 3D approaches: quantitative and analytical 3D tomography.

Electronic tomography studies the 3D form of nanomaterials and provides a comprehensive insight into the structure and interface of nanomaterials. Here, we report 3D characteristics of ZnS nanostructures using Ag catalyst using electron tomography using bright field image.

Thirdly, we fabricated ZnS/diamond-like carbon (DLC) core-shell heterostructure nanowire using a simple two-step process: the vapor-liquid-solid method combined with radio frequency plasma enhanced chemical vapor deposition (rf PECVD). As a core nanowire, ZnS nanowires with face-centered cubic structure were synthesized with a sputtered Au thin film, which exhibit a length and a diameter of $\sim 10\mu\text{m}$ and $\sim 30\text{-}120\text{nm}$. After rf PECVD for DLC coating, The length and width of the dense ZnS/DLC core-shell nanowires were a range of $\sim 10\mu\text{m}$ and $50\text{-}150\text{nm}$, respectively. In addition, ZnS/DLC core-shell nanowires were characterized with scanning transmission electron microscopy. From the results, the products have flat and uniform DLC coating layer on ZnS nanowire in spite of high residual stress induced by the high sp^3 fraction. To

further understanding of the DLC coating layer, Raman spectroscopy was employed with ZnS/DLC core-shell nanowires, which reveals two Raman bands at 1550 cm^{-1} (G peak) and 1330 cm^{-1} (D peak). Finally, we investigated the infrared transmittance property using Fourier transform infrared spectrometry. The results confirm that products increased the infrared transmittance property of the ZnS nanowires by 1.1-2.8%.

Lastly, we investigate the influence of the contact interface on the electrical properties of a ZnO microwire (MW) with silver (Ag) paste electrodes. The ZnO MW devices that are produced by dropping Ag paste on the ZnO MW surface followed by a curing step at an elevated temperature exhibit linear current-voltage characteristics, whereas the devices with Ag paste electrodes dropped upon a heated ZnO MW exhibit a non-linear electrical behavior. The results of electron microscopy and cathodoluminescence show the effect of the contact interface properties, such as interfacial defects and/or charge trap sites, between the ZnO MW and Ag paste electrodes. An energy band model is suggested to explain the charge transport mechanism for different types of Ag contacts on the ZnO MW.

Keywords: Nanotechnology, One-Dimensional (1D) Nanostructure, Nanowires, Vapor-Liquid-Solid (VLS), Vapor-Solid (VS), Growth Behavior, Heterostructure, Diamond-like Carbon(DLC), Zinc Sulfide (ZnS), Zinc Oxide, Focused Ion Beam (FIB), Scanning Electron Microscopy (SEM), Raman Spectroscopy, High-resolution Transmission Electron Microscopy (HRTEM), 3D TEM Tomography, 3D Printing, Fourier-transform Infrared (FT-IR), Photoluminescence (PL), Radio Frequency Plasma Enhanced Chemical Vapor Deposition (R.F- PECVD), Energy Dispersive Spectroscopy (EDS), Cathodoluminescence

Student Number: 2007-20690

Table of Contents

Abstract	I
Table of Contents	VI
List of Tables	XII
List of Figures	XIII

Chapter 1.

Introduction

1.1 Nanotechnology	1
1.2 Nanomaterials	10
1.2.1 0D Nanostructure-Quantum Dots and Nanoparticles	14
1.2.2 Two-Dimensional Nanostructure – Thin Films	17
1.3 II-VI semiconductors	19
1.3.1 Zinc Oxide – ZnO	20
1.3.2 Zinc Sulfide – ZnS	22

1.4 Thesis motivation	23
1.5 References	25

Chapter 2.

One-Dimensional Nanostructures

2.1 General Properties of Nanomaterials	29
2.2 Definition and Types of 1-D Nanostructure	32
2.3 Top-Down and Bottom-Up Approach	36
2.4 Nanowire Synthesis and Theory	40
2.4.1 Vapor Synthesis	42
2.4.1.1 Vapor-liquid-solid growth	42
2.4.1.2 Vapor-solid growth	47
2.4.1.3 Oxide-assisted growth	48
2.4.1.4 Carbothermal reactions	52
2.4.2 Solution Based Growth of Nanowires	53
2.4.2.1 Template-based synthesis	53
2.4.2.2 Anisotropic crystal structures	57
2.4.2.3 Solution-liquid-solid process	57
2.4.2.4 Solvothermal synthesis	59
2.5 References	60

Chapter 3.

Vapor–liquid–solid growth mechanism of Ag₂S catalyzed ZnS nanowires

3.1 Introduction	63
3.2 Experimental	66
3.2.1 Synthesis of ZnS nanowires	66
3.2.2 Characterization method	68
3.3 Results and Discussion	69
3.3.1 Characterization of ZnS nanowires	69
3.3.2 Structural analysis of ZnS nanowires	71
3.3.3 In-situ heating of ZnS nanowire	75
3.3.4 Growth mechanism	78
3.4 Conclusion	81
3.5 References	82

Chapter 4.

Visualization of Three-Dimensional Morphology of Hierarchically-Assembled ZnS Nanostructures by Corroborated Electron Tomography and 3D Printing

4.1 Introduction	88
4.2 Experimental section	90
4.2.1 Synthesis and characterization	90
4.2.2 TEM tomography and 3D printing	93
4.3 Results and Discussion	95
4.3.1 Morphology of ZnS nanostructure	95
4.3.2 Structural Analysis of ZnS nanostructure	98
4.3.3 3D TEM tomography	101
4.3.4 Growth mechanism of ZnS nanostructures	104
4.4 Conclusion	107
4.5 References	108

Chapter 5.

Fabrication and characterization of ZnS/ diamond-like carbon core-shell nanowires

5.1 Introduction	111
5.1.1 The structure and properties of diamond-like carbon	111
5.1.2 Motivation	119
5.2 Experimental Procedure.....	121

5.2.1 Synthesis of ZnS/DLC core-shell nanowires.....	121
5.2.2 Characterization method	123
5.3 Results and Discussion	124
5.3.1 Structural analysis of ZnS/DLC core-shell nanowires	124
5.3.2 Chemical analysis of ZnS/DLC core-shell nanowires	129
5.4 Conclusion	133
5.5 References	134

Chapter 6.

Influence of the contact interface on the electrical characteristics of a ZnO microwire with silver paste electrodes

6.1 Introduction	137
6.2 Experimental Procedure.....	140
6.2.1 Synthesis and the formation process of ZnO MW devices	140
6.2.2 Characterization method	143
6.3 Results and Discussion	144
6.3.1 I-V characteristics of ZnO MW devices	145
6.3.2 Structural Analysis of ZnO MW devices	147

6.3.3 Energy band diagrams	155
6.4 Conclusion	157
6.5 References	158

Chapter 7.

Total Conclusion	165
-------------------------------	------------

요약 (국문초록)	169
-----------------	-----

LIST OF TABLES

- Table 2.1 Size-dependent surface energy variation of NaCl (1g).
- Table 2.2 Classifying nanostructure fabrication techniques.
- Table 5.1 Mechanical properties of DLC film evaluated with
Diamond and Graphite for comparison.
- Table 5.2 Various general applications of diamond-like carbon film.

LIST OF FIGURES

- Figure 1.1 A) Simple energy band diagram of a single free atom representing a single potential energy state. (B) Corresponding broader energy bands that appear in larger bulk materials available to different countries at each level.
- Figure 1.2 Schematic illustrating color change in a quantum dot resulting from a shift in possible energy states corresponding to size change.
- Figure 1.3 Graph illustrating the exponential growth of IC transistors according to Moore's Law from 1971 to 2000.
- Figure 1.4 a), (b) SEM image of gecko head showing nano-sized setae small enough to operate using van der Waals force as an adhesive; (c) a color image of bacteria with magnetic nanowire particles inside used as a compass to aid the direction of the bacteria; (d) SEM image of a molecular motor used to move in nanometer increments along a protein track within the cytoplasm of the cell.

Figure 1.5 Nanomaterials have been used unknowingly in stained glass by grinding up gold and silver nanoparticles to small sizes. This figure shows SEM images of gold and silver nanoparticles with sizes ranging from 25 nm to 100 nm. Both gold and silver change their color significantly with size. Silver also can change its color depending on its shape as seen in the difference between the spherical and prismatic 100 nm silver nanoparticles.

Figure 1.6 This vial contains a solution with monodisperse CdSe quantum dots of different sizes. On the left side, there are small quantum dots ranging from blue to red.

Figure 1.7 ZnO wurtzite crystal structure.

Figure 2.1 Figure 2.1 SEM images of nanomaterial classifications.

Figure 2.2 Overview of the bottom-up paradigm for nanotechnology.

Figure 2.3 (a) Schematic illustration of vapor-liquid-solid growth mechanism including three stages. (I) alloying, (II) nucleation, (III) axial growth. Three stages are projected onto the conventional Au-Ge phase diagram; (b) shows

the compositional and phase evolution during the nanowire growth process.

Figure 2.4 In-situ TEM images recorded during the process of nanowire growth. (a) Au nanoclusters in solid state at 500 °C; (b) alloying initiated at 800 °C, at this stage Au exists mostly in solid state; (c) liquid Au/Ge alloy; (d) the nucleation of Ge nanocrystal on the alloy surface; (e) Ge nanocrystal elongates with further Ge condensation and eventually forms a wire (f).

Figure 2.5 TEM images of (a) Si nanowire nuclei formed on the Mo grid and (b), (c) initial growth stages of the nanowires.

Figure 2.6 Schematic diagram of the nucleation and growth mechanism of Si nanowires. The parallel lines indicate the [112] orientation. (a) Si oxide vapor is deposited first and forms the matrix within which the Si nanoparticles are precipitated. (b) Nanoparticles in a preferred orientation grow fast and form nanowires. Nanoparticles with non-preferred orientations may form chains of nanoparticles.

- Figure 2.7 TEM image of an anodic alumina membrane (AAM).
- Figure 2.8 Schematic diagram showing the formation of nanowires by templating against mesostructures which are self-assembled from surfactant molecules. (a) Formation of cylindrical micelle; (b) formation of the desired material in the aqueous phase encapsulated by the cylindrical micelle; (c) removal of the surfactant molecule with an appropriate solvent to obtain an individual nanowire.
- Figure 2.9 Schematic illustration showing the growth of a nanowire through the solution-liquid-solid mechanism.
- Figure 3.1 (a) XRD pattern of ZnS nanowires. The peaks are identified with a wurtzite 6H ZnS structure with lattice constants $a = 3.823\text{\AA}$, $c = 18.743\text{\AA}$. (b) Low magnification SEM image of Ag₂S catalyzed ZnS nanowires. Inset in (b) is high-magnification SEM image.
- Figure 3.2 (a) A bright field TEM image of Ag₂S catalyzed ZnS nanowires. (b) HR-STEM image of a ZnS nanowire with a catalytic Ag₂S tip growing along [0001] direction. The

spacing between adjacent lattice fringes is 0.312nm. (c), (d) EDS spectrum recorded on the ZnS nanowire (Point A) and the Ag₂S tip (Point B), respectively. HR-STEM image of ZnS nanowire with corresponding EDS line-scan profile along the growth direction. (Blue: Zn, Red: Ag, Yellow: S) (e) STEM image and high resolution STEM-EDS elemental mappings of (f) Zn, (g) S and (h) Ag.

Figure 3.3 TEM images of ZnS nanowire: Cross-sectional TEM images, and high-resolution TEM image of ZnS nanowire. (a) ZnS nanowire with a hexagonal cross-section. (b), (c) HAADF-STEM characterization of the (a) and elemental mapping of Zn (blue) and S (yellow) (d) A high-resolution STEM image obtained from a cross-section of a ZnS nanowire and the corresponding FFT pattern indexed to wurtzite ZnS nanowire show that a ZnS nanowire grows along a [0001] direction. Inset in (d) is illustration of ZnS atomic structure (blue, Zn; yellow, S) (e) Simulated model

illustrates the atomic structure of the ZnS nanowire (blue, Zn; yellow, S)

Figure 3.4 Representative frames from movies of nanowire heating experiments (a) TEM image of as-grown Ag₂S catalyzed ZnS nanowire taken at room temperature prior to the in-situ annealing experiments. (b) TEM images showing a ZnS nanowire encapsulated in carbon shells during in-situ annealing at temperature between room temperature and 480 °C. (c) Exchange of material across the ZnS nanowire/liquid drop interface after the assembly of the shell and the melting of the alloy Zn-S-Ag nanoparticle. (d-f) A pure ZnS nanowire dissolves and evaporates into nanoparticle (Zn-S-Ag droplet) while the diameter of the wire simultaneously decreases. (g) In-situ assembly of the carbon tube.

Figure 3.5 Growth and dissolution mechanisms of Ag₂S catalyzed ZnS nanowire: (a) vapor–liquid–solid growth; (b) solid–liquid vapor–dissolution.

Figure 4.1 (a) The schematic diagram of the two distinctive grow zones inside the quartz tube for the synthesis of ZnS nanostructures by the MOCVD method. SEM images of as-synthesized ZnS nanostructures formed in zone 1 and 2. (b) ZnS nanowires. (c) ZnS nanostructures. The insets are high-magnification SEM images of ZnS nanostructures.

Figure 4.2 (a) XRD pattern of ZnS nanostructures. The peaks are identified with a wurtzite 2H ZnS structure with lattice constants $a = 3.836 \text{ \AA}$, $c = 6.277 \text{ \AA}$. (b) A bright field TEM image of ZnS nanostructure. (c) STEM image and high resolution STEM-EDS elemental mappings of Zn, S and Ag. (d) HR-STEM image of a ZnS nanostructure with a catalytic Ag_2S tip growing along [002] direction. The spacing between adjacent lattice fringes is 0.314 nm . (e) Cross-sectional TEM images between ZnS nanowire and nanoparticle. (f) HR-STEM image between ZnS nanowire and nanoparticle. (g) GPA simulation map.

Figure 4.3 Illustration of TEM tomography data acquisition, 3D reconstruction and 3D printing process. Series of 2D

images acquired of ZnS nanostructure at different viewing angles. 2D projected images combined into image stack ordered by viewing angle. Tilt series is aligned, and reconstruction algorithm is applied to produce 3D reconstruction of ZnS nanostructure. The ZnS nanostructure was output using 3d printing

Figure 4.4 Different angles BF TEM images of a tomographic series recorded from the ZnS nanostructure.

Figure 4.5 Visualizations: from 2D to 3D at nanoscales to 3D at macroscales.

Figure 4.6 Growth mechanism of ZnS nanostructure.

Figure 5.1 Exist in three hybridization of carbon with different allotropic forms as sp^1 , sp^2 and sp^3 .

Figure 5.2 Ternary phase diagram of amorphous carbons. The three corners correspond to diamond, graphite, and hydrocarbons, respectively.

Figure 5.3 Various industrial applications of diamond-like carbon film such as coating for IR window of Tank, Infrared missile, VTR head drum, computer hard disk and stent.

Figure 5.4 X-ray diffraction pattern of ZnS/DLC core-shell nanowires.

Figure 5.5 (a) Low-magnification SEM image of ZnS/DLC core-shell nanowires (inset: SEM image of as-synthesized ZnS nanowires. Scale bar is $1\mu\text{m}$.). (b) High-magnification SEM image of ZnS/DLC core-shell nanowires (inset: enlarged SEM image of as-synthesized ZnS nanowires. Scale bar is 100nm .).

Figure 5.6 (a) The low-magnification TEM image of a ZnS/DLC nanowire. (b) HRTEM image of ZnS/DLC core-shell nanowires revealing growth along the $[111]$ direction (inset: corresponding FFT pattern obtained by $[11\bar{0}]$ zone axis). (c) ADF-STEM image of ZnS/DLC core-shell nanowires with corresponding EDS line-scan profile along the width direction (Red: Zn, Blue: S, Green: C). (d) EDS spectrum of (c).

- Figure 6.1 Schematic illustrations depicting the formation process of ZnO MW devices with two different types of Ag paste contacts.
- Figure 6.2 Current (I)-voltage (V) characteristics of (a) type A and (b) type B devices. Log-log plots of I-V characteristics of (c) type A and (d) type B devices.
- Figure 6.3 SEM images of the Ag paste electrode formed at the end of the ZnO MW for (a) type A and (b) type B devices.
- Figure 6.4 Cross-sectional SEM images of ZnO MWs taken from (a) type A and (c) type B devices with corresponding EDS mapping data (b) of (a) and (d) of (c).
- Figure 6.5 Cross-sectional bright field TEM images of (a) type A and (b) type B devices corresponding to dark field TEM images (c) of (a) and (d) of (b).
- Figure 6.6 Cathodoluminescence spectra for (a) type A and (b) type B devices.
- Figure 6.7 Schematic illustrations and corresponding energy band diagrams depicting two different types of electrical

contacts between Ag paste electrodes and the ZnO MW.

Chapter 1.

Introduction

This chapter is intended to provide a framework in which the proposed studies are conducted. It is intended to be used extensively while providing a broad view of the field of nanomaterials. This chapter has been divided into discussions on nanotechnology and its directions, nanomaterials and II-VI semiconductors.

1.1 Nanotechnology

The term "nano" is derived from the Greek word dwarf. It is used to represent today's prefix nano - unit billions. Thus, nanometers are about one-tenth of the width of a human hair, or about 1/1000 of the hair, and the material generally contains several atomic lengths. If 'nano' is the only unit, what is nanotechnology? Wikipedia, a popular open source-based Internet site, defines nanotechnology as follows.

“Nanotechnology is research to control substances at the atomic or molecular level. In general, nanotechnology is related to developing structures and structures with sizes that are less than 100 nanometers in size.”[1]

This definition is surprisingly accurate. However, experts in this field are in the nanometer range for nanotechnology to be categorized as nanomaterials,

dealing with the creation, engineering, manipulation, and utilization of nanomaterials for systems and devices. Nanoscience, a field close to nanotechnology, can be defined as a search to understand the behavior of these materials and / or the underlying principles that apply to the application of such information to basic scientific questions.

One of the most cited definitions in nanotechnology in this regard is:

“The term “nanotechnology” means the science and technology that will enable one to understand, measure, manipulate and manufacture at the atomic, molecular, and the supermolecular levels, aimed at creating materials, devices, and systems with fundamentally new molecular organization, properties, and functions.”[2]

It is explained that this definition corresponds precisely to three important points: scale, function and originality.

Nanotechnology has made great efforts in the 20th century. The emergence of nanotechnology is initiated and accelerated by several scientific events. Of these events, the development of electron microscopy, the observation of new structures, and the growth of mathematical computational models to understand nanoscale phenomena are worth noting in the 20th century.

The emergence of upgraded electron microscopes and the development of quantum mechanics provided the basis for the first exploration of new

properties of nanomaterials, and the development of electron microscopy began in the 20th century. The first electron microscopy was initiated by Louis de Broglie and was continually developed in 1931 by Ernst Ruska and colleagues. (Ruska was awarded a physics Nobel in 1987). Continuing efforts to develop imaging tools, the latest electron microscope has a resolution of less than 1 angstrom. The growth of such electron microscopy allows scientists to understand the new nanomaterial structure, the ability to examine the composition was given. With this powerful imaging tool, many scientists were able to visualize phenomena such as precipitation, defects, and configuration

The first discovery of the properties of new nanomaterials was the quantum dot. Physicists have studied the ideal case of a single particle of very small size compared to the Bohr bulk radius.[3] The Bohr radius is a constant representing the size of an electron orbital around an unknown hydrogen atom nucleus. The size of the orbit consists of the attractive original strength between charged particles in the opposite direction and the repulsive force due to the momentum of electrons around the nucleus. The answer to the Schrodinger equation is that the electrons in the ground state can have only a certain "quantized" value of energy. These distinct orbits can be superimposed on a wide "energy band" because a large number of atoms are taken together. Figure 1.1 shows the difference between the narrow quantization energy level of a single free atom and a larger energy "band" than observed in molecular clusters and solids.

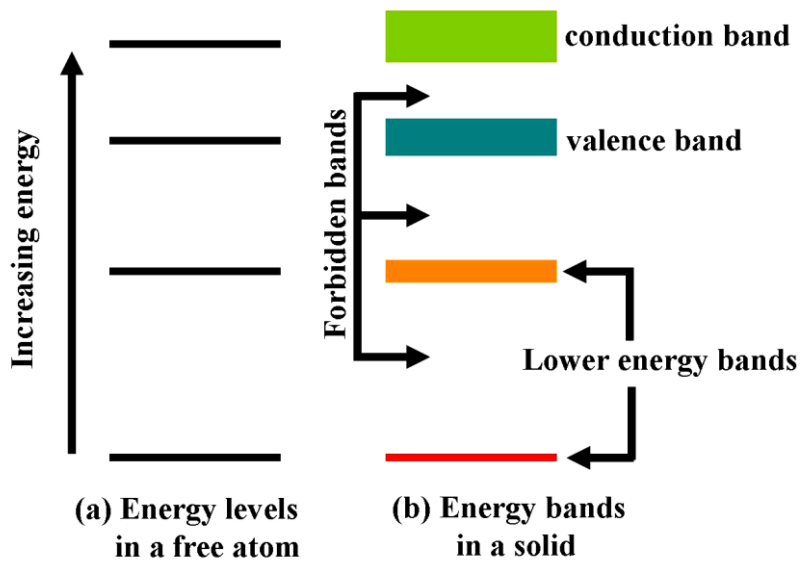


Figure 1.1 (A) Simple energy band diagram of a single free atom representing a single potential energy state. (B) Corresponding broader energy bands that appear in larger bulk materials available to different countries at each level.

Scientists have studied that if the particle has a size of about the Bohr radius, the energy band of the bulk material will be reduced to a quantized energy level like atoms, and the atomic effect will increase. Quantum dots were able to visualize from the theoretical potential wells to particles in a similar way of the Schrodinger equation. Quantum effects were first discovered by Bell Lab scientists in the CdSe study. According to quantum mechanics, the possible energy levels shift to higher energy as the particle size decreases. This energy transfer can be identified by a change in light emission at the quantum dots (Figure 1.2). [5]

After extensive research on quantum dots, carbon nanomaterials such as fullerene and carbon nanotubes have been studied by many scientists (Curl, Kroto, Smalley, Iijima, etc.).[6] Carbon nanomaterials research has sought scientists to gain insights into metal and semiconductor nanowires, nano-belts, heterogeneous structures, and highly complex nanomaterial structures. The technical expansion of the electron microscope enabled observation of new structures providing new information to understand nanostructures.

As research using nanomaterials increases, scientists have found that the properties of nanomaterials cannot be predicted as relative bulk materials. For example, metal oxide nanotubes, known as with brittle mechanical behavior, have been found to be very flexible. Carbon nanotubes (CNTs) showed better strength and toughness than the strongest diamond. It has also been found that

the degree of chirality in CNTs can affect the electron transport properties between metal and semiconductor materials.

As scientists continue to report on new properties of nanomaterials, they have found that the realization of nanomaterials can provide an opportunity to access fundamental scientific issues. With the development of new materials based on experimental approaches in terms of propelling their research in nanoscience and nanotechnology, theorists based on computational approaches are attempting to understand the origin of new properties. Computer simulation has been performed to demonstrate the physics behind nanomaterials with unique mechanical, chemical, electronic, optical, and other properties. In the early 1970s, the rapid growth of the computing process began, so you can validate the results of the experiment before the start of the task.

Recently, the computer industry has been working hard to make more sophisticated devices in smaller spaces while increasing computing performance and speed while maintaining reasonable prices. Even though, manufacturer has pushed to keep their continuous developing devices along the Moore's Law (Figure. 1.3), a prediction that the number of transistors on an integrated circuit could grow by a factor of 2 approximately every 18 months industry leaders have recognized that the growth trend of integration will be slow owing to their physical limits of miniaturization. The best microchips were recently reported with containing millions of transistors in only 100 atoms

across.[7] It is clear that Moore's Law paradigm cannot continue to work with traditional silicon processing technology. Nanotechnology has benefited from both theoretical and experimental research, and manufacturers have realized that innovative technologies are needed to prevent inevitable deceleration. From this perspective, many companies are investing in nanotechnology resources to overcome the obstacles inherent in traditional device manufacturing.

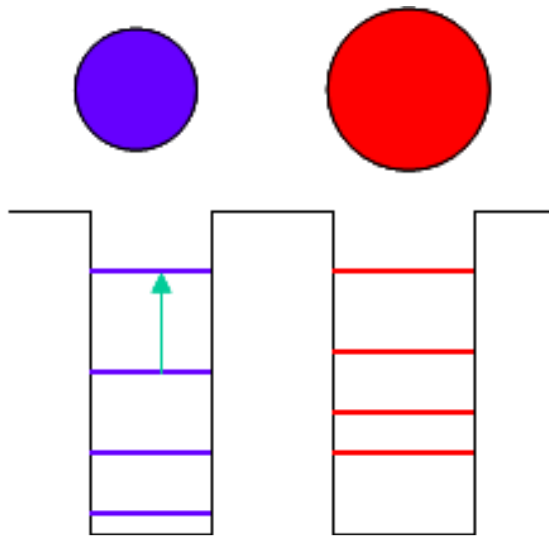


Figure 1.2 Schematic illustrating color change in a quantum dot resulting from a shift in possible energy states corresponding to size change.

Moore's Law

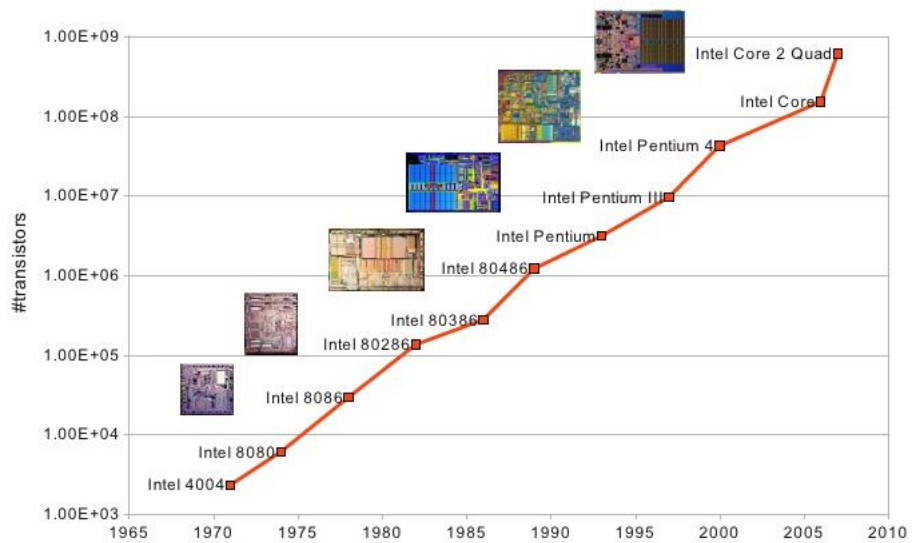


Figure 1.3 Graph illustrating the exponential growth of IC transistors according to Moore's Law from 1971 to 2000.

1.2 Nanomaterials

The special function of the substance at the nanoscale has been known for some time. In nature, the influence of design on nanoscale is well known, and nature has evolved a very interesting use for nanomaterials. For example, some bacteria have internal magnetic nanoparticles that are used as compasses to provide a sense of direction to the bacteria.[8] Even larger creatures used nano-sized designs. The nano-sized Gecko foot hair has an excellent ability to climb smoothly up the vertical plane. Individual hairs (seta) are acted upon by van der Waals forces, allowing for greater adhesion.[9] Even the most basic building blocks of biological things are an example of nanoscale design.[10] These are shown in Figure 1.4.

In addition to being used in nature, nanomaterials have been unconsciously used by artisans for centuries. If the size of the gold is significantly reduced, you will not see any unfamiliar yellow-metallic appearance, but you can get an array of colors.[11] Chinese craftsmen discovered this when they crushed gold to make red paint that appeared in many vases. European medieval craftsmen have found that gold chloride can be mixed with molten glass to enrich the ruby color.[12] By changing the amount of gold in the mixture, another color could be created. The size of gold nanoparticles and silver nanoparticles are shown in Figure 1.5. The cause was not known at the time, but the small gold spheres were tuned to absorb and reflect sunlight in a slightly different way and could

be adjusted to the size of these particles.

Electron microscopy allows for proper classification of nanomaterials and can be discussed in an easy to understand and useful way. Because the main features of nanomaterials are small in size, nanomaterials are classified by the number of dimensions that are limited to nanoscale. Indicates the number of space dimensions whose names have been reduced due to the Convention and are not actually limited to nano-size. This is a marvel of scientific naming. Thus, two-dimensional nanomaterials are so named because they are only one-dimensionally confined to the nanoscale. One-dimensional nanomaterials are named because they are limited to nanoscale in two dimensions. Finally, zero-dimensional nanomaterials are named because they are all nanoscale-limited in three dimensions.

The focus of this paper is on one-dimensional nanostructures. But for some reason it is important to understand the relationship with other nanostructures. First, many phenomena occurring in one-dimensional nanostructures occur in zero- and two-dimensional nanostructures. Understanding these phenomena in this structure can be understood even in one-dimensional nanostructures. Second, many architectures and devices use a combination of different types of nanostructures. Understanding the similarities and associations between the three types of nanomaterials will enable a greater understanding of larger devices.

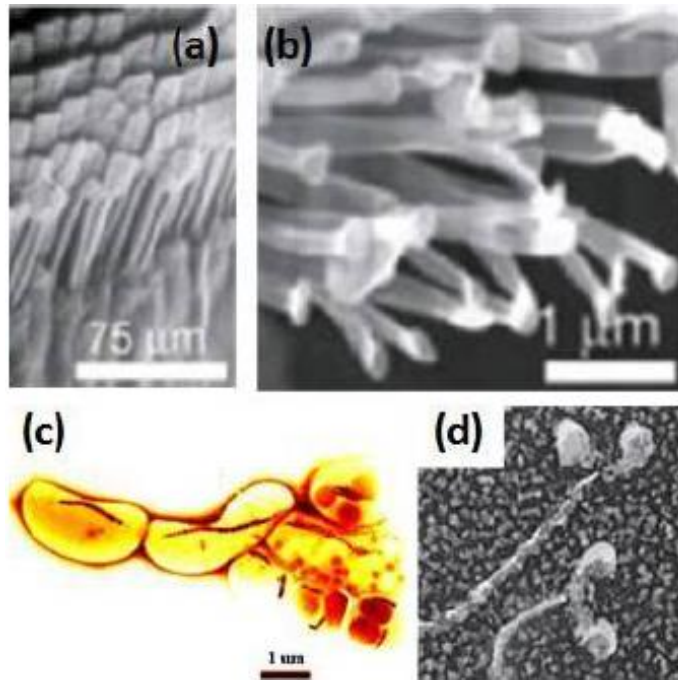


Figure 1.4 (a), (b) SEM image of gecko head showing nano-sized theta small enough to operate using van der Waals force as an adhesive; (c) a color image of bacteria with magnetic nanowire particles inside used as a compass to aid the direction of the bacteria; (d) SEM image of a molecular motor used to move in nanometer increments along a protein track within the cytoplasm of the cell.

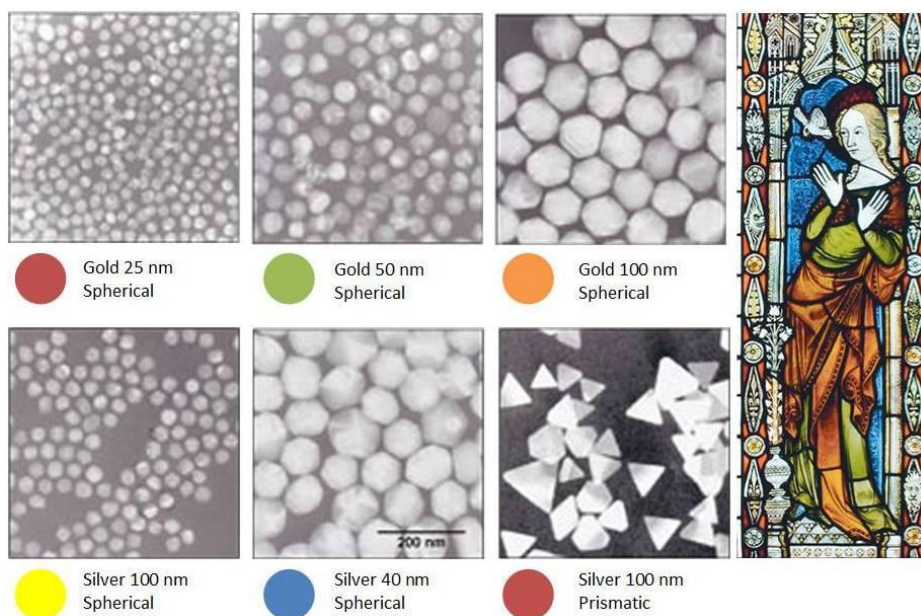


Figure 1.5 Nanomaterials have been used unknowingly in stained glass by grinding up gold and silver nanoparticles to small sizes. This figure shows SEM images of gold and silver nanoparticles with sizes ranging from 25 nm to 100 nm. Both gold and silver change their color significantly with size. Silver also can change its color depending on its shape as seen in the difference between the spherical and prismatic 100 nm silver nanoparticles.

1.2.1 Zero-dimensional Nanostructure-Quantum Dots and Nanoparticles

One of the earliest nanomaterials studied extensively was the quantum dot (QD). Quantum dots are semiconductor, zero-dimensional nanostructures. Quantum dots were first theorized in the 1970s and synthesized in the early 1980s. If the semiconductor particles are small enough, the quantum effect starts to appear on its own. This effect limits the energy that electrons and holes can have in the particle. Since energy is related to the wavelength of the generated photons, it means that the optical properties of the particles can be finely tuned according to their size.

The quantum confinement effect begins to occur as the size of the material decreases. Quantum confinement is when the material is less than or equal to the exciton Bohr radius of the constituent compound.[13] The quantum damping effect has a significant effect on the optical properties of the material. A popular quantum dot material is cadmium selenide (CdSe). Figure 1.4 shows the size-dependent characteristics of the CdSe QD. In the image, each vial is filled with a monodisperse CdSe QD solution in which the particle size is reduced from left to right. The result is dramatic.

Bell Labs scientists were among the first to determine the direct relationship between the quantum constraint of zero-dimensional cadmium selenide

quantum dots and the higher energy transfer induced in the electron band structure.[14,15] When CdSe is reduced to nanoscale dimensions in 1, 2 and 3 dimensions, it has been demonstrated that the energy band is reconstituted into a band structure similar to the individual atoms.[16] That is, on a sufficiently small scale, with a sufficient number of small numbers, a group of atoms behaves like an atom. For this reason, quantum dots are often referred to as artificial atoms.

Due to its unique properties, quantum dot has promising potential applications. There is a growing body of research using quantum dots in biotechnology imaging and computing applications.[17-19] Biological markers should utilize the luminescence properties of QDs and attach functional groups to the surface of QDs. Functional groups preferentially bind to specific organisms, cells or proteins once the system is injected into a biological system. The QD then emits light through luminescence or fluorescence to detect and track biological targets inside the body.[20,21] Unlike current organic dyes, using QDs in this application has the advantage that QD is brighter and more resistant to light.[22]



Figure 1.6 This vial contains a solution with monodisperse CdSe quantum dots of different sizes. On the left side, there are small quantum dots ranging from blue to red.

1.2.2 Two-Dimensional Nanostructure – Thin Films

Two-dimensional nanostructures have been traditionally studied and classified because they are limited to nanoscale in one dimension and are classified as "thin films." It has been developed for considerable time usage in various fields such as electronic devices and photovoltaic applications. For example, in the silicon integrated circuit industry, many devices rely on thin films for their operation and require control of film thicknesses close to atomic levels. Faults are often used in chemistry. The formation and properties of these layers are well understood from the atomic level even in the more complex layers used in lubricants. Significant research is underway to precisely control the composition and softness of these films.

Thin film nanostructures are suitable for the efficient conversion of light from photovoltaic devices in photovoltaic processes with large surface areas. We have studied the synthesis of TiO_2 electrode by improving the PV structure for efficient electron transfer and excellent stability through a large amount of research. In addition, compression of TiO_2 powder has been used as a technique for forming a thin film.[23-28] However, TiO_2 films have difficulty achieving efficiencies of more

than 10%. So we focused on broad band gap semiconductor oxide materials such as ZnO and SnO₂. In addition, research has been conducted to improve the overall efficiency through a combination structure composed of a semiconductor oxide film and a polymer layer for a semiconductor solar cell device. Up to now, efficiency improvements of up to 5% for these ZnO devices, 1% for SnO₂ devices and up to 2% for hybrid devices have been demonstrated.[29]

1.3 II-VI semiconductors

In general, eight II-VI semiconductor materials are known. They are ZnO, ZnS, ZnSe, ZnTe, CdO, CdS, CdSe, and CdTe. The II-VI semiconductors have been the focus of intensive research on recent nanomaterials due to their use in optoelectronics and semiconductor applications. The II-VI semiconductors are typically wide band gap materials and act as efficient light emitters. This is a likely candidate to replace materials such as GaN in LEDs (light emitting diodes). [30] Each of the II-VI semiconductors has unique properties and is useful for unique applications. ZnS has a band gap of 3.54 eV with respect to the zinc-blended phase, and has a band gap of 3.91 eV with respect to the wurtzite phase. [31] It has a high refractive index of 2.2 and high light transmittance in the visible region of the spectrum. [32-34] Because of these properties, ZnS is a strong candidate for optoelectronic devices. The nanostructures of II-VI semiconductors also have some unique properties. ZnO nanowires can be operated with Ohmic or Schottky devices, and these nanowires can be used as nano-generators and piezoelectric sensors.

This thesis will focus on two specific II-VI semiconductors that provide the greatest potential in nanostructure applications. A brief section of the paper will be given first to ZnO nanostructures, including a brief consideration of the electrical properties of ZnO microwire. Much of the paper consists of a discussion of ZnS nanostructures focused on the in-situ heating and 3D printing

of ZnS nanowire.

1.3.1 Zinc Oxide - ZnO

ZnO is one of the most important nanomaterials studied extensively. The crystal structure of ZnO at nanoscale is wurtzite structure with lattice parameters $a = 0.3296\text{nm}$ and $c = 0.52065\text{nm}$. It consists of several alternating planes stacked along the c-axis alternating tetrahedral-coordinated O^{2-} and Zn^{2+} ions. The Zn-(0001) polar surface charged to the anode along the c-axis and the O-(0001) polar surface charged to the cathode are the strongest polar surfaces. The pole surface contributes to various ZnO nanostructures by surface reconstruction to maintain a stable structure. When stress is applied, the non-central symmetric structure leads to the separation of the center point of positive charge and the center point of negative charge, resulting in polarization. This is called piezoelectricity, an important property of ZnO. In addition, ZnO is an important semiconductor with a large direct bandgap of 3.37 eV. Due to the difference in work function Φ between the contact metal and ZnO, ZnO nanowire-based devices can operate as Ohmic or Schottky devices. Nanowire-based nano-generator and force sensors found in 2006 can be explained by the combined effect of piezoelectric properties and semiconductor properties. [35,36] Because of all of these key properties, ZnO has great potential for applications in nanoscience and nanotechnology.

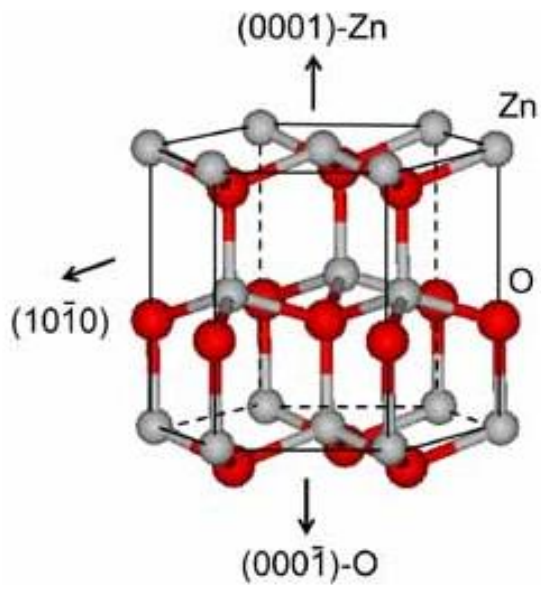


Figure 1.7 ZnO wurtzite crystal structure.

1.3.2 Zinc Sulfide - ZnS

Wurtzite ZnS is a direct broadband (3.91 eV) semiconductor, one of the most important materials in photonics. This is due to the high transmittance and high refractive index (about 2.2) in the visible range. ZnS has been synthesized as nanowires, nanobelts, nanocombs and recently nanohelices.[37-40] All of these are one-dimensional nanostructures. Recently, the ZnS nanotubes have been doped with manganese without changing the crystal structure.[41] ZnS doped with manganese exhibits attractive luminescent properties with increased optically active sites for efficient phosphor applications. In addition, a single ZnS nanobelt has been shown to facilitate optical pumping lasers.[42] All of these properties make ZnS 1-D nanostructures attractive candidates for use in devices and other technologies.

ZnS is also an important phosphorescent lattice material used in electroluminescent devices (ELD) due to the efficient transfer of high energy electrons and bandgaps that are large enough to emit visible light without absorption. Electroluminescent display devices consist of several layers. The center layer is a phosphor that emits light when an electric field of about 1.5 MV / cm is applied. Because of this high field level, a current limiting insulating layer is placed on both sides of the phosphor. Finally, the electrodes at the top and bottom of the device form the basic capacitive structure. Of course, in order to view the emitted light, at least one electrode is transparent.[43]

1.4 Thesis motivation

To reach the realization of a nanodevice based on a bottom-up paradigm, nanoscale chemical composition, structure and size control methods are needed through rational synthesis including reproducibility. Since there are very different properties such as quantum confinement in nano-building blocks, we have to study the limitations of nano-devices based on nano-building blocks. Just as a complement to nanodevices, the right approach for building blocks must be developed for sustainable nano-device operation.

In an effort to address some of these obstacles, the work described in this thesis focuses on understanding the growth behavior and the underlying synthesis of II-VI nanowires. The goal is to investigate the nanostructures associated with specific growth conditions and then closely analyze these structures to gain new insights into growth behaviors that manage nucleation and growth.

In particular, the study focused on nanowires and emphasized their underlying growth behavior and applicability. Among the II-VI compound semiconductor materials, ZnS and ZnO were selected because of their photoelectric characteristics and applicability of nano-optoelectronic devices. The growth behavior of ZnS nanowires was investigated through in-situ heating experiments, and new analytical methods of ZnS nanostructure grown by

combining TEM tomography and 3D printing technology were described. In addition to studying the optoelectronic properties of ZnS nanowires, diamond-like carbon was selected as the shell material of ZnS nanowires that serves to increase the infrared transmittance in the bulk state.

This is done using a wide range of experimental approaches that provide possible growth mechanisms and applications. In this work, this information can provide an important step in assembling highly integrated electronics, photons, and photovoltaic devices.

1.5 References

- [1] “Wikipedia.”
- [2] The 21st Century Nanotechnology R&D Act, USA Congress S.189
- [3] A. D. Yoffe, *Advances in Physics*, **42**, 173, (1993)
- [4] L. E. Brus, *Journal of Chemical Physics*, **80**, 4403, (1984)
- [5] A. P. Alivisatos, *Science*, **271**, 933, (1996)
- [6] S. Iijima, *Nature*, **354**, 56, (1991)
- [7] D. K. Ferry, *Science*, **319**, 579, (2008)
- [8] T. Matsunaga, *Journal of Materials Chemistry*, **14**, 2099, (2004)
- [9] K. Autumn, *Nature*, **405**, 681, (2000)
- [10] M. Schliwa, *Nature*, **422**, 759, (2003)
- [11] C.D. Geddes, *Chemical Physics Letters*, **380**, 269, (2003)
- [12] K. Chang, *Tiny is Beautiful: Translating 'Nano' Into Practical*, in *The New York Times*. 2005: New York City, NY.
- [13] M.G. Bawendi, *The Journal of Chemical Physics*, **96**, 946, (1992)

- [14] A.P. Alivisatos, *The Journal of Chemical Physics*, **89**, 4001, (1988)
- [15] L.E. Brus, *The Journal of Chemical Physics*, **80**, 4403, (1984)
- [16] C.B. Murray, *Journal of the American Chemical Society*, **115**, 8706, (1993)
- [17] W.C. Chan, *Science*, **281**, 2016, (1998)
- [18] M. Bruchez, *Science*, **281**, 2013, (1988)
- [19] X. Li, *Science*, **301**, 809, (2003)
- [20] P.T. Tran, *Physica Status Solidi B*, **229**, 427, (2002)
- [21] X. Gao, *Nature Biotechnology*, **22**, 969, (2004)
- [22] A.M. Smith, *Photochemistry and Photobiology*, **80**, 377, (2004)
- [23] K. Keis, *Journal of Photochemistry and Photobiology a-Chemistry*, **148**, 57, (2002)
- [24] S. Karuppuchamy, *Solid State Ionics*, **151**, 19, (2002)
- [25] K. Tennakone, *Physica E*, **14**, 190, (2002)
- [26] S. Chappel, *Langmuir*, **18**, 3336, (2002)

- [27] S. Chappel, Solar Energy Materials and Solar Cells, **71**, 141, (2002)
- [28] S.G. Chen, Chemistry of Materials, **13**, 4629, (2001)
- [29] W.U. Huynh, Advanced Materials, **11**, 923, (1999)
- [30] J. Gutowski, Physica Status Solidi B-Basic Research, **234**, 70, (2002)
- [31] B. Ray, II-VI Compounds. 1 ed. International series of monographs in the science of the solid state, ed. B.R. Pamplin. Vol. 2. 1969, Oxford, London, U.K.: Pergamon Press. 268.
- [32] X. Jiang, Chemistry of Materials, **13**, 1213, (2001)
- [33] S. Yamaga, Journal of Crystal Growth, **86**, 252, (1988)
- [34] B. Elidrissi, Materials Chemistry and Physics, **68**, 175, (2001)
- [35] Z. L. Wang, Science **312**, 242 (2006)
- [36] X. D. Wang, Science **316**, 102 (2007).
- [37] C. Ma, Advanced Materials, **15**, 228, (2003)
- [38] D. Moore, Chemical Physics Letters, **385**, 8, (2004)
- [39] D. Moore, Journal of the American Chemical Society, **126**, 14373, (2004)

[40] D. Moore, Polar ZnS Nanohelices. 2006, Georgia Institute of Technology.

[41] Y.Q. Li, Applied Physics Letters, **88**, 13115, (2006)

[42] J.A. Zapien, Applied Physics Letters, **84**, 1189, (2004)

[43] C.N. King, Journal of Vacuum Science & Technology A - Vacuum Surfaces and Films, **14**, 1729, (1996)

Chapter 2.

One-Dimensional Nanostructures

2.1 General Properties of Nanomaterials

Unlike bulk materials, the ratio of surface atoms per unit volume is relatively important at nanoscale, which contributes to new chemical and physical phenomena in terms of surface energy excellence. For example, the ratio of the volume of Fe (iron) to the surface atoms of 1 cm^3 is about 10-5% while the surface atoms of Fe with a volume of $10 \times 10 \times 10 \text{ nm}^3$ show an improved ratio of 10%. Also, when the volume of iron is 1 nm^3 , all atoms of Fe can be placed on the surface. [1]

The total surface energy of a material is directly proportional to the surface energy of all atoms made up of one material. Table 2.1 shows trends between total surface area and surface energy. From this tendency, the surface energy at the bulk size is negligible. In other words, total surface area and energy increase very much at the nano level. Increased surface energy at the nanoscale becomes thermodynamically unstable. It is therefore important to understand the basic behavior that corresponds to surface energy changes at the nanoscale.

In general, physical properties such as electrical conduction and dielectric constant can be measured by electrical conductance, capacitance and tensile

stress. For nano-sized physical properties, it is typically reduced by 17% compared to the bulk state.

In addition to general properties, new features may appear on the nanoscale. Doping for semiconductor processing is a well-established technique in the bulk state, but it can affect characteristics very different from nanoscale semiconductor manufacturing. For example, a $10 \times 10 \times 10 \text{ nm}^3$ volume semiconductor containing a doping element of $10^{18} / \text{cm}^3$ means that one doping atom in a unit volume can play an important role in influencing electrical properties.

Length of edge (cm)	Total surface area (cm³)	Surface energy (J/g)
0.77	3.6	7.2×10^{-5}
0.1	28	5.6×10^{-5}
0.01	280	5.6×10^{-3}
0.001	2.8×10^3	5.6×10^{-2}
10^{-4}	2.8×10^4	0.56
10^{-7}	2.8×10^7	560

Table 2.1 Size-dependent surface energy variation of NaCl (1g).

2.2 Definition and Types of 1-D Nanostructures

Nanomaterials are usually dimensionally classified as one-dimensional (nanowires, nanotubes, and nanobelts) or two-dimensional (thin-film) zero-dimensional (dots or mostly spherical nanoparticles). This category refers to the number of dimensions in which the material is outside the nano regime. For example, a thin film consists of large expansions of material in both in-plane directions and is nano-sized in thickness. It is therefore called a two-dimensional (2D) nanomaterial.

Because of the size effects discussed in the previous chapters, the dimensional properties of nanomaterials can change their properties, and thin films can behave very differently from nanowires with the same chemical properties. Therefore, this distinction is not arbitrary, but it is important to distinguish these substances according to their unique characteristics. Figure 2.1 below shows the differences between these types of nanomaterials.

Since 1D nanomaterials are relatively easy to synthesize, much effort has been focused on the development and application of 2D and 0D nanomaterials. The development of molecular beam epitaxy (MBE) technology, in which the material can be formed into a single atomic layer, allowed extensive research on 2D nanomaterials. Chemical monolayer formation has also been adopted as a reliable means of forming high quality 2D nanomaterials. Thin film formation

and properties are now well-known and form the cornerstone of many high-precision products, including commercial lasers, silicon microelectronics and NASA-quality optical components. 0D quantum dots are easily synthesized through wet chemistry, aerosol spraying, and other methods (even though uniform size distribution is a problem) and have been developed in numerous commercial applications over the past few decades.

There are a quantum dot laser, a biological fluorescence probe, and a single electron transistor.[2-4] Many researchers have not sought to study 1D nanomaterials because of their lack of control over complex and mysterious formation processes and synthesis, operational difficulties, and lack of standard and verifiable characterization.

However, as our understanding of these materials has increased and synthetic technologies have greatly improved, there has been an explosion of publications focused on 1D nanomaterials over the last 10-20 years. Starting with carbon nanotubes, 1D nanomaterials have grown to include nanowires and nano-belts, nanoscale heterostructures with semiconductor materials, complex geometries, and various components. Recently, they have been used potentially in the fields of structural, commercial, environmental, electronic and biological applications, which have brought about the interest and imagination of researchers and the general public in almost all scientific disciplines. Still, our understanding of 1D nanomaterials is incomplete, our control is limited, and

production is still expensive compared to other nanomaterials. Certainly improved synthesis techniques have helped to develop 1D nanomaterials research and the driving force behind the rapid development is the need to use the unique properties of nanomaterials.

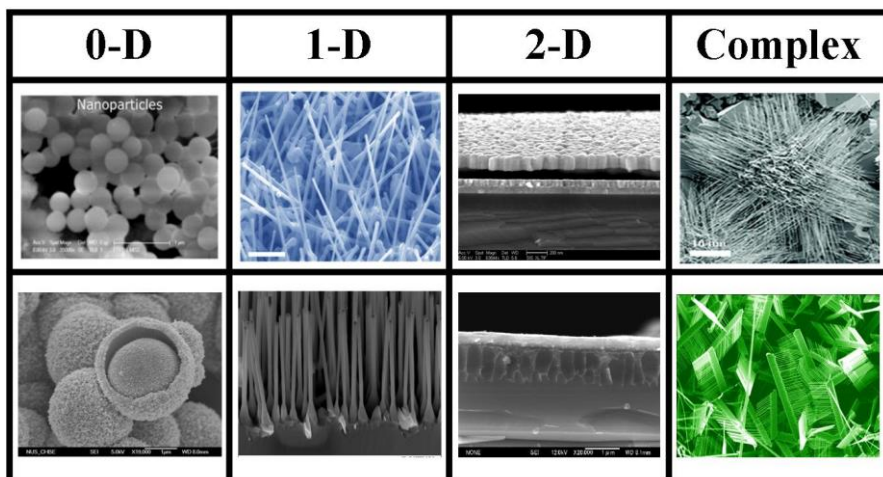


Figure 2.1 SEM images of nanomaterial classifications.

2.3 Top-Down and Bottom-Up Approach

There are two common methods for producing nanomaterials. The first method is to start with the bulk material from top-down and then break it up into small pieces using mechanical, chemical or other forms of energy. The second method, bottom-up, is to increase the size of precursor particles by synthesizing a material from an atom or molecular species through a chemical reaction. Both methods can be performed in gas, liquid, supercritical fluid, solid state or vacuum state. Most manufacturers are interested in a) particle size b) particle shape c) size distribution d) particle composition e) ability to control grain cohesion.

Recently, a key issue in nanotechnology is the development of conceptually simple construction techniques for the mass fabrication of identical nanoscale structures. Conventional top-down fabrication techniques are both top down fabrication techniques are intensive and wasteful in a view of energy, because many production steps involve depositing unstructured layers and then patterning them by removing most of the deposited films. Furthermore, increasingly expensive fabrication facilities are required as the feature size decreases. The natural alternative to the top-down construction is the bottom-up approach, in which nanoscale structures are obtained from their atomic and molecular constituents by self-organized growth. Self-organized growth can be driven by thermodynamic forces or be the result of

kinetic processes. The archetype of a thermodynamically driven structure formation at the mesoscopic scale is molecular self-assembly. This refers to the spontaneous association of molecules under conditions close to equilibrium into stable, well-defined nanostructures joined by non-covalent bonds; it is one of the key building principles of all living matter (Figure 2.2).[6] To make full use of this approach in nanotechnology, we have to understand the non-covalent intermolecular interactions and to develop methods to manipulate them in a controlled way.[7]

To reach realization of integrated nano-devices based on bottom-up paradigm, the following issues must be investigated over nanowire building-block;

- The control manner for accurate chemical composition, size, opto/electrical properties
- The advanced technique on building block for devices with more complex structure
- New integrated circuit design via self or directed assembly and verification of functions on novel nano-devices

At a period of initiation on 1D nanomaterials research, single wall carbon nanotube (SWCNT) has drawn much attention due to their predictable applications such as field emission transistor (FET), diode, and logic gate.

In spite of fascinating properties of SWCNT, there have been some obstacles for nano-devices using SWCNT due to a lack of control manner

based on metallic and semiconducting properties. In contrast to SWCNT, synthesis of semiconducting nanowires is relatively easy since single crystalline nanowires can be achieved with reproducibility including chemical composition, diameter, length, and doping/electrical property. In this regard, building block using nanowires have been focused for substantial applications such as p-n diode, c-NW-FET, logic gate, LED, and laser.[8-11]

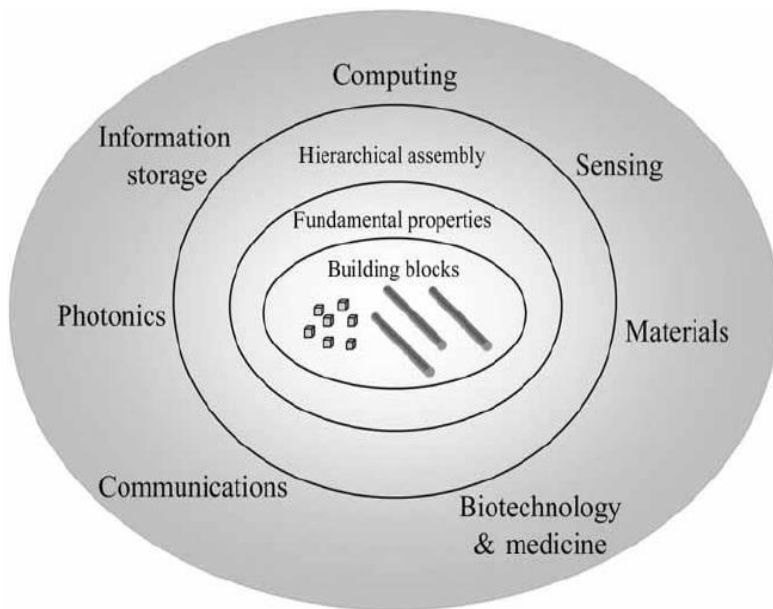


Figure 2.2 Overview of the bottom-up paradigm for nanotechnology.

2.4 Nanowire Synthesis and Theory

The controlled synthesis of nanostructures has attracted much attention, such as chemical and physical phenomena, which depend on many exhibit sizes and dimensions that can be adjusted as desired for a particular application.[12] 1D nanostructures, such as nanowires, are important for basic material research and can function as active devices and interconnects, making them suitable for many applications.[13] Several methods can be used to fabricate nanostructures, but they can be classified as vapor deposition or solution-based chemistry, as shown in the table below.

This section discusses general theories and related synthesis of nanowires, including vapor synthesis and solution-based chemistry. This thesis focuses on the vapor growth process.

Physical Vapor Deposition (PVD)	Thermal Evaporation <i>Electron-beam</i> <i>RF Induction</i> <i>Resistive</i> Sputtering <i>Focused Ion Beam</i> <i>Radio frequency</i> <i>Magnetron</i> Pulsed Laser Deposition
Chemical Vapor Deposition (CVD)	Thermal CVD Low-pressure CVD (LPCVD) Plasma-enhanced CVD (PECVD) Metal-organic CVD (MOCVD) Molecular Beam Epitaxy (MBE) Atomic Layer Deposition (ALD)
Solution Based Chemistry (SBC)	Hydrothermal Sol-gel

Table 2.2 Classifying nanostructure fabrication techniques

2.4.1 Vapor Synthesis

2.4.1.1 Vapor-liquid-solid growth

The growth of nanowires through a gas phase reaction including the vapor-liquid-solid (VLS) process has been the most widely studied. Wagner proposed in 1960s, a mechanism for the growth via gas phase reaction involving the so-called vapor-liquid-solid process.[14] He worked for the growth of mm-sized Si whiskers in the presence of Au particles. The mechanism described in this report is suggested that the anisotropic crystal growth is activated by the presence of the liquid alloy/solid interface, and this mechanism has been widely accepted and applied for understanding of various nanowires. The growth of Ge nanowires with Au clusters is understood based on the Ge-Au phase diagram in figure 3.1. Ge and Au form a liquid alloy when the temperature is higher than the eutectic point as shown in figure 2.3 (a- I).[15] The liquid surface has a large accommodation coefficient and is therefore a preferred site for the incoming Ge vapor. After the liquid alloy involving Ge and Au becomes supersaturated state, precipitation of the Ge nanowire starts at the solid-liquid interface (Fig.2.3.a-II,III).

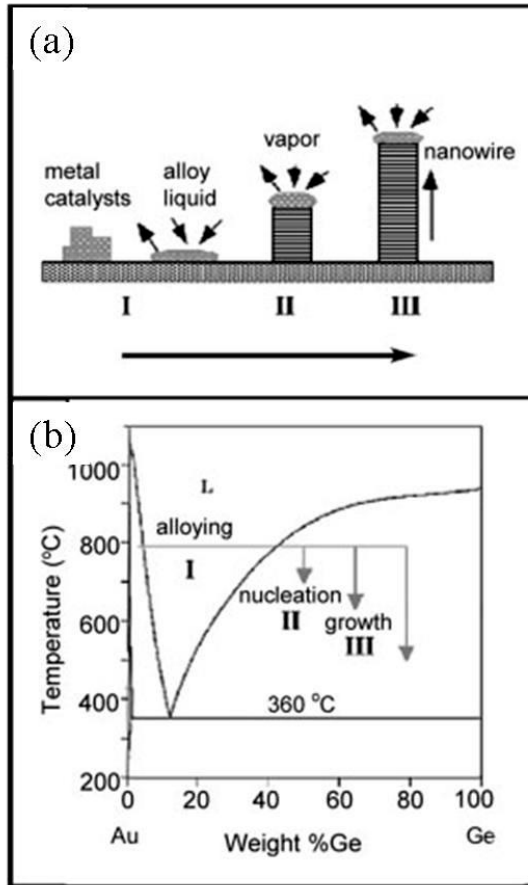


Figure 2.3 (a) Schematic illustration of vapor-liquid-solid growth mechanism including three stages. (I) alloying, (II) nucleation, (III) axial growth. Three stages are projected onto the conventional Au-Ge phase diagram; (b) shows the compositional and phase evolution during the nanowire growth process.

The only clue that nanowires grew by VLS mechanism is considered by the existence of alloy droplets at the top of the nanowire. Wu et al. have reported real-time observation of Ge nanowire grown by in-situ heating TEM, which demonstrate the validity of the VLS growth mechanism. Wu's report shows that there are three growth steps: metal alloying, crystal nucleation, and axial growth (Figure. 2.4).[16]

Figure. 2.4 displays a sequential images of Ge nanowire growth grown by in-situ heating TEM. Three steps (I -III) are clearly demonstrated.

(I) Alloying process (Fig.3.2(a)-(c)): The maximum temperature that could be gained in the system was 900°C, which the Au clusters remain in the solid state in the absence of Ge vapor. As increasing amount of Ge vapor condensation and dissolution, Ge and Au form a liquid alloy. The volume of the alloy droplet increases, while the alloy composition moves, from left to right, to a biphasic regime (solid Au and Au/Ge liquid alloy) and a single-phase region (liquid). An isothermal line in the Au-Ge phase diagram in figure 2.4(b) shows the alloying process.

(II) Nucleation (Fig. 2.4(d)-(e)): the nucleation of the Ge nanowire begins when the concentration of Ge in Au/Ge alloy droplet becomes supersaturated. From the volume change of the Au/Ge liquid alloy, it is estimated that the nucleation generally occurs at a Ge weight percentage with 50-60%.

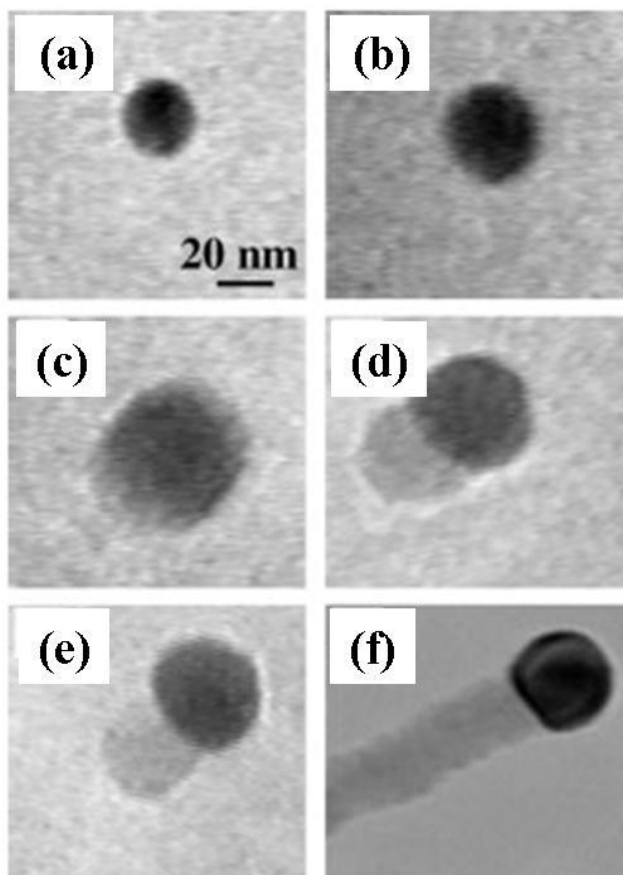


Figure 2.4 In-situ TEM images recorded during the process of nanowire growth. (a) Au nanoclusters in solid state at 500°C; (b) alloying initiated at 800°C, at this stage Au exists mostly in solid state; (c) liquid Au/Ge alloy; (d) the nucleation of Ge nanocrystal on the alloy surface; (e) Ge nanocrystal elongates with further Ge condensation and eventually forms a wire (f).

(III) Axial growth (Figure 3.2(d)-(f)): Once precipitation of Ge nanowire begins at the liquid/solid interface, further Ge vapor into the Au/Ge droplet alloy increases the amount of Ge precipitation from the alloy. The incoming Ge vapors diffuse and condense at the solid/liquid interface, which lead to secondary nucleation events. This report confirms the validity of the VLS growth mechanism at nanoscale.

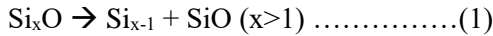
After the diameter of catalyst governs the diameter of nanowires, VLS manner is not only to provide an efficient ways to obtain uniform nanowires, but also to gain insight to extend the knowledge of the phase diagram of the reacting species. Physical methods, such as laser ablation, thermal evaporation, as well as chemical vapor deposition can be used to generate the reactant species in vapor form, required for the nanowire growth. From this perspective, various nanowires, such as elements, oxides, carbides, etc., have been successfully synthesized with VLS manner.[17-19]

2.4.1.2 Vapor-solid growth

The nanowires can also be synthesized without catalysts by thermally evaporating a proper source materials near their melting point and depositing at cooler temperatures.[20] This method, the synthesis without liquid droplets corresponding to alloying, is referred to as a vapor-solid (VS) method. The VS method has been adopted to prepare whiskers of oxide, as well as metals with micrometer diameters. Even though no tight manner to control the spatial arrangement has been reported so far, it is worth mentioning that various nanowires can be obtained via VS manner if one can control the nucleation and the subsequent growth process.[21]

2.4.1.3 Oxide-assisted growth

In contrast to the well-established VLS growth, Lee and co-researchers have suggested a nanowire grown by the oxide-assisted mechanism.[22] At this report, these researchers find that the growth of Si nanowire is highly enhanced when Si powder target containing SiO₂ were utilized. Lee et al. proposed that the growth of the Si nanowire was assisted by the Si oxide, where the Si_xO (x>1) vapor generated by thermal treatment plays the key role. Nucleation of the nanoparticles was assumed to occur on the substrate as shown in equation (1) and (2).



The precipitation of Si nanoparticles is attributed in these decompositions, which serve as the nuclei of the silicon nanowires sheathed by shells of silicon oxide. The precipitation suggesting that temperature gradient gives the external driving force for the formation and growth of the nanowires.

Figure 2.5 (a)-(c) reveal the TEM images of the formation of nanowire nuclei at the initial stages. Figure 2.5 (a) displays isolated Si nanoparticles covered by an amorphous silicon oxide layer, which have the growth normal direction to the substrate. The tip of the Si crystalline core possesses a high concentration of defects, as indicated by arrows in figure 2.5 (c). Figure 2.6 shows a schematic

diagram of the oxide-assisted mechanism. The Si nanowires growth is governed by four factors: (1) catalytic effect of the Si_xO ($x>1$) layer on the nanowire tips (2) retardation of the lateral growth of nanowires by the SiO_2 component in the shells (3) stacking faults of growth direction of $\langle 112 \rangle$, which contain $1/6[112]$ and non-moving $1/3[111]$ partial dislocations, and micro-twins reveals at the tip areas coming fast growth of Si nanowires (4) the $\{111\}$ plane with the lowest surface energy plays an important role during nucleation and growth, since the energy of the system is decelerated significantly when the $\{111\}$ surfaces are parallel to the axis of the nanowires. The aforementioned last two factors are only working at lying in $\langle 112 \rangle$ direction parallel to the growth direction.

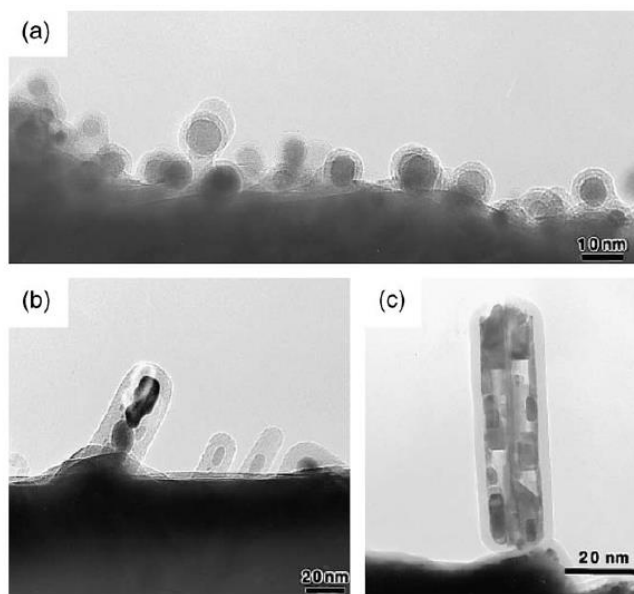


Figure 2.5 TEM images of (a) Si nanowire nuclei formed on the Mo grid and (b), (c) initial growth stages of the nanowires.

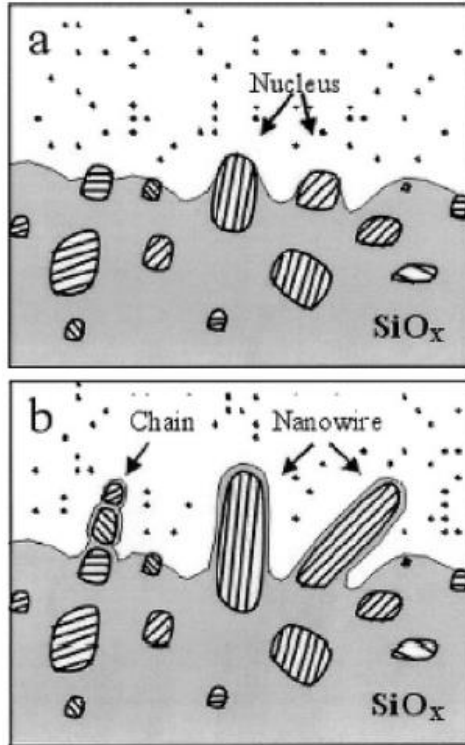
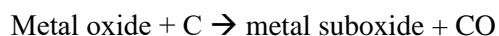


Figure 2.6 Schematic diagram of the nucleation and growth mechanism of Si nanowires. The parallel lines indicate the [112] orientation. (a) Si oxide vapor is deposited first and forms the matrix within which the Si nanoparticles are precipitated. (b) Nanoparticles in a preferred orientation grow fast and form nanowires. Nanoparticles with non-preferred orientations may form chains of nanoparticles.

2.4.1.4 Carbothermal reactions

Carbothermal reactions are useful for the growth of oxides, nitrides, and carbides nanowires. For example, carbon mixed oxide makes sub-oxidic vapor species since it reacts with C, O₂, N₂ or NH₃ to produce the intended nanowires. The typical example is that the heating of the mixture with Ga₂O₃ and carbon in N₂ atmosphere forms GaN nanowires.[23] Carbothermal reactions generally are as follows:



In general, the first step includes the formation of a metal suboxide by the reaction of the metal oxide with carbon. With regarding to the desired product, the suboxide heated in the existence of O₂, NH₃, N₂ yields oxide, nitride or carbide nanowires.

2.4.2 Solution Based Growth of Nanowires

2.4.2.1 Template-based synthesis

The growth of template-directed nanowires is the most widely studied strategy in solution based synthesis. In this manner, the template provides as a scaffold against which other materials with similar morphologies are synthesized. The in-situ generated material is formed into a nanostructure with morphology complementary to that of the template. The templates can be nanoscale channels within mesoporous materials such as porous alumina and polycarbonate membranes. For the formation of nanowires, the nanoscale channels are filled in terms of the solution, the sol-gel or the electrochemical manner. The desired nanowires can be synthesized after removal of the host matrix.[24] Unlike the polymer membranes made by etching, anodic alumina membrane (AAM) involving a hexagonally packed 2D array of cylindrical pores with a uniform size are fabricated using anodization of aluminum foils in an acidic medium (Fig. 2.7).

The various materials such as elements, oxides, chalcogenides are synthesized by electronically conducting polymers such as polypyrrole, poly(3-methylthiophene) and polyaniline. The only drawback of template-based growth is difficulty of achieving materials with single-crystalline.

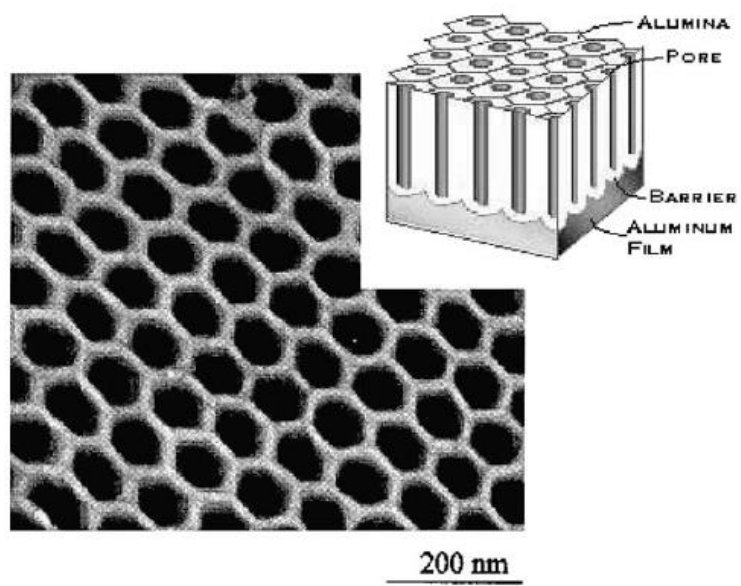


Figure 2.7 TEM image of an anodic alumina membrane (AAM).

Additionally, alumina and polymer membranes with large surface areas and uniform pore sizes, mesoporous silica has been utilized as a template for the synthesis of nanowires. Mesophase structures self-assembled from surfactants provide specific class of useful and versatile templates for producing 1-D nanostructures in relatively large quantities (Figure 2.8). It is well known that specific micell concentration surfactant molecules spontaneously organize into rod-shaped micelles.[25] These anisotropic structures can be employed as soft templates to promote the formation of nanowires when combined with suitable chemical or electrochemical reaction. The surfactant is required with selective removal to collect the nanowires. Through the template-based growth, various nanowires such as CdS, ZnS, and ZnSe have been synthesized by using surfactants such as Na-AOT and Triton X of known concentrations.[26]

Nanowires themselves can be exploited as templates to generate the nanowires of other materials. The template can be coated to the nanowire fabricating coaxial nanowires, or it can react with the nanowires forming a novel material.[27] From solution or sol-gel coating, nanowires can be directly sheathed with conformal coating layers made of a different material to form coaxial nanowires. Subsequent dissolution of the original nanowires results in nanotubes of the coated materials. The sol-gel coating provides a general way to synthesize coaxial nanowires that contain electrically conductive metal cores and insulating sheaths.

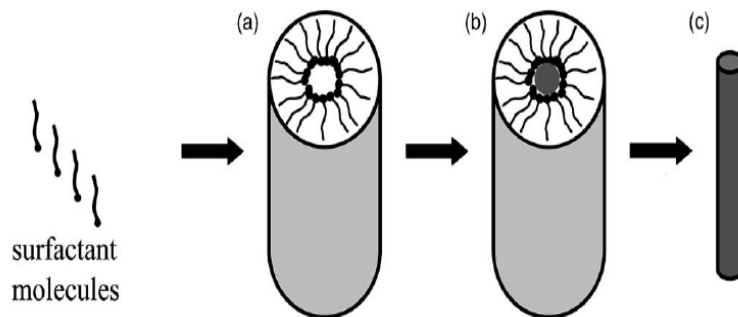


Figure 2.8 Schematic diagram showing the formation of nanowires by templating against mesostructures which are self-assembled from surfactant molecules. (a) Formation of cylindrical micelle; (b) formation of the desired material in the aqueous phase encapsulated by the cylindrical micelle; (c) removal of the surfactant molecule with an appropriate solvent to obtain an individual nanowire.

2.4.2.2 Anisotropic crystal structures

Solid materials such as selenium, tellurium, and molybdenum can be readily synthesized by the governing of anisotropic bonding in the structure.[28] In particular, it dictates the crystallization to occur along the c-axis with preference of the stronger covalent bonds over the relatively weak van der Waals forces between chains.

2.4.2.3 Solution-liquid-solid process

Buhro et al. have studied on synthesis of III-Vsemiconducting nanowires via low temperature solution-liquid-solid (SLS) method.[29] In a this method, a metal with a low melting temperature is employed as a catalyst, decomposition of metal-organic precursor leads to fabrication of the desired nanowires.[30] Nanowires of III-Vsemiconducting nanowires have been synthesized at low temperature (below than 203°C) solution phase reactions. Figure 2.9 illustrates the growth of single-crystalline nanowires via the SLS method.

In addition to the solution-based process for III-Vsemiconducting nanowires, it has been reported that by exploiting the selective capping capacities of mixed surfactants, which extend the synthesis of the II-VI semiconducting nanowires.[31]

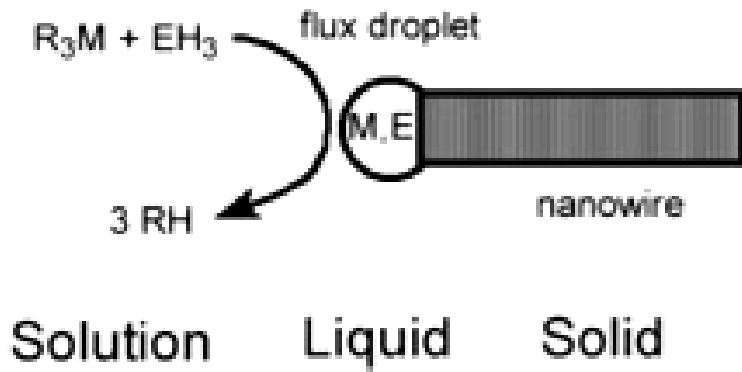


Figure 2.9 Schematic illustration showing the growth of a nanowire through the solution-liquid-solid mechanism.

2.4.2.4 Solvothermal synthesis

Solvothermal synthesis is normally used as a solution route to produce semiconductor nanowires and nanorods. In this process, a solvent is mixed with metal precursors and crystal growth regulating agents. This solution mixture is positioned in an autoclave maintained at relatively high temperatures and pressures to perform with the crystal growth and the assembly process. This method is highly versatile and results in the synthesis of semiconducting nanowires and other materials.

2.5 References

- [1] Joonwoong Lee, “The trend of nanotechnology”, KISTI report, (2004)
- [2] V. I. Klimov, A. A. Mikhailovsky, S. Xu, A. Malko, J. A. Hollingsworth, C. A. Leatherdale, H. J. Eisler, and M. G. Bawendi, *Science*, **290**, 314, (2000)
- [3] V. S. Trubetskoy, *Advanced Drug Delivery Reviews*, **37**, 81, (1999)
- [4] L. E. Brus, *Journal of Chemical Physics*, **80**, 4403, (1984)
- [5] D. L. Klein, R. Roth, A. K. L. Lim, A. P. Alivisatos, and P. L. McEuen, *Nature*, **389**, 699, (1997)
- [6] C. M. Lieber, *MRS Bulletin*, **28**, 486, (2003)
- [7] J. V. Barth, *Appl. Phys. A*, **76**, 645 (2003)
- [8] X. Duan, Y. Huang, Y. Cui, J. Wang, C. M. Lieber, *Nature*, **409**, 66, (2001)
- [9] Y. Cui, C. M. Lieber, *Science*, **291**, 851, (2001)
- [10] Y. Huang, X. Duan, Y. Cui, L. J. Lauhon, K.-H. Kim, C. M. Lieber, *Science*, **294**, 1313, (2001)
- [11] C. Martin, *Science*, **266**, 1961, (1994)
- [12] P. Y. Yiying Wu, *Journal of the American Chemical Society*, **123**, 3165,

(2000)

[13] C. M. Lieber, MRS Bulletin, pp. 486-491, (2003)

[14] R. S. Wagner, W. C. Ellis, Appl. Phys. Lett., **4**, 89, (1964)

[15] Y. Xia, P. Yang, Y. Sun, Y. Wu, B. Mayers, B. Gates, Y. Yin, F. Kim, H. Yan, Adv. Mater., **15**, 353, (2003)

[16] Y. Wu, P. Yang, J. Am. Chem. Soc., **123**, 3165, (2001)

[17] Y. Wu, P. Yang, Chem. Mater., **12**, 605, (2000)

[18] C. C. Chen, C. C. Yeh, Adv. Mater., **12**, 738, (2000)

[19] M. H. Huang, Y. Wu, H. Feick, E. Webber, P. Yang, Adv. Mater., **13**, 113, (2000)

[20] H. J. Fan, F. Bertram, A. Dadgar, J. Christen, A. Krost, M. Zacharias, Nanotechnology, **15**, 1401, (2004)

[21] S. M. Zhou, Y. S. Feng, L. D. Zhang, Chem. Phys. Lett., **369**, 610, (2003)

[22] S. T. Lee, N. Wang, Y. F. Zhang, Y. H. Tang, MRS Bulletin, **20**, 36, (1999)

[23] C. Y. Nam, J. Y. Kim, J. E. Fischer, Appl. Phys. Lett., **86**, 193112, (2005)

- [24] M. Zheng, L. Zhang, X. Zhang, J. Zhang, G. Li, *Chem. Phys. Lett.*, **334**, 298, (2001)
- [25] H. Ringsdorf, B. Schlarb, J. Verzmer, *Angew. Chem. Int. Ed.*, **27**, 113, (1988)
- [26] C. N. R. Rao, A. Govindaraj, F. L. Deepak, N. A. Gunari, M. Nath, *Appl. Phys. Lett.*, **78**, 1853, (2001)
- [27] Y. Yin, Y. Lu, Y. Sun, Y. Xia, *Nano Lett.*, **2**, 427, (2002)
- [28] J. J. Stejny, R. W. Trinder, J. Dlugosz, *J. Mater. Sci.*, **16**, 3161, (1981)
- [29] T. J. Trentler, K. M. Hickman, S. C. Geol, A. M. Viano, P. C. Gibbons, W. E. Buhro, *Science*, **270**, 1791, (1995)
- [30] O. R. Lourie, C. R. Jones, B. M. Bartlett, P. C. Gibbons, R. S. Ruoff, W. E. Buhro, *Chem. Mater.*, **12**, 1808, (2000)
- [31] L. Manna, E. C. Scher, A. P. Alivisatos, *J. Am. Chem. Soc.*, **122**, 12700, (2000)

Chapter 3.

Vapor–liquid–solid growth mechanism of Ag₂S catalyzed ZnS nanowires

3.1 Introduction

During the past few decades, one-dimensional (1D) semiconductor nanowires (NWs) attaining unique electrical, chemical, and optical properties have been researched as important building blocks for realization of various nano-electronic devices [1-3]. This has opened up the potential for various possible applications [4-6] and research on a global scale has been actively pursued. Among the various semiconductor nanomaterials, Zinc sulfide (ZnS) with a wide band gap of 3.7eV has garnered significantly increased attention as a promising electronic material [7-10]. It has been recognized as a suitable material for flat-panel display [11], light-emitting diodes (LEDs) [12], infrared windows sensors [13], electroluminescent devices [14] and lasers [15] fabrication due to its structural and formation diversity and excellent chemical and thermal stability. As a synthesis manner of ZnS NWs, Vapor–Liquid–Solid (VLS), Solution-Liquid-Solid (SLS), Solution-Solid-Solid (SSS), Vapor-Solid-Solid (VSS), and Supercritical Fluid-Solid-Solid (SFSS) [18] have been used [16-19]. Among these methods, the VLS growth method using supersaturated solid after liquid metal-semiconductor droplet formation with absorbed vapor

precursor and metal catalyst has been widely used to synthesize 1D semiconductor nanostructures, which enables nanowire to have the desired size and location through the metal catalyst. Also, many efforts to realize nanowire fabrication were performed with VLS technique on various semiconducting materials and catalysts. However, metal catalysts in semiconductor nanowires synthesized by VLS method can act as impurities affecting the band gap during operation of electronic devices. Regarding disadvantage of metal catalysts in semiconductor NWs, there have been reports on aspects that need to be overcome for future applications to devices [20-23].

Semiconductor NW fabrication using semiconductor catalysts have been studied to overcome the disadvantages of metal catalysts and develop new semiconductor materials. In the case of ZnS, although some research groups have recently reported the application potential of photocatalysts using methods such as SLS and SSS to synthesize nanoparticle/nanowire /nanorods including Ag₂S–ZnS, Ag₂S–CdS, and Ag₂S–AgInS₂ using the Ag₂S semiconductor catalyst [24-27], there have yet to be reports of ZnS NW fabrication employing the VLS synthesis method using the Ag₂S catalyst. Ag₂S, used as a catalyst, is an important semiconductor II-VI group with a high absorption coefficient and ~1eV band gap. With its relatively small band gap, chemical stability, and mixed conducting properties, Ag₂S is an interesting material that can be applied to electrical devices. Recently, Ag₂S has been used in studies on nonvolatile

memory devices functioning at low operating voltages [28-31]. The nanostructures of the Ag₂S semiconductor (bulk $E_g=0.9-1.1$ eV) and ZnS semiconductor (bulk $E_g=3.77$ eV) have high application potential in areas such as photoluminescence emitting/quenching, band gap engineering, photocatalysis, solar energy, electrical circuitry, optical and/or optoelectronic [25,26,32-35]. In this study, we report synthesis of ZnS NWs using the Ag₂S semiconductor catalyst using the simple VLS method utilizing an Ag film and a ZnS precursor. Properties of the synthesized ZnS NWs such as the crystallinity, composition, and structure were analyzed using X-ray Diffractometer (XRD, PANalytical-X'pert Pro), field-emission scanning electron microscopy (FE-SEM, Hitachi-8230), energy-dispersive X-ray spectroscopy (EDS, Oxford- X-MaxN 80T), and transmission electron microscopy (TEM, JEM-ARM200F). Also, the Ag₂S semiconductor catalyst ZnS NW VLS growth mechanism was investigated using in-situ heating TEM. Through real-time observation of ZnS NWs, the transition of ZnS NW and Ag₂S semiconductor catalyst were observed and the results provided valuable insight into understanding the ZnS NW VLS growth mechanism using Ag₂S.

3.2 Experimental

3.2.1 Synthesis of ZnS nanowires

ZnS NWs were synthesized by metalorganic chemical vapor deposition (MOCVD) using an $(\text{Zn}(\text{S}_2\text{CNEt}_2)_2)$ single molecular precursor [36]. The MOCVD equipment with a gold furnace was composed of a 25mm diameter quartz tube and a gas and pressure control system. The Si(100) wafer was cleaned in an acetone solution and sonicated for 10 minutes followed by sonication in a deionized water solution bath for 5 minutes then the wafer was dried using a nitrogen gas. Afterwards, the Ag film (~10nm) to be used as the catalyst was deposited on the cleaned Si wafer for 10 seconds via ion sputtering. $(\text{Zn}(\text{S}_2\text{CNEt}_2)_2)$ powder (Sigma Aldrich) was poured into an alumina boat and Ag coated Si wafers were placed upstream and downstream of the quartz tube. After reducing the pressure of the furnace tube to 0.1torr, Mass flow controller (MFC) was used to allow a 100sccm (SCCM denotes cubic centimeter per minute at standard temperature and pressure (STP)) flow of Ar carrier gas, and the pressure within the quartz tube was maintained at 5torr using the pressure control system as the temperature of the gold furnace was increased at a rate of 1°C per second to 800°C. When the gold furnace temperature reached 800°C, the alumina boat prepared upstream was moved inside the furnace and the temperature was maintained for 1 hour for the ZnS NW synthesis. After 1 hour, the Ar gas flow was blocked and furnace cooling was performed until reaching

room temperature. A nontransparent, white membrane was observed to have formed over the silicon specimen cooled to room temperature.

3.2.2 Characterization method

The crystalline characteristics of the synthesized ZnS NWs were investigated using MF-XRD and their morphology was observed using SEM and Cs-TEM. Focused ion beam (FIB, FEI NOVA200) was used to observe the cross section of the ZnS NWs. A qualitative analysis of the ZnS NWs was conducted using EDS and the decomposition process of the ZnS NWs was observed through in-situ heating TEM using the Aduro heating stage designed by Protochips.

3.3 Results and Discussion

3.3.1 Characterization of ZnS nanowires

XRD was used to analyze the structure of the ZnS NWs synthesized using the Ag₂S catalyst. The XRD spectrum peaks were found to be hexagonal wurtzite phase ZnS with lattice constants of $a=b=3.823\text{\AA}$ and $c=18.743\text{\AA}$, which is well matched with JCPDS (Joint Committee on Powder Direction Standards, card no. 89-2191). Other phases were not observed and the lack of an Ag₂S peak was due to its very small amount in comparison to ZnS (Fig. 3.1a). FE-SEM was used to observe the morphology and growth mechanism of the synthesized ZnS NWs. Fig. 3.1b shows a FE-SEM image of the ZnS NWs synthesized after depositing Ag with a thickness of $\sim 10\text{nm}$ over the Si wafer where Ag is used as the catalyst for the growth. The low magnification SEM image shows typical, uniform formation of ZnS NWs. It can be observed that the formation is consistent over a large area and effective synthesis has taken place. The length and width of the ZnS NWs intricately grown on the Si wafer were in the ranges of a few μm and a few tens of nm. The right inset of Fig. 3.1(b) shows a high magnification SEM image of the ZnS NWs. The spherical forms on the end of the ZnS NWs appear to be the Ag₂S catalyst grown through the VLS method.

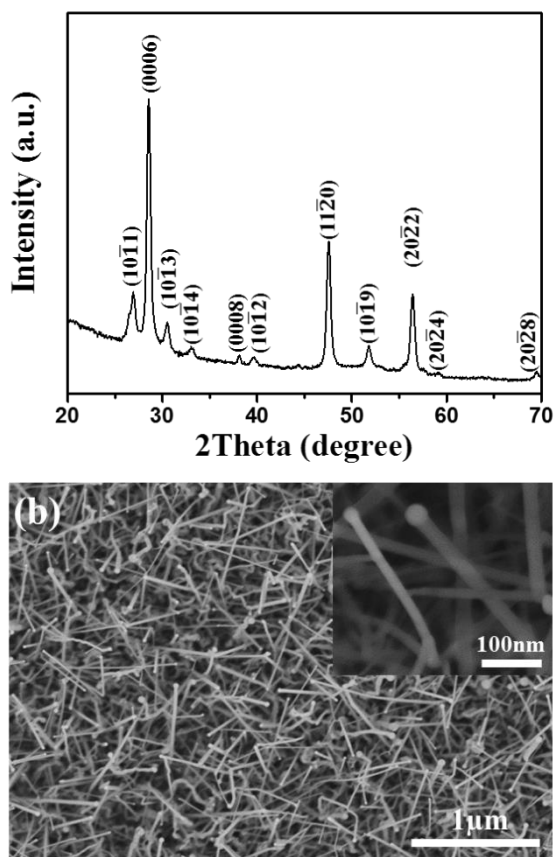


Figure 3.1 (a) XRD pattern of ZnS nanowires. The peaks are identified with a wurtzite 6H ZnS structure with lattice constants $a = 3.823 \text{ \AA}$, $c = 18.743 \text{ \AA}$. (b) Low-magnification SEM image of Ag₂S catalyzed ZnS nanowires. Inset in (b) is high-magnification SEM image.

3.3.2 Structural analysis of ZnS nanowires

A detailed morphology analysis of the ZnS NWs was conducted using TEM. To enable the TEM analysis, the ZnS NWs were directly scattered on a SiN film on the TEM grid. Fig. 3.2a shows a low magnification TEM image of typical ZnS NWs with the Ag₂S catalyst shown as dark spherical forms on the ends of the ZnS NWs. Moreover, high resolution (HR) annular dark field (ADF)-scanning TEM (STEM) was used to conduct a structural analysis of the ZnS NWs. Fig. 3.2b shows HR ADF-STEM image of the single ZnS NW, which exhibits highly crystallized lattice fringes for both the catalyst and wire. From the HR ADF-STEM image, the growth direction of ZnS NW was revealed [0001] direction with the interplanar spacing of 3.12Å in wurzite structure. The catalyst part showed a (110) lattice plane with an interplanar spacing of 3.44Å, which display [110] growth direction. (JCPDS card no. 65-4429) In order to analyze the chemical composition of the ZnS NW, EDS point, line scan, and mapping were conducted. Fig. 3.2b shows the EDS line scan profiles in the growth direction overlaid on the HR ADF-STEM image of the ZnS NW. Uniform Zn(blue) and S(yellow) element distributions are observed at the ZnS NW region, and Zn(blue) decreases while Ag(red) increases moving towards the catalyst part. The S (yellow) element was observed to be constant throughout the ZnS NW. The point EDS spectra of the ZnS NW and catalyst regions support this observation (Figs. 3.2c and d), and the EDS mapping

results of the ZnS NW support the finding that the ZnS NW using the Ag₂S catalyst was grown using the VLS method (Figs. 3.2e~h).

In order to definitively identify the growth direction and crystalline structure of the ZnS NW, FIB was used to perform cross-sectioning of the ZnS NWs to prepare a TEM sample. Fig. 3.3a is a cross-sectional TEM image where the typical hexagonal shaped ZnS NW with a diameter of approximately 80nm has a [0001] zone axis. Through the EDS mapping results, it was found that the ZnS NWs were composed of Zn (blue) and S (yellow) elements (Figs. 3.3b and c). Fig. 3.3d is a HR ADF-STEM image of the area marked with a red square in Fig. 3.3a, and the right inset shows the fast Fourier transformation (FFT) with [0001] zone axis. The left inset shows an atomic structure schematic diagram of the wurtzite ZnS viewed from the [0001] direction, which is well matched with HR ADF-STEM regarding Z-contrast between Zn and S. For better understanding of ZnS NW, representative atomic structure of ZnS NW is displayed in Fig. 3.3e

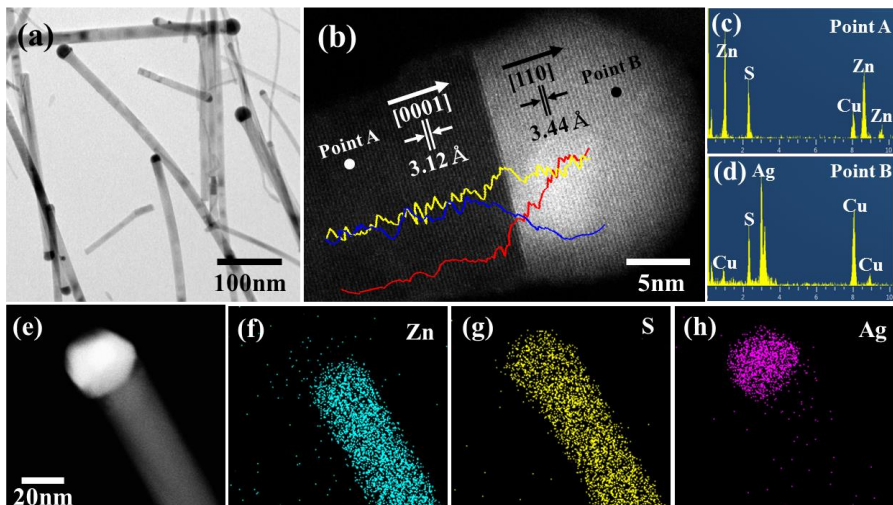


Figure 3.2 (a) A bright field TEM image of Ag_2S catalyzed ZnS nanowires. (b) HR-STEM image of a ZnS nanowire with a catalytic Ag_2S tip growing along $[0001]$ direction. The spacing between adjacent lattice fringes is 0.312 nm. (c),(d) EDS spectrum recorded on the ZnS nanowire (Point A) and the Ag_2S tip (Point B), respectively. HR-STEM image of ZnS nanowire with corresponding EDS line-scan profile along the growth direction. (Blue: Zn, Red: Ag, Yellow: S) (e) STEM image and high resolution STEM-EDS elemental mappings of (f) Zn, (g) S and (h) Ag.

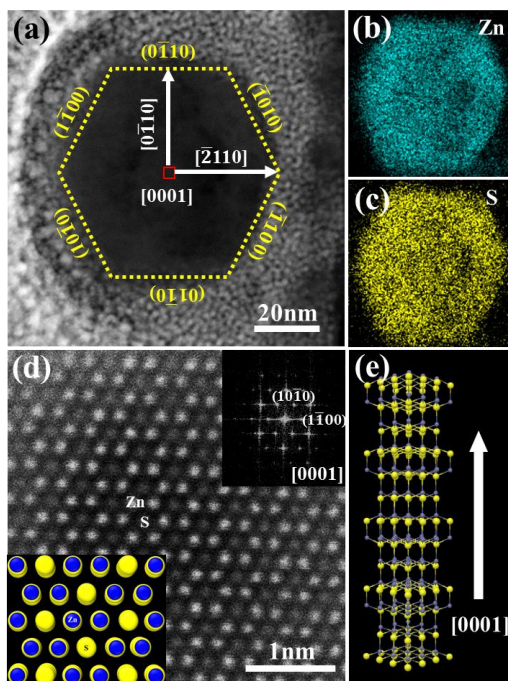


Figure 3.3 TEM images of ZnS nanowire: Cross-sectional TEM images, and high-resolution TEM image of ZnS nanowire. (a) ZnS nanowire with a hexagonal cross-section. (b), (c) HAADF-STEM characterization of the (a) and elemental mapping of Zn (blue) and S(yellow) (d) A high-resolution STEM image obtained from a cross-section of a ZnS nanowire and the corresponding FFT pattern indexed to wurtzite ZnS nanowire show that a ZnS nanowire grows along a $[0001]$ direction. Inset in (d) is illustration of ZnS atomic structure (blue, Zn; yellow, S) (e) Simulated model illustrates the atomic structure of the ZnS nanowire (blue, Zn; yellow, S)

3.3.3 In-situ heating of ZnS nanowire

To gain better insight of ZnS NW using Ag₂S catalyst based on VLS growth mechanism, in-situ heating of the ZnS NWs was carried out inside the TEM. Firstly, ZnS NWs were dispersed on thin carbon membrane chip to prepare for in-situ heating TEM experiment. In-situ heating experiment was conducted from room temperature to 900°C using an in-situ holder. The heating rate was 1°C per second and a video recording of the NW changes during the experiment were made. Fig. 3.4 shows representative frames of the ZnS NW variation from the in-situ heating movie. Fig. 3.4a is a TEM image of the ZnS NW before the in-situ heating experiment. It can be observed that a C-shell has formed on the ZnS NW when heated to around 400°C (Fig. 3.4b). Conceivably, we believe that C-shell is formed from diffusion of amorphous carbon membrane during in-situ heating process. To verify composition of C-shell, we carried out point EDS spectra of carbon tube and carbon membrane in supplementary information. From the EDS results, we only found increased carbon composition at carbon tube compared to bare carbon membrane. Also C-shell is reported as typical product during in-situ heating TEM using carbon TEM grid [37,38]. For temperatures above 500°C, a converse reaction such as solid-liquid-vapor (SLV) to the VLS mechanism takes place. It could be observed that the Ag₂S catalyst melted in the ZnS NW direction, forming the alloy Zn-S-Ag in a liquid phase from the interface between Ag₂S and the ZnS NWs (Fig.

3.4c). Subsequently, the ZnS NW was found to melt from the bottom of that at over 800°C (Fig. 3.4d). The ZnS NWs continuously migrated towards the previous Ag₂S catalyst area and evaporated, where the ZnS NW length and diameter simultaneously decreased (Figs. 3.4e-f). Finally, Ag₂S catalyzed ZnS NW was all vaporized above 840°C, leaving only the C-shell tube (Fig. 3.4g).

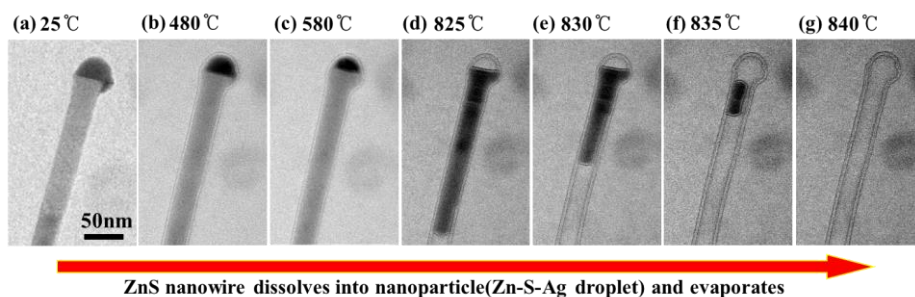


Figure 3.4 Representative frames from movies of nanowire heating experiments (a) TEM image of as-grown Ag_2S catalyzed ZnS nanowire taken at room temperature prior to the in-situ annealing experiments. (b) TEM images showing a ZnS nanowire encapsulated in carbon shells during in-situ annealing at temperature between room temperature and 480 °C. (c) Exchange of material across the ZnS nanowire/liquid drop interface after the assembly of the shell and the melting of the alloy Zn-S-Ag nanoparticle. (d-f) A pure ZnS nanowire dissolves and evaporates into nanoparticle (Zn-S-Ag droplet) while the diameter of the wire simultaneously decreases. (g) In-situ assembly of the carbon tube.

3.3.4 Growth mechanism

Through the in-situ heating experiment, the VLS growth mechanism of the ZnS NWs synthesized using the Ag₂S catalyst was suggested on the basis of the following four steps: (1) The ZnS powder evaporates at high temperatures (800°C), separating into Zn(v) and S(v) precursors. (2) Here, the Ag thin film of ~10nm thickness coating on the Si wafer minimizes the surface energy and forms spherical Ag droplets of a liquid phase, while the gaseous Zn(v) and S(v) precursors are dissolved into the Ag droplets. The reaction between Ag and S is thermodynamically favored, and hence Ag₂S is formed first and the continuously provided Zn and S are dissolved into the Ag₂S droplet in the ZnS form. (3) After ZnS is maximally dissolved into the Ag₂S droplet, the supersaturated ZnS is precipitated in a solid phase to form NWs. (4) Below the eutectic temperature from natural cooling, the Ag₂S-ZnS liquid droplet remains on the top of the NWs with precipitated ZnS NW. Regarding above experimental results, Fig. 3.5 explains the Ag₂S catalyzed ZnS NW growth phenomena in detail. We believe that the in-situ heating TEM results show SLV reaction of Ag₂S catalyzed ZnS NW to support growth based on the VLS mechanism.

Through the simple VLS method using the Ag thin film, synthesis of semiconductor ZnS NWs using an Ag₂S catalyst was carried out. The structural and chemical analyses of the product were confirmed to Ag₂S catalyzed wurzite

ZnS NW based on VLS growth mechanism. Furthermore, in-situ heating experiments were performed to observe that the SLV process is the exact reverse of the VLS process and to investigate the synthesis mechanism of the Ag₂S catalyzed ZnS NW. We believe that semiconductor NW using semiconductor material catalyst such as our finding could be one of the helpful strategy to realize future electronic devices.

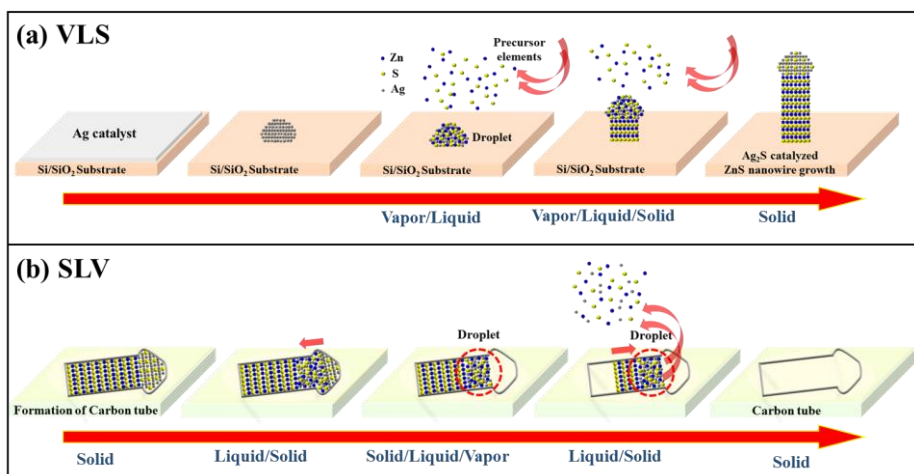


Figure 3.5 Growth and dissolution mechanisms of Ag₂S catalyzed ZnS nanowire: (a) vapor–liquid–solid growth; (b) solid-liquid vapor–dissolution.

3.4 Conclusion

In summary, we researched the Ag₂S catalyzed ZnS NWs based on VLS growth mechanism by MOCVD with Ag thin film. The Ag₂S catalyzed ZnS NWs were confirmed with wurzite structure possessing length and width in the ranges over ~1 μ m and ~30nm to ~80nm. Through extensive TEM analysis, the growth direction of ZnS NW was examined with c-axis [0001] from plane and cross-sectional viewpoint. Additionally, the catalyst at the top of ZnS NW was found to single crystalline Ag₂S. To gain better insight of VLS growth mechanism, in-situ heating TEM experiment was conducted from room temperature to 840°C. As a result, the dissolution of Ag₂S catalyst toward ZnS NW was firstly observed around 480°C with C-shell. Subsequently, melting of Ag₂S catalyst toward ZnS NW was completed melted at around 825°C. As the temperature increased, dissolved Ag₂S and ZnS NW continuously melted and vaporized until 840 °C with only the C-shell. Finally, the possible growth mechanism of Ag₂S and ZnS NW was suggested based on experimental investigation. We believe our finding such as semiconductor NW using semiconductor catalyst could potentially be used for future electronic nano-devices.

3.5 References

- [1] C.M. Lieber, Z.L. Wang, Functional nanowires MRS Bull. 32 (2007) 99-104.
- [2] Y. Xia, P. Yang, Y. Sun, Y. Wu, B. Mayers, B. Gates, Y. Yin, F. Kim, H. Yan, One-dimensional nanostructures: synthesis, characterization, and applications, Adv. Mater. 15 (2003) 353-389.
- [3] C. Weisbuch, B. Vinter, Quantum Semiconductor Structures; Physics and Applications, Academic Press, Boston (1991)
- [4] M.I. van der Meulen, N. Petkov, M.A. Morris, O. Kazakova, X. Han, K.L. Wang, A.P. Jacob, J.D. Holmes, Single crystalline Ge_{1-x}Mnx nanowires as building blocks for nanoelectronics, Nano Lett. 9 (2008) 50-56.
- [5] X.D. Wang, C.J. Summers, Z.L. Wang, Large-scale hexagonal-patterned growth of aligned ZnO nanorods for nano-optoelectronics and nanosensor arrays, Nano Lett. 4 (2004) 423-426.
- [6] M. Hamedi, A. Herland, R.H. Karlsson, O. Inganäs, Electrochemical devices made from conducting nanowire networks self-assembled from amyloid fibrils and alkoxy-sulfonate PEDOT, Nano Lett. 8 (2008) 1736-1740.
- [7] X. Fang, T. Zhai, U. Gautam, ZnS nanostructures: from synthesis to applications, Prog. Mater. Sci. 56 (2011) 175-287.

- [8] T.Y. Zhai, L. Li, Y. Ma, M.Y. Liao, X. Wang, X.S. Fang, J. Yao , Y. Bando , D. Golberg, One-dimensional inorganic nanostructures: synthesis, field-emission and photodetection, *Chem. Soc. Rev.* 40 (2011) 2986-3004.
- [9] F. Gode, C. Gumus, M. Zor, Investigations on the physical properties of the polycrystalline ZnS thin films deposited by the chemical bath deposition method, *J. Cryst. Growth* 299 (2007) 136-141.
- [10] X. Wang, H. Huang, B. Liang, Z. Liu, D. Chen, G. Shen, ZnS nanostructures: synthesis, properties, and applications, *Crit. Rev. Solid State Mater. Sci.* 38 (2013) 57–90.
- [11] X. Liu, X. Cai, J. Mao, C. Jin, ZnS/Ag/ZnS nano-multilayer films for transparent electrodes in flat display application, *Appl. Surf. Sci.* 183 (2001) 103-110.
- [12] J. Ziegler, S. Xu, E. Kucur, F. Meister, M. Batentschuk, F. Gindele, T. Nann, Silica-Coated InP/ZnS Nanocrystals as Converter Material in White LEDs, *Adv. Mater.* 20 (2008) 4068-4073.
- [13] P. Calandra, M. Goffredi, V.T. Liveri, Study of the growth of ZnS nanoparticles in water/AOT/n-heptane microemulsions by UV-absorption spectroscopy, *Colloids Surf. A* 160 (1999) 9-13.
- [14] H.S. Yang, P.H. Holloway, B.B. Ratna, Photoluminescent and electroluminescent properties of Mn-doped ZnS nanocrystals, *J. Appl. Phys.* 93

(2003) 586-592.

[15] X. Fang, Y. Bando, U.K. Gautam, T. Zhai, H. Zeng, X. Xu, M. Liao, D. Golberg, ZnO and ZnS nanostructures: ultraviolet-light emitters, lasers, and sensors, *Crit. Rev. Solid State Mater. Sci.* 34 (2009) 190-223.

[16] N. Dasgupta, J. Sun, S. Brittman, J. Andrews, H. Lim, R. Gao, P. Yan, Yang, 25th anniversary article: semiconductor nanowires—synthesis, characterization, and applications, *Adv. Mater.* 26 (2014) 2137–2184.

[17] D.D. Fanfair, B.A. Korgel, ZnE (E= S, Se, Te) Nanowires Grown by the Solution-Liquid-Solid Mechanism: Importance of Reactant Decomposition Kinetics and the Solvent, *Cryst. Growth Des.* 8 (2008) 3246-3252.

[18] J. Wang, K. Chen, M. Gong, B. Xu, Q. Yang, Solution–solid–solid mechanism: superionic conductors catalyze nanowire growth, *Nano Lett.* 13 (2013) 3996–4000.

[19] D.S. Kim, P. Shimpi, P.X. Gao, Zigzag Zinc Blende ZnS Nanowires: Large Scale Synthesis and Their Structure Evolution Induced by Electron Irradiation, *Nano Res.* 2 (2009) 966-974.

[20] J.H. Woodruff, J.B. Ratchford, I.A. Goldthorpe, P.C. McIntyre, C.E.D. Chidsey, Vertically Oriented Germanium Nanowires Grown from Gold Colloids on Silicon Substrates and Subsequent Gold Removal, *Nano Lett.* 7 (2007) 1637-1642.

- [21] J.V. Wittemann, W. Münchgesang, S. Senz, V. Schmidt, Silver catalyzed ultrathin silicon nanowires grown by low-temperature chemical-vapor-deposition, *J. Appl. Phys.* 107 (2010) 096105.
- [22] S. Barth, J.J. Boland, J.D. Holmes, Defect transfer from nanoparticles to nanowires, *Nano Lett.* 11 (2011) 1550-1555.
- [23] K.A. Dick, P. Caroff, Metal-seeded growth of III–V semiconductor nanowires: towards gold-free synthesis, *Nanoscale* 6 (2014) 3006-3021.
- [24] G. Zhu, Z. Xu, Controllable growth of semiconductor heterostructures mediated by bifunctional Ag₂S nanocrystals as catalyst or source-host, *J. Am. Chem. Soc.* 133 (2011) 148-157.
- [25] S. Chen, S. Thota, G. Reggiano, J. Zhao, Generalized seeded growth of Ag-based metal chalcogenide nanorods via controlled chalcogenization of the seeds, *J. Mater. Chem. C* 3 (2015) 11842-11849.
- [26] P.J. Wu, J.W. Yu, H.J. Chao, J.Y. Chang, Silver-based metal sulfide heterostructures: synthetic approaches, characterization, and application prospects, *Chem. Mater.* 26 (2014) 3485-3494.
- [27] C. Zou, M. Li, L. Zhang, Y. Yang, Q. Li, X. Chen, X. Xu, S. Huang, Ag₂S-catalyzed growth of quaternary AgInZn₇S₉ semiconductor nanowires in solution, *Cryst. Eng. Comm.* 13 (2011) 3515-3520.

- [28] I.C. Lekshmi, G. Berera, Y. Afsar, G.X. Miao, T. Nagahama, T. Santos, J.S. Moodera, Controlled synthesis and characterization of Ag₂S films with varied microstructures and its role as asymmetric barrier layer in trilayer junctions with dissimilar electrodes, *J. Appl. Phys.* 103 (2008) 093719.
- [29] Y. Zhang, G.S. Hong, Y.J. Zhang, G.C. Chen, F. Li, H.J. Dai, Q.B. Wang, Ag₂S quantum dot: a bright and biocompatible fluorescent nanoprobe in the second near-infrared window, *ACS Nano* 6 (2012) 3695-3702.
- [30] Y. Du, B. Xu, T. Fu, M. Cai, F. Li, Y. Zhang, Q. Wang, Near-infrared photoluminescent Ag₂S quantum dots from a single source precursor, *J. Am. Chem. Soc.* 132 (2010) 1470-1471.
- [31] Z. Xu, Y. Bando, W. Wang, X. Bai, D. Golberg, Real-time in situ HRTEM-resolved resistance switching of Ag₂S nanoscale ionic conductor, *ACS Nano* 4 (2010) 2515-2522.
- [32] G. Murugadoss, R. Jayavel, M.R. Kumar, R. Thangamuthu, Synthesis, optical, photocatalytic, and electrochemical studies on Ag₂S/ZnS and ZnS/Ag₂S nanocomposites, *Appl. Nanosci.*, 6 (2016) 503-510.
- [33] S.L. Shen, Y.J. Zhang, L. Peng, Y.P. Du, Q.B. Wang, Matchstick-shaped Ag₂S–ZnS heteronanostructures preserving both UV/blue and near-infrared photoluminescence, *Angew. Chem. Int. Ed.* 50 (2011) 7115-7118
- [34] S. Shen, Y. Zhang, Y. Liu, L. Peng, X. Chen, Q. Wang, Manganese-Doped

Ag₂S-ZnS Heteronanostructures, *Chem. Mater.* 24 (2012) 2407-2413.

[35] T. Zhu, C. Zhang, G.W. Ho, In Situ Dissolution–Diffusion toward Homogeneous Multiphase Ag/Ag₂S@ ZnS Core–Shell Heterostructures for Enhanced Photocatalytic Performance, *J. Phys. Chem. C* 119 (2015) 1667-1675.

[36] Z. Q. Wang, X. D. Liu, J. F. Gong, H. B. Huang, S. L. Gu and S. G. Yang, Epitaxial Growth of ZnO Nanowires on ZnS Nanobelts by Metal Organic Chemical Vapor Deposition, *Cryst. Growth. Des.* 8 (2008) 3911-3913.

[37] E. Sutter, P. Sutter, Au-induced encapsulation of Ge nanowires in protective carbon shells, *Adv. Mater.* 18 (2006) 2583-2588.

[38] E. Sutter, P. Sutter, Y.M. Zhu, Assembly and Interaction of Au/C Core–Shell Nanostructures: In Situ Observation in the Transmission Electron Microscope, *Nano Lett.* 5 (2005) 2092-2096.

Chapter 4.

Visualization of Three-Dimensional Morphology of Hierarchically-Assembled ZnS Nanostructures by Corroborated Electron Tomography and 3D Printing

4.1 Introduction

Development of nanotechnology has an impact on all areas of science. With rapid progress of nano-objects and nanostructured materials over the past few years, especially at the materials science, there are an escalating need for novel tools dedicated to the structural characterization of qualitative and quantitative analysis at the nanometer level.[1-5] There is a need to explore the basic physical and chemical properties of nanomaterials that can subsequently exploit these properties on a technical level. The ultimate goal is to incorporate as innovative analytical system and of the device can be applied to a real application. Accordingly, accurate characterization of nanomaterials plays an important key role in the synthesis and production of the required material.[6-11]

3D TEM tomography and 3D printing is emerging as a useful tool with powerful technologies that provide information about nanomaterials.[13-15] These techniques overcome the limitations such as exact shape and location of

the nano-particles cannot be obtained from a 2D image by enabling the visualization of the overall shape and localized features, including the individual particle sizes and shapes of materials on a nanoscale.[16-22] Further, since properties of nanomaterials strongly influenced by its structure, it is important for us to appreciate and understand the structure itself. But it can be challenging to understand because of the often complex nanostructure of the periodic domain or the entangled shapes of nanoparticles.[22-28] In order to solve this problem, the visualization of complex nanostructures by using a 3D print would be a good way to improve the understanding of the nanostructure.[29-31]

In this communication, we demonstrate a shape controllable ZnS nanostructures having two different growth mechanisms of the one-step synthesis. The technical development will most certainly occur in the near future, reducing the gap between nano-imaging and high-tech materials. New Suggestion for 3D spatial design will be useful for educators, students, and researchers in material science and nanotechnology.

4.2 Experimental section

4.2.1 Synthesis and characterization

The ZnS nanowires and ZnS nanostructures were synthesized in a horizontal two-temperature zone tube gold furnace system. . After the 1.0cm x 3.0 cm Silicon (100) wafers were cleaned, the Ag film (~10nm) to be used as the catalyst was deposited on the cleaned Si wafer for 10 seconds via ion sputtering. ZnS powder (Zinc diethyldithiocarbamate (SIGMA-ALDRICH, CAS number: 14324-55-1)) (0.1mg) was poured into an alumina boat was placed upstream of the quartz tube. Ag coated two Si wafers were located on each side of Zone 1 and 2 in the downstream of the quartz tube. A schematic of the metalorganic chemical vapor deposition (MOCVD) apparatus is shown in figure 1a. After reducing the pressure of the furnace tube to 0.1torr, Mass flow controller (MFC) was used to allow a 100sccm (standard cubic centimeter per minute) flow of Argon gas (99.999% purity), and the pressure within the quartz tube was maintained at 5torr using the pressure control system. Temperature zones 1 of the furnace were increased at a rate of 1 degree per second to 900 °C, and temperature zone 2 was not specifically heated during the growth. When the gold furnace temperature reached 900 °C, the alumina boat prepared upstream was moved inside the furnace. The growth was continued for 20 min. After the reaction was terminated and the furnace was cooled to room temperature, a nontransparent and gray-colored products was observed to have formed over

silicon substrates cooled to room temperature.

The morphologies and microstructures of the as-synthesized products were systematically characterized. The crystalline characteristics of the synthesized ZnS nanostructures were investigated using MF-XRD and their morphology was observed using field emission scanning electron microscopy (FE-SEM) and Cs-TEM. Focused ion beam (FIB, FEI NOVA200) was used to observe the cross section of the ZnS nanostructures. A qualitative analysis of the ZnS nanostructures was conducted using energy dispersive X-ray spectrometer (EDS).

Moreover, STEM was used to conduct a structural analysis of the ZnS nanostructure. The single ZnS nanostructure ADF image of Fig. 4.2b shows that ZnS nanoparticles have been shown in the whole area around the nanowire. In order to analyze the chemical composition of the ZnS nanostructure, EDS point and mapping were conducted.

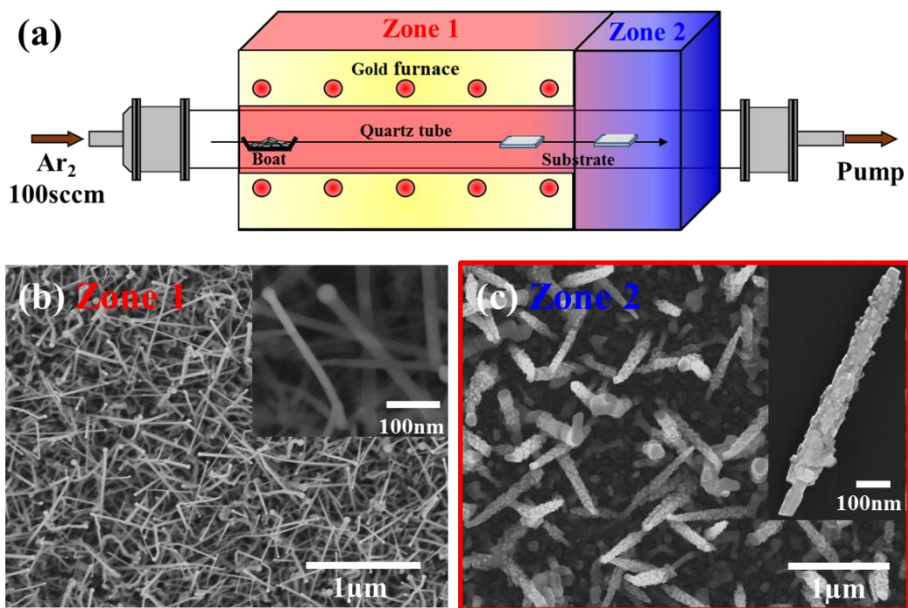


Figure 4.1 (a) The schematic diagram of the two distinctive grow zones inside the quartz tube for the synthesis of ZnS nanostructures by the MOCVD method. SEM images of as-synthesized ZnS nanostructures formed in zone 1 and 2. (b) ZnS nanowires. (c) ZnS nanostructures. The insets are high-magnification SEM images of ZnS nanostructures.

4.2.2 TEM tomography and 3D printing

TEM tomography was performed using the automated tilt-series acquisition software tomography on a JEOL-ARM operated at 200 kV. The first step in TEM tomography is recording TEM images while tilting the sample over a wide range of angles with small increments. For the ZnS nanowires coated with nanoparticles, JEOL rotation holder was employed to collect bright field (BF) images in a JEOL-ARM TEM. The tilt of the JEOL rotation is motor driven from 0 to 360°. For each reconstruction, 160 BF images were collected at 1° tilt intervals in a tilt range of -80° to +80°. Tomography software performs complete automatic acquiring of sequential tilted TEM images series essential for tomographical 3D image reconstruction. Algorithms corresponding to inherent problems, such as correction of shifted position when specimen tilted, and maintenance of focus are applied automatically. After data acquisition all BF TEM images are aligned with respect to a common origin and tilt axis. In the next step a 3D reconstruction of the imaged sample is computed using specialized algorithms such as filtered back-projection (FBP), the simultaneous iterative reconstruction technique (SIRT). The 3D reconstruction provides the basis to visualize the ZnS nanostructure morphology.

1. Software and Equipment
2. Preparation of 3D Printable .stl Nanostructure Files (3D Design and Mathematical Graphing)

3. Preparation of 3D Printable .stl Nanostructure Files

4. 3D Printing the Nanostructures

The basic steps of the tomographic method are illustrated in Fig. 4.3

4.3 Results and Discussion

4.3.1 Morphology of ZnS nanostructure

The products were first analyzed using FE-SEM (Fig. 4.1b, c). Fig. 4.1b and c are the SEM images of the ZnS nanowires and nanostructure, respectively. High magnification SEM image of typical the ZnS nanowires and nanostructures are shown in right inset of Fig 4.1b and c. Both of them can be observed that the formation is consistent over a large area and effective synthesis has taken place. The ZnS nanowires exhibit clearly that the typical length and diameter of the individual nanowire range of a few μm and a few tens of nm, respectively. The spherical forms on the end of the ZnS nanowires appear to be the catalyst grown through the VLS method. The ZnS nanostructure displays that each ZnS nanowire was decorated by a considerable amount of nanoparticles with size <10 nm which show that thickness of 50-100 nm and length of ~ 1 μm , respectively. The nanoparticles coating is exceptionally uniform throughout the wire length. Through the ZnS nanostructure morphology, it was synthesized VLS and VS growth process since nanoparticles can be seen uniform distribution on the surface of nanowire, which is agreement with the experimental condition of catalyst showed at the tips of nanowire. The coexistence of different morphologies of nanomaterials indicates that the growth of nanostructures can be controlled by the growth mechanism in the gold furnace with two distinctive temperature zones. Using

this method created a nanostructure for TEM tomography.

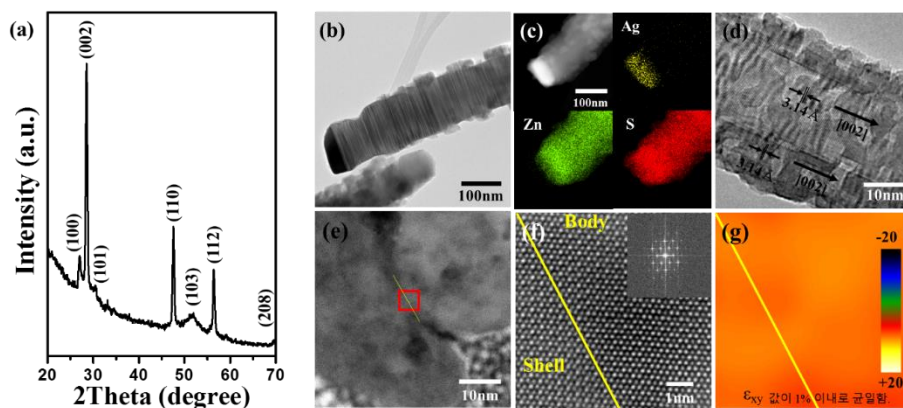


Figure 4.2 (a) XRD pattern of ZnS nanostructures. The peaks are identified with a wurtzite 2H ZnS structure with lattice constants $a = 3.836\text{\AA}$, $c = 6.277\text{\AA}$. (b) A bright field TEM image of ZnS nanostructure. (c) STEM image and high resolution STEM-EDS elemental mappings of Zn, S and Ag. (d) HR-STEM image of a ZnS nanostructure with a catalytic Ag_2S tip growing along [002] direction. The spacing between adjacent lattice fringes is 0.314nm . (e) Cross-sectional TEM images between ZnS nanowire and nanoparticle. (f) HR-STEM image between ZnS nanowire and nanoparticle. (g) GPA simulation map.

4.3.2 Structural Analysis of ZnS nanostructure

The crystal structure of the as-obtained product was characterized by XRD. All of the strong reflection peaks were found to be hexagonal wurtzite phase ZnS with lattice constants of $a=b=3.836\text{\AA}$ and $c=6.277\text{\AA}$, which is well matched with JCPDS (Joint Committee on Powder Diffraction Standards, card no. 75-1547). Other phases were not observed and the lack of an Ag_2S peak was due to its very small amount in comparison to ZnS (Fig. 4.2a).

A detailed morphology analysis of the ZnS nanostructure was conducted using TEM. To enable the TEM analysis, the ZnS nanostructures were directly scattered on a SiN film on the TEM grid. Fig. 4.2b shows a BF TEM image of typical ZnS nanostructure with the Ag_2S catalyst shown as dark elliptical forms on the ends of the ZnS nanostructure. ZnS nanoparticles have been shown in the whole area around the nanowire. In order to analyze the chemical composition of the ZnS nanostructure, EDS point and mapping were conducted. Fig. 4.2c shows the EDS mapping on the ADF image of the ZnS nanostructure. Uniform Zn(green) and S(red) element distributions are observed at the ZnS nanowire region, while Ag(yellow) is observed the catalyst part. It is finding that the ZnS nanowire using the Ag_2S catalyst was grown using the VLS method and then ZnS nanoparticle around nanowire was grown using the VS method. The microstructures of the as-synthesized ZnS nanostructures were further studied using the TEM images of an individual ZnS nanowire and nanoparticle

in Fig. 4.2d, respectively. The HR-TEM image of Fig. 4.2d is a magnified presentation of the single ZnS nanostructure in order to examine the detailed crystal structure. It shows highly crystallized lattice fringes for both the ZnS nanowire and nanoparticle. From the lattice image, the interplanar spacing of 0.314 nm perpendicular to the ZnS nanowire axis was exactly the (002) lattice plane and the ZnS growth was in the [002] direction of the wurtzite ZnS. In addition, the ZnS nanoparticle showed a (002) lattice plane with an interplanar spacing of 0.314nm and ZnS growth was in the [002] direction. As a result, it was confirmed that the growth direction is equal both the ZnS nanowire and nanoparticle.

In order to definitively identify the growth direction and crystalline structure of the ZnS nanostructures, FIB was used to perform cross-sectioning of the nanostructures to prepare a TEM sample. Fig. 4.2e is a cross-sectional BF TEM image where the hexagonal shaped ZnS nanowire with a diameter of approximately 80nm has decorated nanoparticles. Properties such as nanoparticles size, distribution and location are critical for the gas sensing performance. A property that can only be evaluated by TEM tomography is the 3D location of the nanoparticles with respect to the support, e.g. on the surface, grain boundaries.

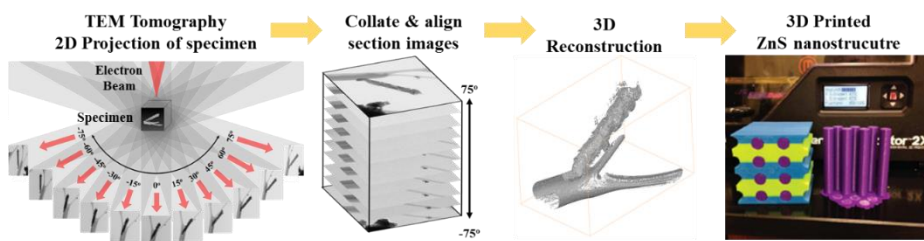


Figure 4.3 Illustration of TEM tomography data acquisition, 3D reconstruction and 3D printing process. Series of 2D images acquired of ZnS nanostructure at different viewing angles. 2D projected images combined into image stack ordered by viewing angle. Tilt series is aligned, and reconstruction algorithm is applied to produce 3D reconstruction of ZnS nanostructure. The ZnS nanostructure was output using 3d printing.

4.3.3 3D TEM tomography

We applied BF TEM tomography to study the 3D structure of ZnS nanoparticles coated ZnS nanowires as well. Several sets of tilted BF images were collected at tilt intervals of two degrees from -80° to 80° by using the rotation holder on the JEOL ARM. Fig.4 shows five BF images of a ZnS nanoparticles coated ZnS nanowire tilted at -70° , -35° , 0° , 35° , and 70° , respectively (Fig 4.4).

The shape and location of the nanoparticles are revealed in the reconstructed volume of the nanowire as shown in Fig. 4.5b. Inspection of the reconstructed model as well as cross sections typified by Fig.4.5d shows that the nanoparticles are most often found around nanowire. A crucial aspect of electron tomography is in segmenting the features of interest from the 3D reconstructions and quantitatively describing their properties.

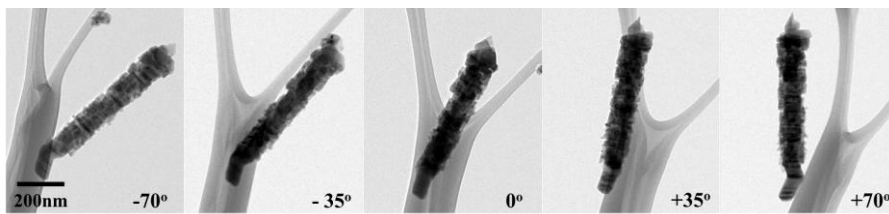


Figure 4.4 Different angles BF TEM images of a tomographic series recorded from the ZnS nanostructure.

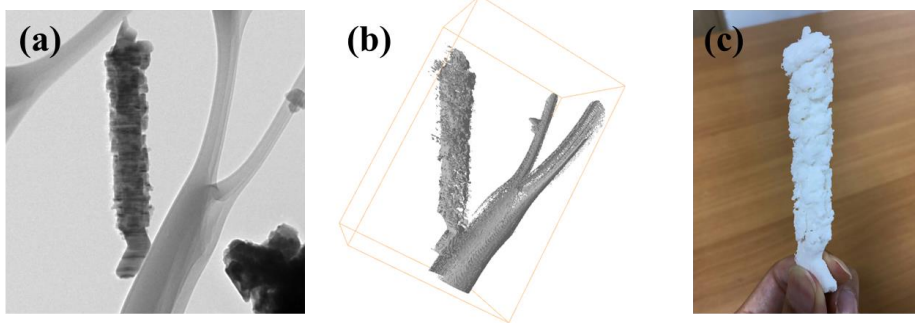


Figure 4.5 Visualizations: from 2D to 3D at nanoscales to 3D at macroscales.

4.3.4 Growth mechanism of ZnS nanostructures

The nanostructures may grow via VLS mechanism combined with a VS mechanism. Through the two-temperature zone tube gold furnace synthesis, the VLS and VS growth mechanism of the ZnS nanostructure synthesized using the Ag_2S catalyst was explained on the basis of the following five steps: (1) The ZnS powder evaporates at high temperatures (900 degrees), separating into $\text{Zn}(\text{v})$ and $\text{S}(\text{v})$ precursors. (2) Here, the Ag thin film of ~10nm thickness coating on the Si wafer minimizes the surface energy and forms spherical Ag droplets of a liquid phase, while the gaseous $\text{Zn}(\text{v})$ and $\text{S}(\text{v})$ precursors are dissolved into the Ag droplets. The reaction between Ag and S is thermodynamically favored, and hence Ag_2S is formed first and the continuously provided Zn and S are dissolved into the Ag_2S droplet in the ZnS form. (3) After ZnS is maximally dissolved into the Ag_2S droplet, the supersaturated ZnS is precipitated in a solid phase to form nanowires at the nucleation temperature. (4) At temperature below the eutectic temperature, due to the high supersaturation of ZnS, the $\text{Zn}(\text{v})$ and $\text{S}(\text{v})$ precursors directly deposited on the nucleation in a solid mode to grow ZnS nanoparticles around ZnS nanowires. This process was controlled by a VS mechanism. (5) When the synthesis is completed, the Ag_2S remains on the top of the nanowires and ZnS nanoparticles coated ZnS nanowires is precipitated in nanostructure form. Therefore, the growth of ZnS nanostructures involved both a VLS mechanism

and a VS mechanism (Fig 4.6).

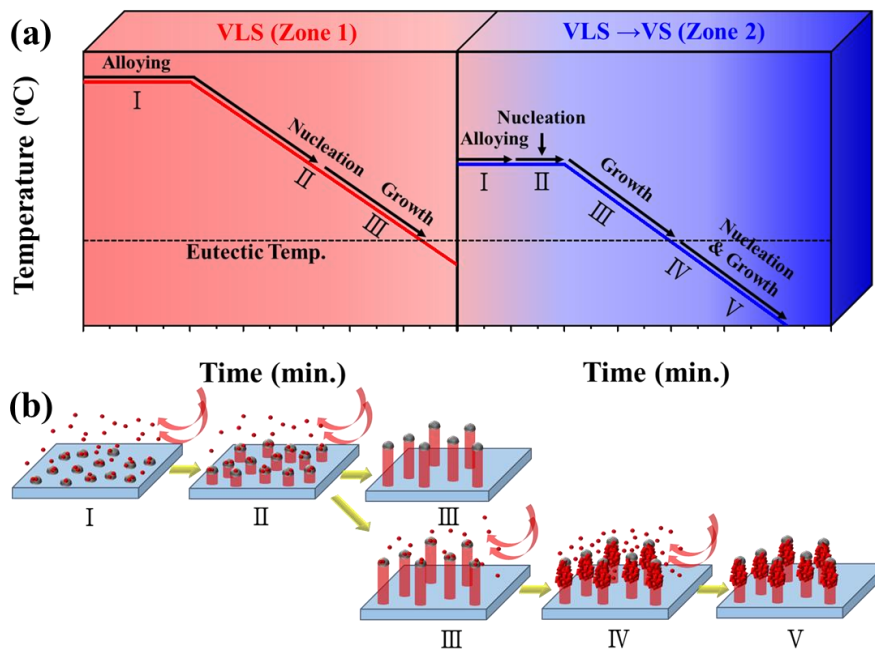


Figure 4.6 Growth mechanism of ZnS nanostructure.

4.4 Conclusion

In recent decades, much attention has been focused on the synthesis and development of nanomaterials, but the development of means for the complete characterization of such objects and structures took much less time. Unlike molecules and extended solid chemical structures, there are few periodic nanostructured 3D models available for 3D printing. We have shown that 3D characterization of ZnS nanostructure can be performed by electron tomography and show how electron tomography experiments can be used to determine the size of nanoparticles attached to the ZnS nanostructure I gave it. The methods and approaches described herein are becoming increasingly popular and provide access to the relationship between material properties and performance. Quantitative tomography makes it possible to perform both qualitative and quantitative properties of nanomaterials. It also applies well to accurate morphological studies such as faceting of nanocrystals. The close agreement between morphology and chemical composition is expected to have a significant impact in the future, as it provides powerful tools for analyzing materials at the forefront of catalysis, nanoelectronics, treatment and imaging. Recent advances in electron microscopy and the development of new methodologies enable the realization of 3D models through routine electron tomography experiments with atomic resolution in the near future, but further improvements are still needed.

4.5 References

- [1] S. Mitchell, N. L. Michels, K. Kunze, J. Pérez-Ramírez, *Nat Chem*, **4**, 825, (2012)
- [2] I. L.C. Buurmans, B. M. Weckhuysen, *Nat Chem*, **4**, 873, (2012).
- [3] V. Ortalan, A. Uzun, B. C. Gates, N. D. Browning, *Nat Nanotechnol*, **5**, 843, (2010)
- [4] L. P. Hansen, Q. M. Ramasse, C. Kisielowski, M. Brorson, E. Johnson, H. Topsøe, *Angew Chem Int Ed*, **50**, 10153, (2011)
- [5] X. Mou, B. Zhang, Y. Li, L. Yao, X. Wei, D. S. Su, *Angew Chem Int Ed*, **51**, 2989, (2012)
- [6] J. Fan, et al. *Angew. Chem. Int. Ed.* **42**, 3146, (2003)
- [7] J.R. Matos, et al. *J. Am. Chem. Soc.* **125**, 821, (2003)
- [8] D. Blavette, et al. *Nature* **363**, 432, (1993)
- [9] H. Friedrich, et al. *Chem. Rev.* **109**, 1613, (2009)
- [10] G.B. Moebus, et al. *Mater. Today* **10**, 18, (2007)
- [11] P.A. Midgley, et al. *Nat. Mater.* **8**, 271, (2009)
- [12] P. A Midgley, M. Weyland, *Ultramicroscopy*, **90**, 413, (2003)
- [13] J. Frank, *Electron Tomography: Three-Dimensional Imaging with the*

- Transmission Electron Microscope; Plenum Press: New York, London, 1992.
- [14] V. Lucic, F. Forster, W. Baumeister, *Annu. Rev. Biochem.*, **74**, 833, (2005)
- [15] M. Weyland, P.A. Midgley, *Institute of Physics Conference Series*, **161**, 239, (2001)
- [16] G. Mobus, B.J. Inkson, *Applied Physics Letters*, **79**, 1369, (2001)
- [17] G. Mo" bus, R.C. Doole, B.J. Inkson, *Ultramicroscopy*, **96**, 433, (2003)
- [18] P.A. Midgley, M. Weyland, *Ultramicroscopy*, **96**, 413, (2003)
- [19] R.D. Leapman, E. Kocsis, G. Zhang, T.L. Talbot, P. Laquerriere, *Ultramicroscopy*, **100**, 115, (2004)
- [20] V. Stolojan, R.E. Dunin-Borkowski, M. Weyland, P.A. Midgley, *Institute of Physics Conference Series*, **168**, 243, (2001)
- [21] H. Friedrich, M. McCartney, P. Buseck, *Microscopy and Microanalysis*, **9**, 174, (2003)
- [22] H. Friedrich, M.R. McCartney, P.R. Buseck, *Microscopy and Microanalysis*, **10**, 1174, (2004)
- [23] M. Weyland, J.M. Thomas, R.E. Dunin-Borkowski, P.A. Midgley, *Institute of Physics Conference Series*, **161**, 107, (2001)
- [24] P.A. Midgley, M. Weyland, J.M. Thomas, B.F.G. Johnson, *Chemical*

Communications, **10**, 907, (2001)

[25] H. Friedrich, M.R. McCartney, M. Weyland, P.R. Buseck, Proceedings of the European Microscopy Conference I, 234, (2004)

[26] U. Ziese, C. Kübel, A.J. Verkleij, A.J. Koster, Journal of Structural Biology, **138**, 58, (2002)

[27] N. Kawase, M. Kato, H. Nishioka, H. Jinnai, Ultramicroscopy, **107**, 8, (2007)

[28] H. Furukawa, M. Shimizu, Y. Suzuki, H. Nishioka, JEOL News, **36**, 12, (2001)

[29] A. Sakuma, Journal of the Physical Society of Japan, **63**, 3053, (1994)

[30] T. Klemmer, D. Hoydick, H. Okumura, B. Zhang, W.A. Soffa, Scripta Metallurgica et Materialia, **33**, 1793, (1995)

[31] J. Ariake, T. Chiba, S. Watanabe, N. Honda, K. Ouchi, Journal of Magnetism and Magnetic Materials, **287**, 229, (2005)

Chapter 5.

Fabrication and characterization of ZnS/ diamond-like carbon core-shell nanowires

5.1 Introduction

5.1.1 The structure and properties of diamond-like carbon

Carbon-based materials have been studied for very versatile element in the form of diamond and graphite. In recent years, many efforts toward advanced carbon materials based on the novel discovery have been devoted to realize nano-devices using carbon-based materials. Carbon possesses different allotropic forms owing to presence of three hybridization, sp^1 , sp^2 and sp^3 (Fig. 5.1).[1] That is, an amorphous carbon can have any mixture of sp^1 , sp^2 and sp^3 sites, with the possible presence of hydrogen and nitrogen. Diamond-like carbon (DLC) is known as an amorphous carbon with a high fraction of diamond-like (sp^3) bonding.[2] In contrast to diamond, In contrast to diamond, DLC can be fabricated at room temperature, which is an important practical advantage.

In general, DLCs can be classified with four types, as shown in figure

5.2.[3]

- (1) Hydrogenated amorphous carbon (a-C:H) films shows the highest H content, which can have up to 70% sp^3 . However,

this material is soft and has low density since most of sp^3 bonds are hydrogen terminated. Therefore, this materials is so called with polymer-like a-C:H (PLCH), which have a bandgap ranging from 2eV to 4eV. These films are usually deposited by plasma enhanced chemical vapor deposition (PECVD) at low bias voltage.[4]

- (2) a-C:H films with intermediate H content (20~40%) are called with diamond-like a-C:H (DLCH). They have a bandgap between 1 and 2eV and better mechanical properties due to having more sp^3 bonds than PLCH. Usually, they are deposited by PECVD or reactive sputtering.[5]
- (3) Hydrogenated tetrahedral amorphous carbon films (ta-C:H) are a kind of DLCH in which the sp^3 bonds can be increased during maintaining a fixed H content. Theses films are differently considered with DLCHs since they have the highest sp^3 (~70%) content, H content of 25~30%, and 2.4eV optical gap. These films are normally deposited by electron cyclotron wave resonance (ECWR) and plasma beam source (PBS).[6]
- (4) Graphite-like a-C:H (GLCH) with a high sp^2 content are having with low H content (less than 20 %). They are usually deposited by PECVD at high bias, dc glow discharge systems, or magnetron sputtering.[7]

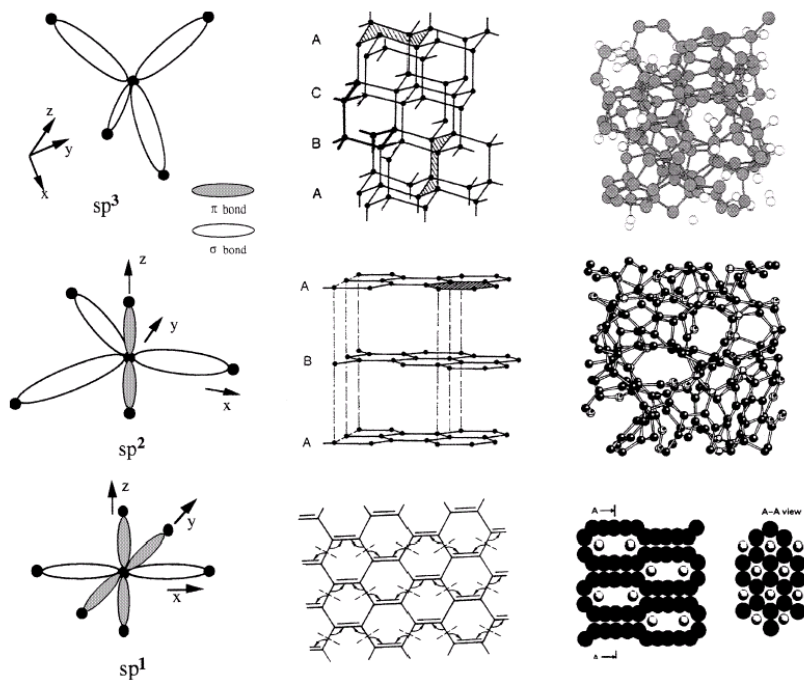


Figure 5.1 Exist in three hybridization of carbon with different allotropic forms as sp^1 , sp^2 and sp^3 .

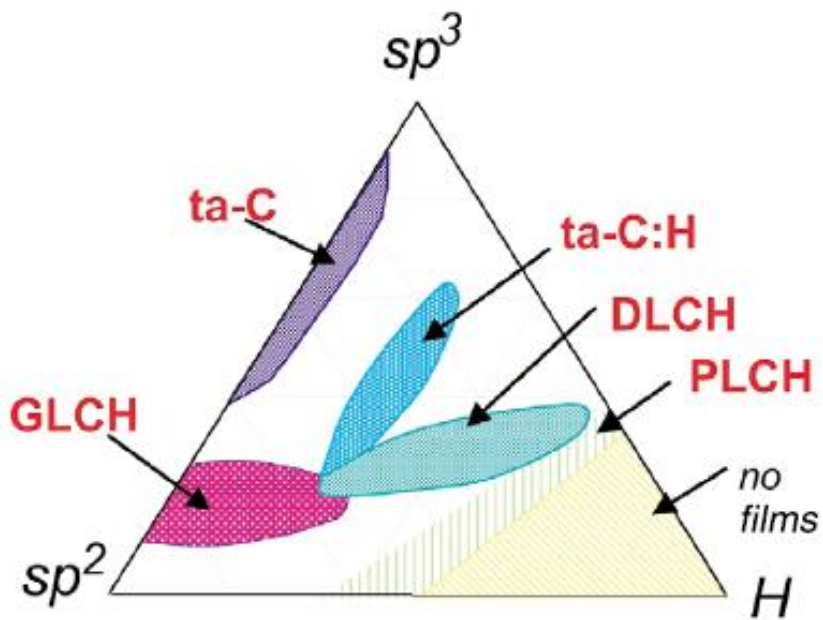


Figure 5.2 Ternary phase diagram of amorphous carbons. The three corners correspond to diamond, graphite, and hydrocarbons, respectively.

Major properties of DLC films are displayed in table 5.1 with diamond and graphite for comparison.[8] Diamond-like carbon film is an amorphous carbon film whereas diamond and graphite are bulk materials. Diamond possesses the highest Young's modulus (1100GPa) and hardness (~100GPa) of any materials due to its high molecular density. The hardness of various amorphous carbon films shows the value from 20 to 80GPa with containing of hydrogen (20-60 %) and sp^2 carbon (20-50 %) or without hydrogen and 80-88 % of sp^3 carbon bonds.[9]

DLCs exhibit an unique set of properties, which lead to a variety of applications (Table 5.2 and Figure 5.3) such as, for example, magnetic hard disk coatings; wear-protective and antireflective coatings for tribological tools, engine parts, and sunglasses; biomedical coatings; and micro-electriomechanical systems.[10]

Property	Diamond	DLC	Graphite
Density (g/cm ³)	3.51	1.8 – 3.6	2.26
Atomic Number Density (Mole/cm ³)	0.3	0.2 – 0.3	0.2
Hardness (Kgf/mm ²)	7000 - 10000	2000 - 8000	<500
Friction Coeff.	0.05	0.03 – 0.2	
Refractive Index	2.42	1.8 – 2.6	2.15 – 1.8
Transparency	UV-VIS-IR	VIS-IR	Opaque
Resistivity (Ωcm)	>10 ¹⁶	10 ¹⁰ - 10 ¹³	0.2 – 0.4

Table 5.1 Mechanical properties of DLC film evaluated with Diamond and Graphite for comparison.

Remark	Application
High Hardness	Tool coating for nonferrous material processing
Low friction coefficient	Coating for Surgical blade, Gear, Hard disk, Hip joint, VTR Head
Chemical inertness	Corrosion coating, Biocompatible coating
Excellent optical property	Coating of IR window for military weapon system

Table 5.2 Various general applications of diamond-like carbon film.



Figure 5.3 Various industrial applications of diamond-like carbon film such as coating for IR window of Tank, Infrared missile, VTR head drum, computer hard disk and stent.

5.1.2 Motivation

Since Wagner and Ellis first discovered Si whiskers in 1964, one-dimensional (1D) nanostructures such as nanowires, nanobelts and nanotubes have been under active development owing to their novel physical and chemical properties associated with their unique size and dimensionality [11-15]. The nanostructures have been mainly utilized as interconnections in a variety of nanoscale electronic/optical devices, single-electron transistors, light-emitting diodes, gas/chemical sensors, and photodetectors [16-20]. Among many semiconductor materials, ZnS is an important II-VI group semiconductor with fascinating excellent optical properties (direct bandgap energy = 3.68eV at 300K) and thus has been recently considered as the most promising material for phosphors in cathode-ray tubes and flat-panel displays, ultraviolet-light-emitting diodes, and injection lasers [21-24]. Extensive efforts have been made on the synthesis of 1D ZnS nanowires, nanotubes, nanobelts, and their complex assemblies [25-28].

The stability of nanowires is a key factor that corresponds to their practical applications used on multi-assembled nanoscale electro-devices [29]. In order to fully exploit ZnS nanowires as nanodevices, waveguides, etc., it is very important to passivate the surface of the ZnS nanowires, which have structures that exhibit high-chemical reactivity with respect to the deformation, oxidation, corrosion, and contamination of these structures. In this regard, several groups

have investigated the protection of ZnS nanowires with boron nitride (BN) or silicon dioxide (SiO₂) [30,31]. However, core-shell heterostructured ZnS nanowires used in various encapsulating nanomaterials are not yet understood in detail.

In this chapter, we aimed to introduce ZnS and diamond-like carbon (DLC) core-shell heterostructure nanowires to gain better insight into their applications towards nanoscale electro-devices. DLC is well-known as sp² and sp³ hybridized amorphous carbon materials and can be used in various applications due to the superior mechanical properties with a low friction coefficient, wear resistance, chemical inertness, and biocompatibility [32-34]. We fabricated ZnS/DLC core-shell heterostructure nanowires by a simple two-step process: the vapor-liquid-solid (VLS) method combined with radio frequency plasma enhanced chemical vapor deposition (rf PECVD). This fabrication is expected to open new possibilities for realizing of a lot of semiconductor nanostructures with DLC coating.

5.2 Experimental Procedure

5.2.1 Synthesis of ZnS/DLC core-shell nanowires

A core nanowire, a ZnS nanowire, was synthesized by a metal-organic chemical vapor deposition (MOCVD) process using a $(\text{Zn}(\text{S}_2\text{CNET}_2)_2)$ single molecular precursor in a horizontal furnace (Nextron, LABSYS CGF-5000) with a 30mm diameter quartz tube [35]. $(\text{Zn}(\text{S}_2\text{CNET}_2)_2)$ powder (Sigma Aldrich) was then placed upstream of a quartz tube and an Au sputtered thin film (thickness $\sim 30\text{nm}$) coated Si substrate was positioned downstream of the quartz tube that was initially evacuated till $\sim 5\text{mTorr}$. Subsequently, Ar flow in the quartz tube was set to 100sccm (SCCM denotes cubic centimeter per minute at standard temperature and pressure (STP)), which enabled the quartz tube to achieve a constant pressure of 300Torr . After the furnace was stabilized at the process pressure of 300Torr , the precursor was slowly pushed into the high temperature zone of the furnace and the growth of the ZnS nanowires proceeded for 10 minutes. After the processing of the synthesis, the furnace was cooled down to room temperature.

The as-synthesized ZnS nanowires were moved to the rf PECVD system with 13.56MHz . As for PECVD process, vacuum chamber was evacuated to 4×10^{-5} Torr for ultraclean and stable plasma generation. Methane (CH_4) with a flow of 10sccm was then put into the chamber, which was allowed to reach 3×10^{-2} Torr for the DLC deposition conditions. To facilitate the deposition of a thin DLC

coating on the ZnS nanowires, rf power was applied at 100W for 60 seconds. Different from the as-synthesized ZnS nanowires in gray, the ZnS/DLC core-shell nanowires were a light-yellow color.

5.2.2 Characterization method

The obtained ZnS/DLC core-shell nanowires were analyzed by X-ray diffraction (XRD, Bruker D8 Advance), scanning electron microscopy (SEM, FEI NOVA 200), transmission electron microscopy (TEM, JEOL-3000F), energy dispersive spectroscopy (EDS, Oxford INCA), Raman spectroscopy (LabRam HR), and Fourier transform infrared spectrometry (FT-IR, Bruker IFS-66/S).

5.3 Results and Discussion

5.3.1 Structural analysis of ZnS/DLC core-shell nanowires

Figure 5.4 shows a representative XRD pattern of ZnS/DLC core-shell nanowires. All the diffraction peaks were identified as a face-centered cubic (FCC) phase of ZnS (JCPDS:05-0566), while XRD peaks of DLC were hardly detected due to its amorphous structure.

A morphological study of the ZnS/DLC core-shell nanowires was performed using a SEM equipped with a dual beam focused ion beam system. Figure 5.5(a) displays a low-magnification SEM image of the ZnS/DLC core-shell nanowires. The length and width of the dense ZnS/DLC core-shell nanowires on a Si substrate were a range of $\sim 10\mu\text{m}$ and 50-150nm, respectively. The inset of Figure 5.5(a) shows a SEM image of the as-synthesized ZnS nanowires with a length and a width of $\sim 10\mu\text{m}$ and $\sim 30\text{-}120\text{nm}$, respectively. Figure 5.5(b) shows a high magnification SEM image of ZnS/DLC core-shell nanowires. Using the transmission mode of SEM, the outer layer of the DLC on the ZnS core nanowires can be clearly seen to have a thickness of $\sim 20\text{nm}$. The inset of Figure 5.5(b) shows an enlarged SEM image of the as-synthesized ZnS nanowires. As shown in the inset of Figure 5.5(b), an Au catalyst is clearly observed at the tip of an as-synthesized ZnS nanowire, indicating that the growth of ZnS nanowires was caused by the VLS method.

A detailed structural and chemical analysis of ZnS/DLC core-shell

nanowires was conducted by TEM. For the sample preparation of TEM analysis, ZnS/DLC nanowires were directly dispersed onto a SiO₂ thin film on a TEM grid. Figure 5.6(a) shows a low-magnification TEM image of a ZnS/DLC nanowire, which indicated that the ZnS/DLC nanowire is ~80nm in diameter with a flat interface between the ZnS and the DLC core-shell layer. A high resolution TEM (HRTEM) was employed for the detailed investigation of the structure of ZnS/DLC core-shell nanowires. Figure 5.6(b) presents a HRTEM image of the ZnS/DLC core-shell nanowires and shows a clear interface between the surface of the as-synthesized ZnS nanowire and the outer layer of DLC. As observed in the inner ZnS nanowire, it shows exactly the (111) lattice plane with a d-spacing of ~3.12Å, which exhibits the ZnS nanowire formed along the [111] growth direction. This was confirmed by fast Fourier transformation (FFT), as shown in the inset of Figure 5.6(b), clearly indicating the single-crystallinity of the ZnS oriented to the [1 $\bar{1}$ 0] zone axis. It is worth mentioning that the interface between the ZnS and the DLC layer is very flat and uniform without any pre-treatment performed on the ZnS nanowires. DLC is generally known to be a material that is difficult to deposit on any substrate since it has high residual stress induced by the high sp³ fraction [36]. Therefore, pre-treatments, for instance, ion bombardment on an arbitrary substrate have been applied to the DLC deposition to promote good adhesion between the film and the substrate.

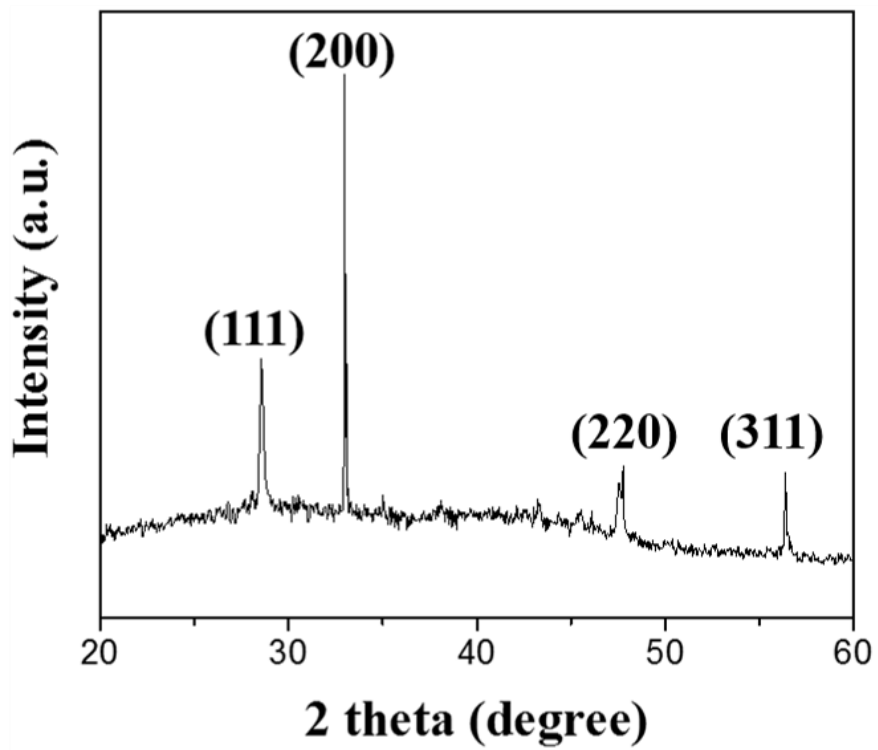


Figure 5.4 X-ray diffraction pattern of ZnS/DLC core-shell nanowires.

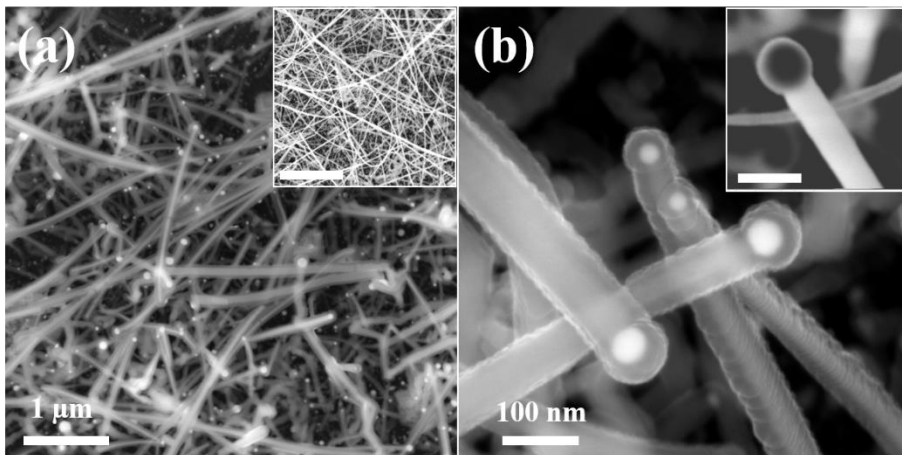


Figure 5.5 (a) Low-magnification SEM image of ZnS/DLC core-shell nanowires (inset: SEM image of as-synthesized ZnS nanowires. Scale bar is 1 μ m.). (b) High-magnification SEM image of ZnS/DLC core-shell nanowires (inset: enlarged SEM image of as-synthesized ZnS nanowires. Scale bar is 100nm.).

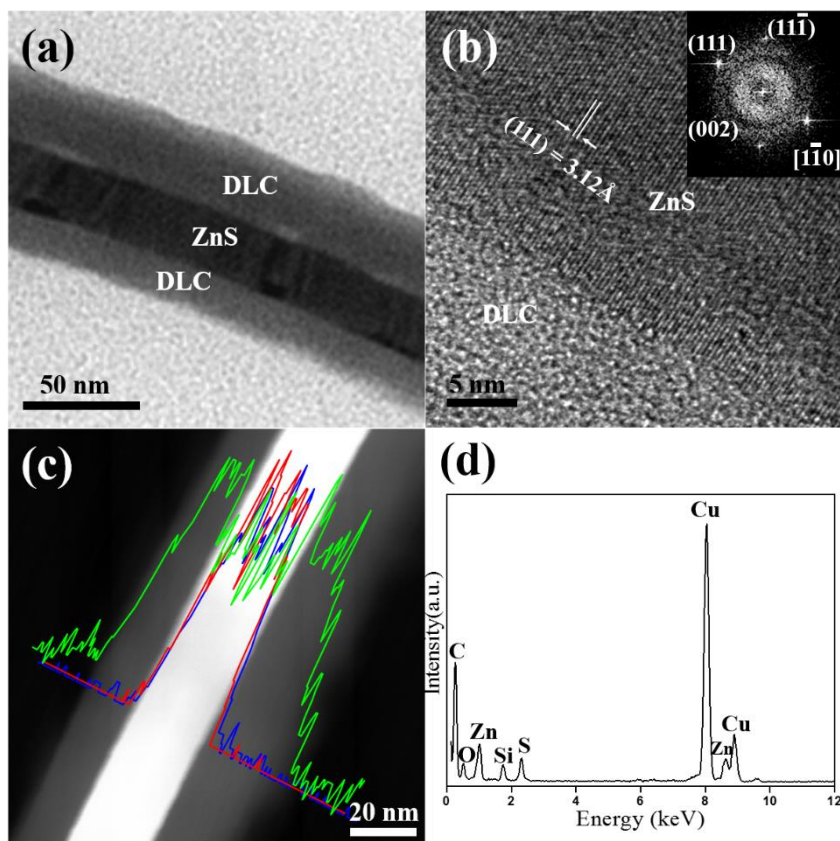


Figure 5.6 (a) The low-magnification TEM image of a ZnS/DLC nanowire. (b) HRTEM image of ZnS/DLC core-shell nanowires revealing growth along the $[111]$ direction (inset: corresponding FFT pattern obtained by $[11\bar{0}]$ zone axis). (c) ADF-STEM image of ZnS/DLC core-shell nanowires with corresponding EDS line-scan profile along the width direction (Red: Zn, Blue: S, Green: C). (d) EDS spectrum of (c).

5.3.2 Chemical analysis of ZnS/DLC core-shell nanowires

To further investigate the chemical information of the ZnS/DLC core-shell nanowire, we conducted a scanning TEM (STEM) annular dark field (ADF) analysis with an EDS line scan profile. Figure 5.6(c) presents an ADF image and the EDS line-profile analysis crossed with the growth direction laid on the ADF image of the ZnS/DLC core-shell nanowire. This evidently shows that only zinc (red) and sulfur (blue) were present within the ZnS nanowire, which has an intrinsic chemical composition without inter-diffusion at the interface between ZnS and DLC. Carbon (green), on the other hand, was uniformly distributed along the width direction of the core-shell nanowires. Figure 5.6(d) illustrates EDS spectrum obtained from the core-shell, which indicates that Cu, Si and O have originated from the TEM grid.

In order to gain further understanding of the DLC bonding state, Raman spectroscopy was employed. Figure 5.7(a) displays the Raman spectrum of the ZnS/DLC core-shell nanowires, which exhibits two kinds of Raman peaks that were observed at 1550 cm^{-1} (G peak) due to E_{2g} symmetry and vibration of sp^2 bonding in graphite carbon, and at 1330 cm^{-1} (D peak) regarding the breathing modes of sp^2 bonding in disordered graphitic carbon. Among many kinds of DLC materials, DLC deposited on ZnS nanowires are the most likely typical hydrogenated diamond-like amorphous carbon, which is in good agreement with the previous results of DLC deposited with PECVD [37].

To explore the optical properties of the ZnS/DLC core-shell nanowires, we investigated the infrared (IR) transmittance of the ZnS/DLC core-shell nanowires using FT-IR spectroscopy. The refractive index of ZnS is generally known as 2.3, resulting in a reflection of 15.5% which can be further reduced by using an optical interference film. DLC coated ZnS thin film in a micrometer-scale is therefore being used as a composite material for military equipment with enhanced IR transmittance and mechanical properties [38]. For the measurement of the IR transmittance, we directly dispersed nanowires onto a glass substrate and the measurements were made at least 20 times on each sample to ensure reliability. The FT-IR spectrum at a wavenumber range of 1900cm^{-1} to 3600cm^{-1} , as shown in Figure 5.7(b), reveals that the IR transmittance of the as-synthesized ZnS nanowires (red) and ZnS/DLC core-shell nanowires (black) were 92-99% in the given period. The enhanced IR transmittance of the ZnS/DLC nanowires is generally observed after 2100cm^{-1} wavenumber with values of 1.1-2.8% higher than those of the ZnS nanowires.

The fabrication process developed in this work is a very simple two-step process consisting of Au-catalyzed VLS growth and sequential rf PECVD and is able to synthesize ZnS/DLC. There is still a limitation to obtaining fully uniform core-shell hetero-structured nanowires due to the randomly oriented nature of the initial nanowires on the substrate. However, our fabrication technique may open up the superior stack coverage on 1D nanostructures using DLC as an outer layer deposited by common PECVD. Moreover, this new

process may be a more feasible and effective platform for multi-assembled nano-devices with elaborate deposition technology.

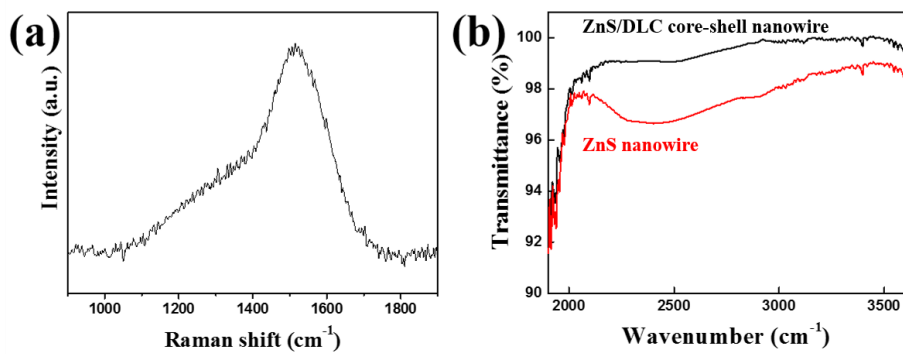


Figure 5.7 (a) Raman spectrum of ZnS/DLC core-shell nanowires. (b) FT-IR spectrum of as-synthesized ZnS nanowire (red) and ZnS/DLC (black) core-shell nanowire.

5.4 Conclusion

In summary, ZnS/diamond-like carbon core-shell heterostructure nanowires were successfully synthesized by VLS growth of ZnS nanowires and a sequential rf PECVD process. ZnS nanowires were initially synthesized with a width of 70-80nm and DLC layers were continuously deposited on the surface of ZnS nanowires with a thickness of 20-30nm. The detailed analysis of the carbon structure and optical properties of the DLC with Raman and FT-IR spectroscopy confirmed that two kinds of Raman bands observed at 1550 cm^{-1} (G peak) and at 1330 cm^{-1} (D peak) indicated DLC as hydrogenated diamond-like amorphous carbon. While the IR transmittance of ZnS and ZnS/DLC nanowires was in a range of 92-99%, the ZnS/DLC nanowires exhibited an enhanced IR transmittance property by 1.1-2.8% compared to the ZnS nanowire. The heterostructure core-shell nanowire developed in the present work can be applied to a wide range of nanoscale electro-devices, which not only introduces novel perspectives for applying DLC on a semiconductor surface and but also establishes a nanoscale fabrication technique for future nanodevices.

5.5 References

- [1] J. Robertson, Mater. Sci. Eng. R., **37**, 129, (2002)
- [2] C. Casiraghi, J. Robertson, A. C. Ferrari, Mater. Today, **10**, 44, (2007)
- [3] W. Jacob, W. Moller, Appl. Phys. Lett., **63**, 1771, (1993)
- [4] M. A. Tamor, W. C. Vassell, K. R. Carduner, Appl. Phys. Lett., **58**, 592, (1991)
- [5] S. F. Yoon, K. H. Tan, J. Ahn, J. Appl. Phys., **91**, 1634, (2002)
- [6] M. Weiler, S. Sattel, T. Giessen, K. Jung, H. Ehrhardt, V. S. Veerasamy, J. Robertson, Phy. Rev. B, **53**, 1594, (1996)
- [7] B. Popescu, A. Tagliaferro, F. D. Zan, E. A. Davis, J. Non-Cryst. Solids, **266**, 803, (2000)
- [8] K. -R. Lee, K. Y. Eun, Bull. Of the Korean Inst. Of Met. & Mater., **6**, 345, (1993)
- [9] J. Robertson, Prog. Solid St. Chem., **21**, 199, (1991)
- [10] J. P. Sullivan, T. A. Friedmann, MRS Bull., **26**, 309, (2001)
- [11] R. S. Wagner and W. C. Ellis, Applied Physics Letters, **4**, 89, (1964)
- [12] M. Law, J. Goldberger, and P. Yang, Annual Review of Materials Research, **34**, 83, (2004)

- [13] Z. L. Wang, *Advanced Materials*, **15**, 432, (2003)
- [14] Z.W. Pan, Z.R. Dai and Z.L. Wang, *Science*, **291**, 1947, (2001)
- [15] D. Moore and Z.L. Wang, *Journal of Materials Chemistry*, **16**, 3898, (2006)
- [16] Y. Li, F. Qian, J. Xiang, and C. M. Lieber, *Materials Today*, **9**, 18, (2006)
- [17] S. V. N. T. Kuchibhatla, A. S. Karakoti, D. Bera, and S. Seal, *Progress in Materials Science*, **52**, 699, (2007)
- [18] S. Barth, F. Hernandez-Ramirez, J. D. Holmes, and A. Romano-Rodriguez, *Progress in Materials Science*, **55**, 563, (2010)
- [19] Y. Xia, P. Yang, Y. Sun et al., *Advanced Materials*, **15**, 353, (2003)
- [20] C. M. Lieber and Z. L. Wang, *MRS Bulletin*, **32**, 99, (2007)
- [21] M. Bredol and J. Merikhi, *Journal of Materials Science*, **33**, 471, (1998)
- [22] Y. F. Zhu, D. H. Fan, and W. Z. Shen, *Journal of Physical Chemistry C*, **112**, 10402, (2008)
- [23] X. S. Fang, Y. Bando, M. Y. Liao, U. K. Gautam, C. Y. Zhi, B. Dierre, B. D. Liu, T. Y. Zhai, T. Sekiguchi, Y. Koide, and D. Golberg, *Advanced Materials*, **21**, 2034, (2009)
- [24] Y. Jiang, X. M. Meng, J. Liu, Z. R. Hong, C. S. Lee, and S. T. Lee, *Advanced Materials*, **15**, 1195, (2003)
- [25] Y. C. Zhu, Y. Bando, D. F. Xue, and D. Golberg, *Advanced Materials*, **16**, 831, (2004)
- [26] X. S. Fang, L. Wu and L. Hu, *Advanced Materials*, **23**, 585, (2011)
- [27] X. S. Fang, T. Y. Zhai, U. K. Gautam, L. Li, L. M. Wu, Y. Bando and D.

- Golberg, *Progress in Materials Science*, **56**, 175, (2011)
- [28] X.S. Fang, Y.S. Bando, C.H. Ye, G.Z. Shen and D. Golberg, *Journal of Physical Chemistry C*, **111**, 8469, (2007)
- [29] X. Duan, Y. Huang, Y. Cui, J.Wang, and C. M. Lieber, *Nature*, **409**, 66, (2001)
- [30] Y.-C. Zhu, Y. Bando, D.-F. Xue, F.-F. Xu, and D. Golberg, *Journal of the American Chemical Society*, **125**, 14226, (2003)
- [31] X. Fan, X. M. Meng, X. H. Zhang, S. T. Lee and S. K. Wu, *Applied Physics Letters*, **86**, Article ID 173111, (2005)
- [32] J. Robertson, *Materials Science and Engineering: R: Reports*, **37**, 129, (2002)
- [33] A. Grill, *Diamond and Related Materials*, **12**, 166, (2003)
- [34] A. H. Lettington, *Carbon*, **36**, 555, (1998)
- [35] Z. Q. Wang, X. D. Liu, J. F. Gong, H. B. Huang, S. L. Gu and S. G. Yang, *Crystal Growth and Design*, **8**, 3911-3913, (2008)
- [36] E. Liu, L. Li, B. Blanpain, and J. P. Celis, *Journal of Applied Physics*, **98**, Article ID 073515, (2005)
- [37] K.J. Clay, S.P. Speakman, N.A. Morrison, N. Tomozeiu, W.I. Milne and A. Kapoor, *Diamond and Related Materials*, **7**, 1100, (1998)
- [38] G.F. Zhang, L.J. Guo, Z. T. Liu, X. K. Xiu and X. Zang, *Journal of Applied Physics*, **76**, 705, (1994)

Chapter 6.

Influence of the contact interface on the electrical characteristics of a ZnO microwire with silver paste electrodes

6.1 Introduction

Zinc oxide (ZnO), a direct semiconductor with a wide band gap of 3.3 eV, has recently been considered as a promising material for device applications in electronics, optoelectronics, and the emerging field called nanopiezotronics [1-4]. In particular, single ZnO microwires (MWs) have attracted significant attention as a means of understanding electromechanically coupling behavior [5-9], exciton-polariton behavior [10,11], and electrical properties in heterojunctions [12-16] due to the potential applications of their quasi-one-dimensional (1D) structures.

Previous studies have demonstrated that the contact properties between a quasi-1D ZnO structure and the source/drain (S/D) electrodes play a significant role in the performance of devices, including electronic transport characteristics [17-20]. For example, high performance ultraviolet (UV) photodetection can be realized by utilizing Schottky contacts [19-22]. In addition, ZnO MWs have recently been used as an excellent model system to understand the transport mechanism and simultaneously investigate the strain-induced piezoelectric

properties for future applications due to their undergoing deformation from tensile or compressive strain [7,8,23-26]. Until now, metal contacts to ZnO MWs have been formed in previous studies by simply depositing silver (Ag) paste because it is difficult to fabricate patterns of thick metal electrodes on them using either a lithography process or a shadow mask. Importantly, understanding the interfaces formed between an Ag paste electrode and a quasi-1D ZnO MW is critical for controlling the electronic behaviors associated with contact resistance, which plays an important role in device performance. However, to the best of our knowledge, there has been no work showing direct evidence of how the contact interface between the ZnO MW and Ag paste electrodes affects the electrical transport properties in the ZnO MW devices.

Here, we demonstrate the influence of the contact interface on the electrical characteristics of ZnO MW devices with Ag paste electrodes through the formation of Ohmic-Ohmic and Schottky-Schottky contacts. To this end, we introduced different methods for the curing of the Ag paste: a slow curing method by increasing the temperature after depositing the Ag paste on the ZnO MW surface and a rapid curing method by dropping Ag paste on the ZnO MW upon heating at an elevated temperature. The slow curing case (type A device) exhibits linear current-voltage characteristics, whereas the rapid curing case (type B device) shows a non-linear electrical behavior. This is likely due to the effect of the contact interface properties between the ZnO MW and Ag paste electrodes, such as interfacial defects and/or charge trap sites, which is

supported by the results of electron microscopy and cathodoluminescence, including electrical analysis associated with trap sites. Energy band diagrams are suggested to explain the charge transport mechanism for different types of Ag contacts to the ZnO MW. Our results show the possibility of tunable electrical properties through the contact properties between quasi-1D microstructures and Ag paste electrodes.

6.2 Experimental procedure

6.2.1 Synthesis of ZnO MW and the formation process of ZnO MW devices

The ultralong ZnO MWs used in this study were grown using a vapor-phase transport process, as described elsewhere [27]. The as-grown ZnO MWs had a typical diameter of several micrometers and a length of several hundred micrometers to several millimeters. To investigate the electrical properties of the ZnO MWs with different contacts of Ag paste, we selected the most geometrically similar microwires with diameters of 10-12 μm using an optical microscope. The straight ZnO microwire was first transferred onto a p-type Si (100) substrate with a 100 nm thermally grown oxide (SiO_2). Then, the conductive two-phase Ag paste was used to tightly fix both ends of the ZnO MW on the substrate for the formation of a metal-semiconductor-metal structure device in which the Ag paste was used as the source (S) and drain (D) electrodes.

In Fig. 6.1, the fabrication processes of ZnO MW devices with different types of Ag paste contacts are illustrated. The conductive Ag paste was first dropped on both ends of the ZnO MW on the oxidized p-type Si substrate, and then it was slowly heated on a hot plate up to 150 °C for curing into Ag paste electrodes (denoted as type A, Fig. 1a). In another trial, the ZnO MW was laid down on

the substrate and was then heated on a hot plate at 150 °C, followed by the deposition of Ag paste at both ends (denoted as type B, Fig. 6.1b).

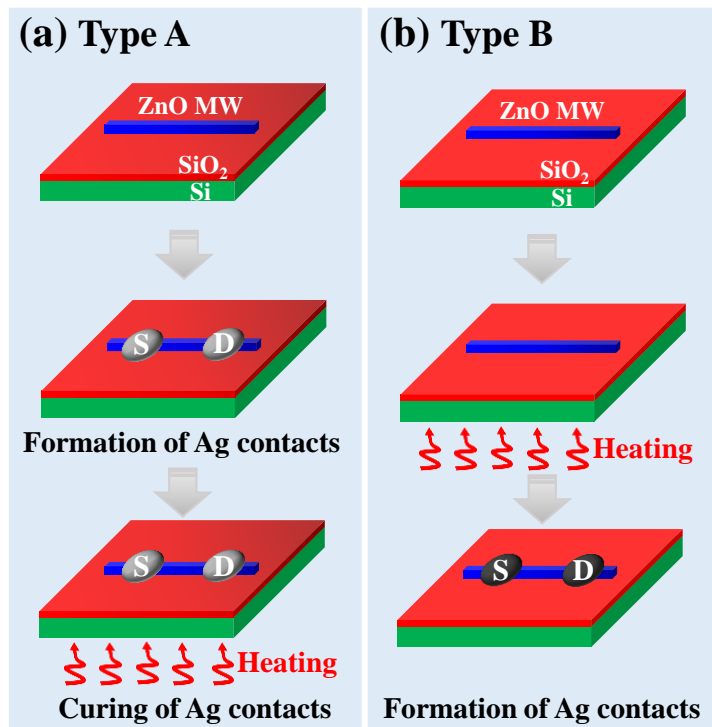


Figure 6.1 Schematic illustrations depicting the formation process of ZnO MW devices with two different types of Ag paste contacts.

6.2.2 Characterization method

The electrical properties of the ZnO MW with Ag paste electrodes were characterized using a semiconductor characterization system (Keithley 4200-SCS) at room temperature. The morphology and elemental composition of the ZnO MW was characterized by field-emission scanning electron microscopy (FE-SEM, Hitachi-4800) and energy-dispersive X-ray spectroscopy (EDS, EDAX, Inc. attached to the SEM) operated at 5 kV. In addition, we investigated the interfacial properties of the ZnO MW/Ag paste contacts through structural and optical characterization using transmission electron microscopy (TEM, JEOL-3000F), focused ion beam (FIB, FEI NOVA200), and cathodoluminescence (CL) spectroscopy (Gatan MonoCL4).

6.3 Results and Discussion

6.3.1 I-V characteristics of ZnO MW devices

Figs. 6.2a and b show the linear-scale plots of the current (I)-voltage (V) characteristics obtained from the type A and type B devices, respectively. Interestingly, two distinct differences in their I-V curves are observed even for the same contact metals. The type A device displays nearly linear I-V behavior, which is indicative of Ohmic-Ohmic contacts for both forward and reverse biases (Fig. 6.2a). In contrast, the type B device shows a nearly symmetrical nonlinear I-V characteristic, which is indicative of Schottky-Schottky contacts for both forward and reverse biases (Fig. 6.2b). In particular, the type A device is more conductive than the type B device in the low-voltage region. This suggests that contact properties such as the Schottky barrier at the interface between the ZnO MW and Ag paste electrodes are responsible for the change in the electrical conductivity. In addition to the overall decrease in conductivity, the type B device shows qualitatively different I-V characteristics. Figs. 6.2c and d show log-log plots of the I-V characteristics of the type A and type B devices, respectively. Here, we find that compared to the type A device, the current and voltage of the type B device follow a power-law relationship $I \sim V^n$, with $n > 2$, especially under the application of high forward and reverse voltages, which is characteristic of a space-charge-limited current in the presence of exponentially distributed charge traps [28-30]. Therefore, we speculate that the

distinct electronic behavior of the type B device is due to the defective interface between the ZnO MW and Ag paste electrodes.

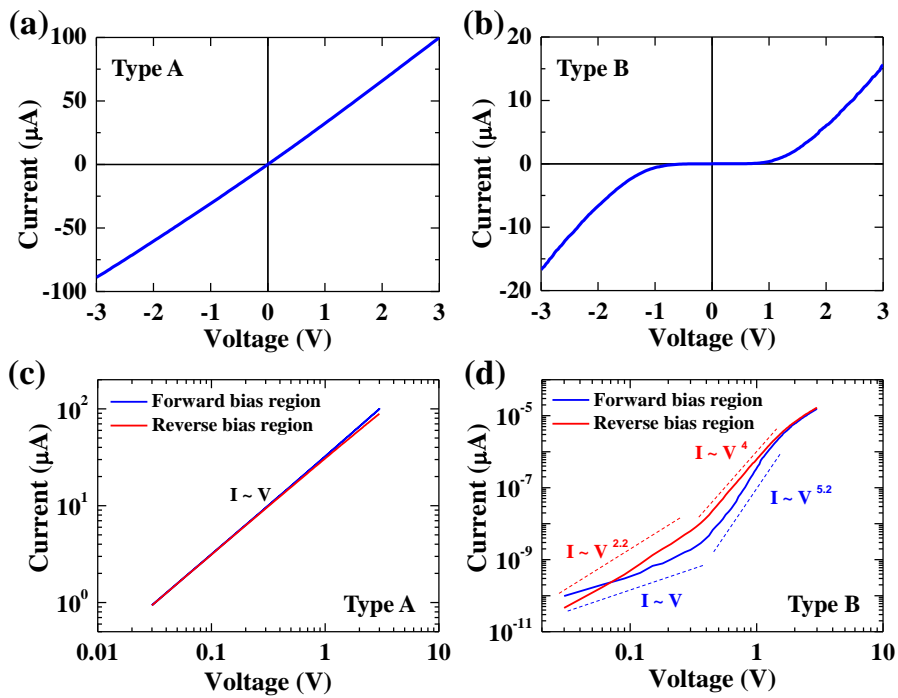


Figure 6.2 Current (I)-voltage (V) characteristics of (a) type A and (b) type B devices. Log-log plots of I-V characteristics of (c) type A and (d) type B devices.

6.3.2 Structural Analysis of ZnO MW devices

To understand these two distinct differences in the electrical transport of these two types of device, we examined the morphological and structural properties at the contact interface between the ZnO MW and Ag paste electrodes using SEM, TEM, and CL spectroscopy. Figs. 6.3a and b show SEM images of the Ag paste electrode formed at the end of the ZnO MW for the type A and type B devices, respectively. Compared to the Ag paste electrode of the type A device, that of the type B device has a relatively rougher and more porous morphology, which can be due to the fast drying induced by dropping the Ag paste solution on the ZnO MW surface under heating at 150 °C. Note that the Ag paste consists of micron-scale Ag flakes and a solvent such as cyclohexanol, butanol, terpineol, isoamyl alcohol or an ethylene glycol ether mixture of cyclohexanol–methanol [31,32].

Fig. 6.4 shows cross-sectional SEM images of ZnO MWs taken from the type A and type B devices with corresponding EDS data. To clearly investigate the interface of the ZnO MW/Ag paste contact, SEM samples were prepared by cross-sectioning using an ion milling system. For the type A device, the Ag flakes with a conductive polymer are closely packed all around the ZnO MW surface (Fig. 6.4a), whereas for the type B device, large areas of voids without Ag flakes are observed, and only a few Ag flakes contact the ZnO MW surface. To determine the chemical information of the ZnO MWs, Figs. 4b and d show

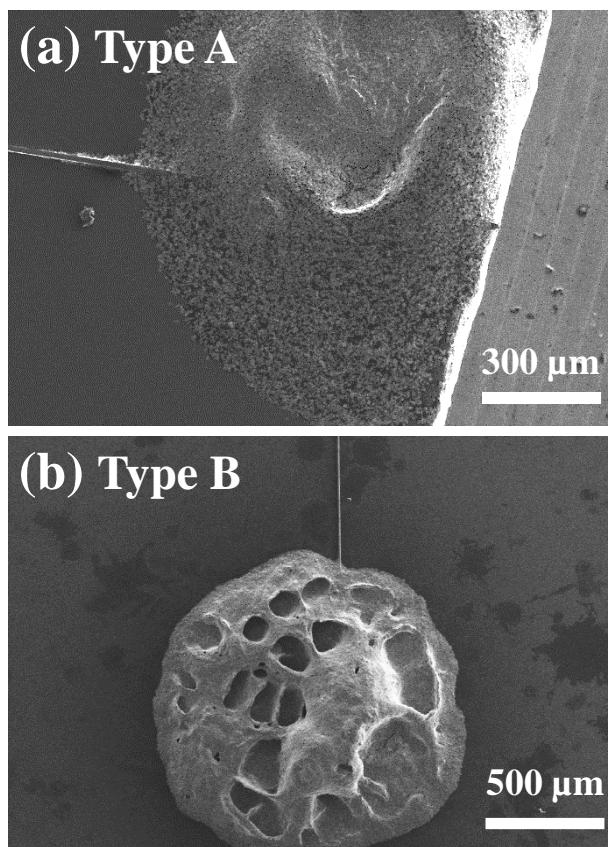


Figure 6.3 SEM images of the Ag paste electrode formed at the end of the ZnO MW for (a) type A and (b) type B devices.

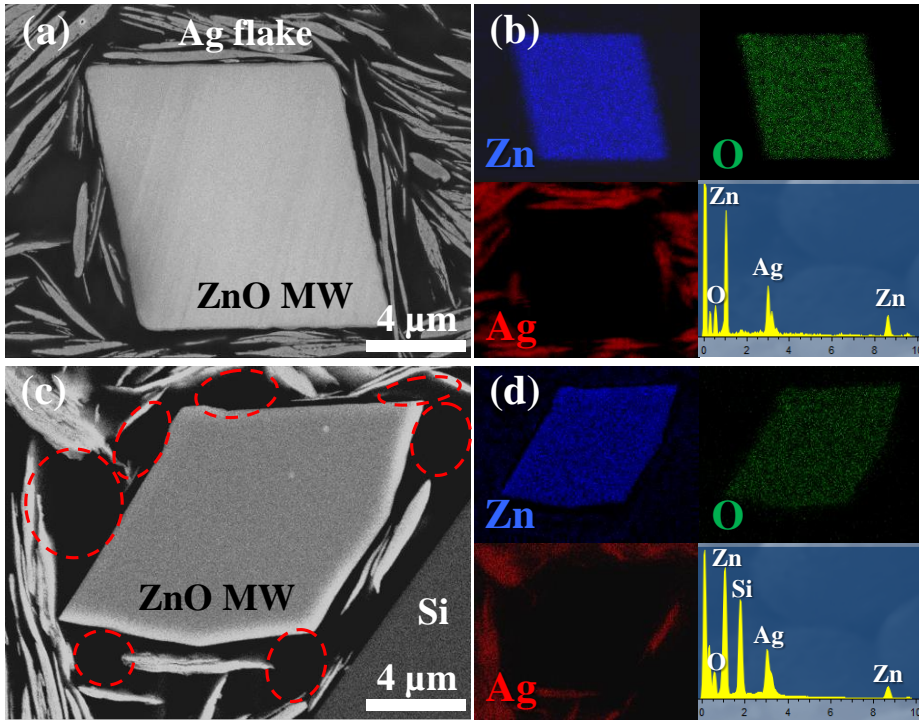


Figure 6.4 Cross-sectional SEM images of ZnO MWs taken from (a) type A and (c) type B devices with corresponding EDS mapping data (b) of (a) and (d) of (c).

the EDS mappings and spectra obtained from the ZnO MWs shown in Figs. 6.4a and c, respectively. From the EDS results, we confirm that the samples had a clear interface between the ZnO MW and Ag electrode without any interdiffusion. We believe that this distinct interfacial property can strongly affect the electronic transport behavior of the Ag paste-contacted ZnO MW. The rough and porous microstructures can increase the Schottky barrier at the contact interface between the Ag paste electrode and ZnO MW, whereas dense and interlocked microstructures can reduce the Schottky barrier at the contact interface. In addition, we performed a cross-sectional TEM analysis on ZnO MWs of type A and type B devices for a detailed investigation of the possible presence of structural defects at the interface between the ZnO MW and Ag paste electrode. TEM specimens were prepared by the FIB lift-out technique at the interface between the ZnO MW and Ag paste electrode of cross-sectional SEM specimens of the type A and type B devices. Figs. 6.5a and b show cross-sectional bright-field TEM images of ZnO MWs for the type A and type B devices, respectively. As shown in Fig. 6.5a, the type A device shows a flat interface between the ZnO MW and Ag paste. Meanwhile, the type B device in Fig. 5b exhibits a relatively rougher interface between the ZnO MW and Ag paste. Hence, defects were clearly found along the cross-sectional depth direction from the ZnO MW surface. To obtain detailed microstructure information on the presence of defects, we conducted dark-field TEM analysis, as shown in Fig. 6.5c and d. Considering the dislocation of the ZnO MW for

the type A and type B devices, we chose the $g = [012]$ condition, which enables basal, prismatic and pyramidal dislocations to be visualized on the single crystalline ZnO MW. As shown in Fig. 6.5c, in the case of the type A device, the ZnO MW is still a single crystalline structure without any dislocation along the cross-section direction. On the contrary, in the case of the type B device, we observed a dislocation cloud at a depth of ~ 300 nm from the ZnO MW surface, as shown in Fig. 6.5d. We believe that the dislocation cloud might be generated from the rapid curing process induced when the Ag paste drops on the ZnO MW that had been heated to an elevated temperature. In other words, the dislocation clouds from the ZnO surface are generated due to the steep temperature gradient between the ZnO MW and Ag paste, which causes thermal stress-driven defects without any external mechanical stress [33,34]. Furthermore, we examined the localized energy levels near the dislocations using scanning electron microscope (SEM)-based CL. Fig. 6.6 shows the CL spectra for cross-sectional ZnO MWs of the type A (Fig. 6.6a) and type B (Fig. 6.6b) at room temperature. The ZnO MW in the type A device exhibits only strong UV emission at approximately 380 nm and almost negligible defect emission bands, whereas for that of the type B device, a weak blue emission band at 460 nm is interestingly observed, including a strong UV emission and a negligible defect emission band. Although the observation of blue band emissions has also been reported from ZnO films [35] and ZnO nanostructures [36-38], the origin of this emission is not yet clear. This emission might

correspond to the formation of defect centers in ZnO, which can be associated with the existence of oxygen-depleted interface traps [39,40] or interstitial zinc defects [38].

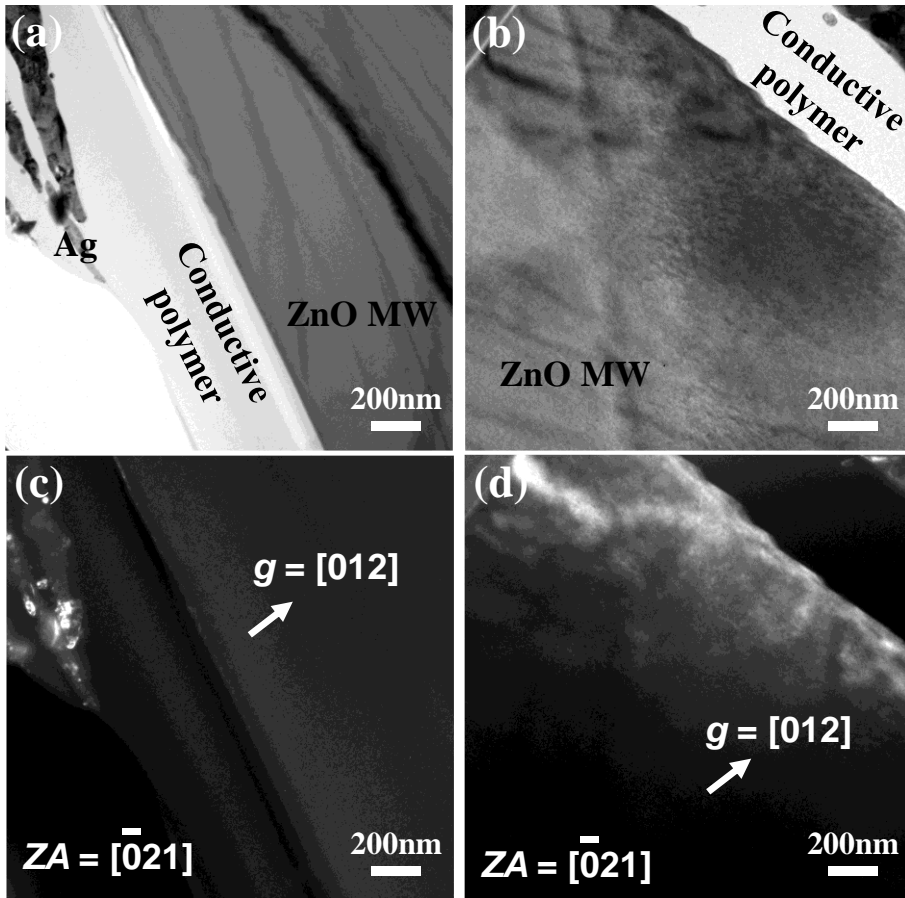


Figure 6.5 Cross-sectional bright field TEM images of (a) type A and (b) type B devices corresponding to dark field TEM images (c) of (a) and (d) of (b).

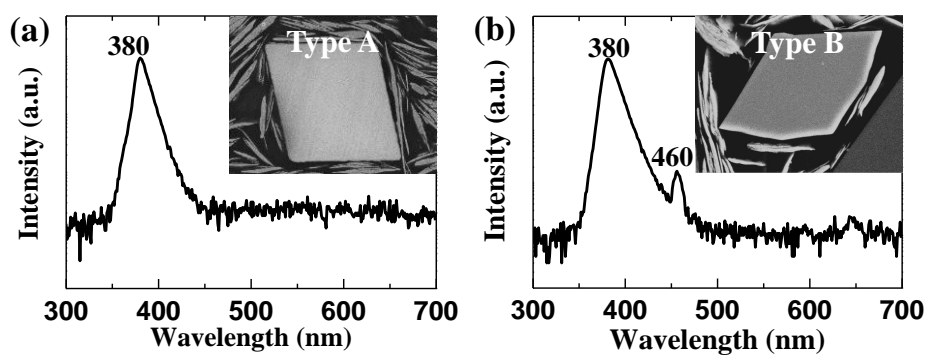


Figure 6.6 Cathodoluminescence spectra for (a) type A and (b) type B devices.

6.3.3 Energy band diagrams

Based on the SEM, TEM, and CL characterizations, the different I-V characteristics for the type A and type B devices can be explained by the energy band diagrams in Fig. 6.7. Fig. 6.7 shows schematic illustrations and corresponding energy band diagrams depicting the two different types of electrical contacts between the ZnO MW and Ag paste electrodes. In the case of the type A device (Fig. 6.7a), the source/drain contacts can form very low Schottky barrier heights (Φ_{B0}) due to the close packing of the Ag paste at the Ag/ZnO interfaces, which result in good Ohmic contacts and improved current injection from the electrodes. In contrast, for the type B device (Fig. 6.7b), much larger Schottky barrier heights (Φ_{B1}) at the source/drain contacts can be formed due to the presence of large areas of voids without Ag flakes and/or defect-induced interface traps at the Ag/ZnO interfaces, which can act as charge trap sites. This results in Schottky contacts and limited current injection from the electrodes.

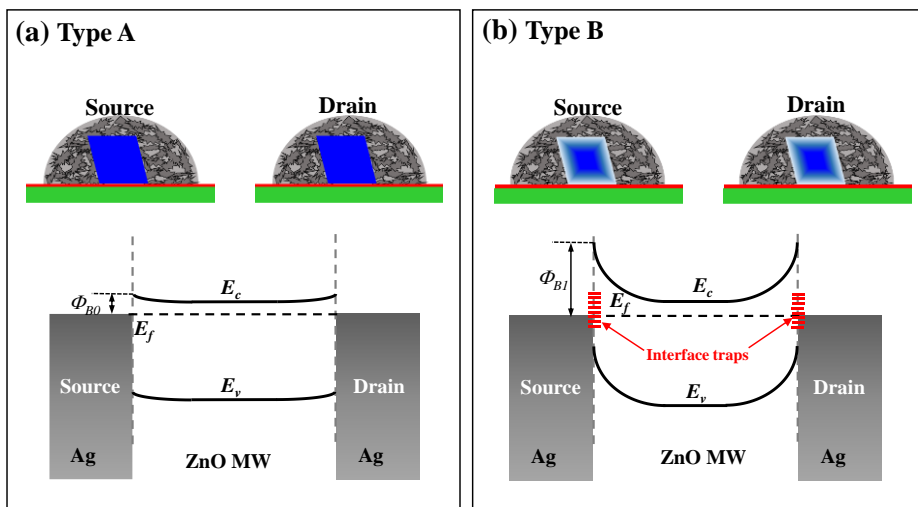


Figure 6.7 Schematic illustrations and corresponding energy band diagrams depicting two different types of electrical contacts between Ag paste electrodes and the ZnO MW.

6.4 Conclusions

In summary, the influence of the contact interface on the electrical characteristics of a ZnO MW with Ag paste electrodes has been demonstrated through the formation of Ohmic-Ohmic and Schottky-Schottky contacts at the ZnO MW/Ag paste interfaces. In the case of a slow curing with increasing temperature after depositing Ag paste on the ZnO MW surface, the device exhibits linear current-voltage characteristics, indicating Ohmic contacts, whereas following the deposition and simultaneous rapid curing of the Ag paste upon deposition on a high-temperature preheated ZnO MW, the device shows a non-linear behavior, indicating Schottky contacts. This is likely due to the effect of the contact interface properties, such as interfacial defects and/or the presence of large areas of voids without Ag flakes as charge trap sites at the ZnO MW/Ag paste interfaces, which is supported by the electron microscopy and cathodoluminescence results. The charge transport mechanism for different types of Ag paste contacts to a ZnO MW was explained by energy band diagrams at the contact interface.

6.5 References

- [1] A. Urbieto, R. del Campo, R. Pérez, P. Fernández, J. Piqueras, Luminescence and waveguiding behavior in Tb doped ZnO micro and nanostructures, *J. Alloys Comp.* 610 (2014) 416-421.
- [2] K. Kim, D-H. Lee, S.Y. Lee, G-E. Jang, J-S. Kim, Effect of Ag/Al co-doping method on optically p-type ZnO nanowires synthesized by hot-walled pulsed laser deposition, *Nanoscale Res. Lett.* 7 (2012) 273.
- [3] J.M. Calleja, M. Cardona, Resonant Raman scattering in ZnO, *Phys. Rev. B* 16 (1977) 3753.
- [4] Z.Q. Chen, A. Kawasuso, Y. Xu, H. Naramoto, X.L. Yuan, T. Sekiguchi, R. Suzuki, T. Ohdaira, Production and recovery of defects in phosphorus-implanted ZnO, *J. Appl. Phys.* 97 (2005) 013528.
- [5] H. Li, X. Zhang, N. Liu, L. Ding, J. Tao, S. Wang, J. Su, L. Li, Y. Gao, Enhanced photo-response properties of a single ZnO microwire photodetector by coupling effect between localized Schottky barriers and piezoelectric potential, *Opt. Express* 23 (2015) 21204-21212.
- [6] Z.-M. Liao, H.-C. Wu, Q. Fu, X. Fu, X. Zhu, J. Xu, I.V. Shvets, Z. Zhang, W. Guo, Y. Leprince-Wang, Q. Zhao, X. Wu, D.-P. Yu, Strain induced exciton fine-structure splitting and shift in bent ZnO microwires, *Sci. Rep.* 2 (2012) 452.

- [7] C.-L. Wang, S.-J. Tsai, J.-W. Chen, H.-W. Shiu, L.-Y. Chang, K.-H. Lin, H.-C. Hsu, Y.-C. Chen, C.-H. Chen, C.-L. Wu, Imaging and characterization of piezoelectric potential in a single bent ZnO microwire. *Appl. Phys. Lett.* 105 (2012) 123115.
- [8] Y.F. Hu, Y.L. Chang, P. Fei, R.L. Snyder, Z.L. Wang, Designing the Electric Transport Characteristics of ZnO Micro/Nanowire Devices by Coupling Piezoelectric and Photoexcitation Effects, *ACS Nano* 4 (2010) 1234-1240.
- [9] X. Fu, C. Su, Q. Fu, X. Zhu, R. Zhu, C. Liu, Z. Liao, J. Xu, W. Guo, J. Feng, J. Li, D. Yu, Tailoring Exciton Dynamics by Elastic Strain-Gradient in Semiconductors, *Adv. Mater.* 26 (2014) 2572-2579.
- [10] D. Xu, W. Xie, W. Liu, J. Wang, L. Zhang, Y. Wang, S. Zhang, L. Sun, X. Shen, Z. Chen, Polariton lasing in a ZnO microwire above 450K, *Appl. Phys. Lett.* 104 (2014) 082101.
- [11] K. Qiu, Y. Zhao, Y. Gao, X. Liu, S. Cao, J. Tang, Y. Zhang, B. Feng, X. Xu, Refractive index of a single ZnO microwire at high temperatures, *Appl. Phys. Lett.* 104 (2014) 081109.
- [12] L.L. Shi, F. Wang, B.H. Li, X. Chen, B. Yao, D. X. Zhao, D.Z. Shen, A highly efficient UV photodetector based on a ZnO microwire p-n homojunction, *J. Mater. Chem. C* 2 (2014) 5005-5010.
- [13] Q. Yang, W. Wang, S. Xu, Z.L. Wang, Enhancing Light Emission of ZnO

Microwire-Based Diodes by Piezo-Phototronic Effect, *Nano Lett.* 11 (2011) 4012-4017.

[14] J. Qi, X. Hu, Z. Wang, X. Li, W. Liu, Y. Zhang, A self-powered ultraviolet detector based on a single ZnO microwire/p-Si film with double heterojunctions, *Nanoscale* 6 (2014) 6025-6029.

[15] T.I. Lee, W.J. Choi, J.P. Kar, Y.H. Kang, J.H. Jeon, J.H. Park, Y.S. Kim, H.K. Baik, J.M. Myoung, Electrical Contact Tunable Direct Printing Route for a ZnO Nanowire Schottky Diode, *Nano Lett.* 10 (2010) 3517-3523.

[16] C.S. Lao, J. Liu, P. Gao, L. Zhang, D. Davidovic, R. Tummala, Z.L. Wang, ZnO Nanobelt/Nanowire Schottky Diodes Formed by Dielectrophoresis Alignment across Au Electrodes, *Nano Lett.* 6 (2006) 263-266.

[17] Y. Qiu, H.Q. Zhang, L.Z. Hu, L.N. Wang, B. Wang, D.C. Yang, G.Q. Liu, J.Y. Ji, X. Liu, J.F. Lin, Y. Lang, F. Li, S.J. Han, Improving the quality of Schottky contacts on ZnO microwires using Cu-contained silver paste electrode, *Micro Nano Lett.* 7 (2012) 592-595.

[18] H. Kim, H. Yun, H.A. Yoon, S.W. Lee, Integrating ZnO Microwires with Nanoscale Electrodes Using a Suspended PMMA Ribbon for Studying Reliable Electrical and Electromechanical Properties, *Adv. Energy Mater.* 4 (2014) 1301973.

[19] J. Zhou, Y.D. Gu, Y.F. Hu, W.J. Mai, P.H. Yeh, G. Bao, A.K. Sood, D.L.

Polla, Z.L. Wang, Gigantic enhancement in response and reset time of ZnO UV nanosensor by utilizing Schottky contact and surface functionalization, *Appl. Phys. Lett.* 94 (2009) 191103.

[20] Y. Hu, J. Zhou, P.H. Yeh, Z. Li, T.Y. Wei, Z.L. Wang, Supersensitive, fast-response nanowire sensors by using Schottky contacts, *Adv. Mater.* 22 (2010) 3327-3332.

[21] D. Zhang, Y. Sheng, J. Wang, F. Gao, S. Yan, J. Wang, L. Pan, Q. Wan, Y. Shi, ZnO nanowire photodetectors based on Schottky contact with surface passivation, *Opt. Commun.* 2015, in press.

[22] J. Song, Y. Zhang, C. Xu, W. Wu, Z.L. Wang, Polar Charges Induced Electric Hysteresis of ZnO Nano/Microwire for Fast Data Storage, *Nano Lett.* 11 (2011) 2829-2834.

[23] R.S. Yang, Y. Qin, L.M. Dai, Z.L. Wang, Power generation with laterally packaged piezoelectric fine wires, *Nat. Nanotechnol.* 4 (2009) 34-39.

[24] J. Zhou, P. Fei, Y.D. Gu, W.J. Mai, Y.F. Gao, R.S. Yang, G. Bao, Z.L. Wang, Piezoelectric-Potential-Controlled Polarity-Reversible Schottky Diodes and Switches of ZnO Wires, *Nano Lett.* 8 (2008) 3973-3977.

[25] J.M. Wu, C.Y. Chen, Y. Zhang, K.H. Chen, Y. Yang, Y.F. Hu, J.H. He, Z.L. Wang, Ultrahigh Sensitive Piezotronic Strain Sensors Based on a ZnSnO₃ Nanowire/Microwire, *ACS Nano* 6 (2012) 4369-4374.

- [26] K. Jenkins, V. Nguyen, R. Zhu, R. Yang, Piezotronic Effect: An Emerging Mechanism for Sensing Applications, *Sensors* 15 (2015) 22914-22940.
- [27] J.I. Sohn, W.K. Hong, S.H. Lee, S.H. Lee, J.Y. Ku, Y.J. Park, J. Hong, S.W. Hwang, K.H. Park, J.H. Warner, S.N. Cha, J.M. Kim, Surface energy-mediated construction of anisotropic semiconductor wires with selective crystallographic polarity, *Sci. Rep.* 4 (2014) 5680.
- [28] W. Xu, A. Chin, L. Ye, C.Z. Ning, H. Yu, Charge transport and trap characterization in individual GaSb nanowires, *J. Appl. Phys.* 111 (2012) 104515.
- [29] Z.-M. Liao, Z.-K. Lv, Y.-B. Zhou, J. Xu, J.-M. Zhang, D.-P. Yu, The effect of adsorbates on the space-charge-limited current in single ZnO nanowires, *Nanotechnology* 19 (2008) 335204.
- [30] Y. Gu, L.J. Lauhon, Space-charge-limited current in nanowires depleted by oxygen adsorption, *Appl. Phys. Lett.* 89 (2006) 143102.
- [31] K.S. Siow, Mechanical properties of nano-silver joints as die attach materials, *J. Alloys Compd.* 514 (2012) 6–19.
- [32] S. Sakamoto, S. Nagao, K. Suganuma, Thermal fatigue of Ag flake sintering die-attachment for Si/SiC power devices, *J. Mater. Sci.: Mater*

Electron 24 (2013) 2593–2601.

[33] B. Debnath, G. Halder, S. Bhattacharyya, One-Step Synthesis, Structural and Optical Characterization of Self-Assembled ZnO Nanoparticle Clusters with Quench-Induced Defects, *Sci. Adv. Mater.* 6 (2014) 1160–1169.

[34] H. Zeng, G. Duan, Y. Li, S. Yang, X. Xu, W. Cai, Blue Luminescence of ZnO Nanoparticles Based on Non-Equilibrium Processes: Defect Origins and Emission Controls, *Adv. Funct. Mater.* 20 (2010) 561-572.

[35] Z. Fu, B. Lin, G. Liao, Z. Wu, The effect of Zn buffer layer on growth and luminescence of ZnO films deposited on Si substrates, *J. Crystal Growth* 193 (1998) 316-321.

[36] J.-J. Wu, S.-C. Liu, Low-Temperature Growth of Well-Aligned ZnO Nanorods by Chemical Vapor Deposition, *Adv. Mater.* 14 (2002) 215-218.

[37] V.E. Sandana, D.J. Rogers, F. Hosseini Teherani, P. Bove, M. Molinari, M. Troyon, A. Largeteau, G. Demazeau, C. Scott, G. Orsal, H.-J. Drouhin, A. Ougazzaden, M. Razeghi, Growth of “moth-eye” ZnO nanostructures on Si(111), c-Al₂O₃, ZnO and steel substrates by pulsed laser deposition, *Phys. Status Solidi C* 10 (2013) 1317-1321.

[38] M.K. Patra, K. Manzoor, M. Manoth, S.P. Vadera, N. Kumar, Studies of luminescence properties of ZnO and ZnO:Zn nanorods prepared by solution growth technique, *J. Lumin.* 128 (2008) 267–272.

[39] B.J. Jin, S. Im, S.Y. Lee, Violet and UV luminescence emitted from ZnO thin films grown on sapphire by pulsed laser deposition, *Thin Solid Films* 366 (2000) 107-110.

[40] J.F. Cordaro, Y. Shim, J.E. May, Bulk electron traps in zinc oxide varistors, *J. Appl. Phys.* 60 (1986) 4186.

Chapter 7.

Total Conclusion

One-dimensional nanostructures based on a bottom-up paradigm have attracted research interest in recent years due to their new properties. In general, it is generally accepted that one-dimensional nanostructures provide a unique system for studying the dependence of thermal, electrical and optical properties on dimensionality and the structure size. Potential applications such as building blocks, interconnects and functional units for electronic and optoelectronic devices and sensors have also been demonstrated. While efforts are under way to implement nanodevices using 1D nanowire building blocks, research on nanoscale chemical composition, structure, and size control through rational synthesis, including reproducibility, is still needed.

In this thesis, I investigated on (1) the growth mechanism of ZnS nanowires through in-situ TEM heating experiments, (2) the analysis of nanostructures using 3D TEM tomography and 3D printing, (3) the optical properties of ZnS / diamond-like carbon core-shell heterostructure nanowires and (4) the electrical characteristics of a ZnO microwire.

First, the synthesis of ZnS NWs using Ag₂S catalyst, a semiconductor material, was carried out by the VLS method using a simple Ag thin film. The

in-situ heating experiment showed that the SLV process proceeds exactly in the reverse direction of VLS, and the synthesis mechanism of Ag₂S catalyzed ZnS NW was investigated. We observe the complete dissolution of ZnS nanowires into the metal catalyst particles at their tips. We are able to consistently explain our observations using a SLV mechanism in which both evaporation at the liquid vapor interface and adhesion of the catalyst droplet to the substrate surface contribute to the overall rate. The synthesis of nanostructures between semiconductor and semiconductor by the VLS method is promising for nanodevices.

Second, in recent decades, much attention has been focused on the synthesis and development of nanomaterials, but the development of means for the complete characterization of such objects and structures took much less time. Unlike molecules and extended solid chemical structures, there are few periodic nanostructured 3D models available for 3D printing. We have shown that 3D characterization of ZnS nanostructure can be performed by electron tomography and show how electron tomography experiments can be used to determine the size of nanoparticles attached to the ZnS nanostructure I gave it. The methods and approaches described herein are becoming increasingly popular and provide access to the relationship between material properties and performance. Quantitative tomography makes it possible to perform both qualitative and quantitative properties of nanomaterials. It also applies well to

accurate morphological studies such as faceting of nanocrystals. The close agreement between morphology and chemical composition is expected to have a significant impact in the future, as it provides powerful tools for analyzing materials at the forefront of catalysis, nanoelectronics, treatment and imaging. Recent advances in electron microscopy and the development of new methodologies enable the realization of 3D models through routine electron tomography experiments with atomic resolution in the near future, but further improvements are still needed.

Third, ZnS/diamond-like carbon core-shell heterostructure nanowires were successfully synthesized by VLS growth of ZnS nanowires and a sequential rf PECVD process. ZnS nanowires were initially synthesized with a width of 70-80nm and DLC layers were continuously deposited on the surface of ZnS nanowires with a thickness of 20-30nm. The detailed analysis of the carbon structure and optical properties of the DLC with Raman and FT-IR spectroscopy confirmed that two kinds of Raman bands observed at 1550 cm^{-1} (G peak) and at 1330 cm^{-1} (D peak) indicated DLC as hydrogenated diamond-like amorphous carbon. While the IR transmittance of ZnS and ZnS/DLC nanowires was in a range of 92-99%, the ZnS/DLC nanowires exhibited an enhanced IR transmittance property by 1.1-2.8% compared to the ZnS nanowire. The heterostructure core-shell nanowire developed in the present work can be applied to a wide range of nanoscale electro-devices, which not only introduces

novel perspectives for applying DLC on a semiconductor surface and but also establishes a nanoscale fabrication technique for future nanodevices.

Forth, the influence of the contact interface on the electrical characteristics of a ZnO MW with Ag paste electrodes has been demonstrated through the formation of Ohmic-Ohmic and Schottky-Schottky contacts at the ZnO MW/Ag paste interfaces. In the case of a slow curing with increasing temperature after depositing Ag paste on the ZnO MW surface, the device exhibits linear current-voltage characteristics, indicating Ohmic contacts, whereas following the deposition and simultaneous rapid curing of the Ag paste upon deposition on a high-temperature preheated ZnO MW, the device shows a non-linear behavior, indicating Schottky contacts. This is likely due to the effect of the contact interface properties, such as interfacial defects and/or the presence of large areas of voids without Ag flakes as charge trap sites at the ZnO MW/Ag paste interfaces, which is supported by the electron microscopy and cathodoluminescence results. The charge transport mechanism for different types of Ag paste contacts to a ZnO MW was explained by energy band diagrams at the contact interface.

요약 (국문초록)

최근 나노스케일을 가지는 1차원 구조 물질(나노와이어)은 그들의 저차원적, 양자구속 효과 등에 기인하여 전기적, 광학적, 기계적으로 활발히 연구되고 있다. 이러한 관점에서 나노와이어는 적층구조, 배선, 기능 소자로서의 잠재적 응용 가능성을 위해 최근에 연구되었다. 최근 1차원 나노와이어를 가지고 나노스케일의 소자를 제작하려는 노력이 활발히 진행되고 있지만 재현성을 포함한 화학적 조성, 미세구조, 사이즈 등을 정확히 조절하기는 매우 어려운 상황이다.

본고에서는 나노와이어를 이용한 소자 제작을 위해 넘어야 할 조건 중 하나인 나노와이어의 성장 거동과 이종구조에 관해 집중하고자 한다. 여러 반도체 물질 중 최근 광학 소자로 쓰이는 2-6족 계열의 화합물 나노와이어를 중점적으로 하여 연구를 진행하였다. 나노와이어의 성장 거동과 이종구조를 연구하면서 아연황화합물 나노와이어의 성장 메커니즘, 3차원 투과 전자 현미경 단층 촬영과 3차원 프린팅, 아연황화합물/다이아몬드 카본 상을 이용한 선형 이종구조 나노와이어의 광학적 특성 그리고 산화아연 마이크로와이어의 전기적 특성 부분에 강조를 두고 그들의 기초적

성장 거동과 응용가능성을 조사하였다.

1장에서 2장까지는 최근 부각되고 있는 나노기술과 현재까지의 흐름, 나노와이어의 일반적 특성, 나노와이어의 다양한 제작 방법에 대해 서술하였다.

3장에서는 실시간 투과 전자 현미경에 의해 영상화 된 진공에서 승온 시 결정성 아연황화합물 나노와이어의 승화를 보고하였다. 지름 20-80nm의 아연황화합물 나노와이어는 제어 가능한 가열 시스템을 사용하여 가열되었으며, 그 용융 온도가 연구 되었다. 결과는 1185 °C의 벌크 녹는 점과 비교하여 나노와이어의 직경에 따라 약 400 °C의 녹는 점이 감소한 것을 확인 할 수 있었으며, 현장에서의 가열 실험은 고체-액체-기체 공정이 기체-액체-고체의 역방향으로 정확하게 진행됨을 보여 주었다. 황화는 촉매 사용하여 만들어진 아연황화합물 나노와이어의 합성 메커니즘을 조사하였다.

4장에서는 나노 물질 및 나노 구조에 적용될 때 나노 스케일에서 3차원 이미징 분야의 최근 개발에 중점 두면서 실험을 진행 하였으며, 우리는 단층 촬영법을 기반으로 한 전자 현미경 검사 기술의 최근 발전이 새로운 재료의 개발과 구조 및 특성화 사이의 차이를 메울 수 있음을 보여주었다. 특히 두 가지 새로운 3차원

접근법 인 양적 및 분석적 3차원 단층 촬영이 중요하다. 전자 단층 촬영은 나노 물질의 3차원 형태를 연구하여 나노 물질의 구조와 그 인터페이스에 대한 포괄적인 통찰력을 제공하며, 여기서, 우리는 Bright field 이미지를 이용한 전자 단층 촬영을 사용하여 은 촉매를 이용한 아연황화합물 나노구조체의 3차원 특성을 보고하였다.

4장에서는 아연황화합물/다이아몬드 카본 상을 이용한 선형 이중구조 나노와이어의 성장거동 및 광학적 특성에 관해 연구하였다. 아연황화합물/다이아몬드 카본 이중구조 나노와이어는 기상-액상-고상 방법과 고주파 플라즈마 화학기상증착법을 이용하여 합성이 되었다. 초반 부분에서는 다이아몬드 카본 상을 입히기 전의 아연황화합물 나노와이어의 지름에 따른 성장 거동에 대해서 논하였다. 합성된 아연황화합물 나노와이어는 대체로 30~120nm 정도의 지름을 가지고 성장되었으며, 다이아몬드 카본 코팅층의 두께는 20~30nm로 관찰되었다. 화학적 조성 및 구조적 접근을 위하여 집중적인 전자현미경 분석이 이루어졌다. 추가로 라만분광기를 이용하여 다이아몬드 카본 상의 특성을 분석하였으며, 합성된 다이아몬드 카본 상은 탄소성 피크인 G 피크가 1550cm^{-1} 지역대에서 발견되었고, 무질서성 피크인 D 피크가 1330cm^{-1} 지역대에서 측정되었다. 이러한 지역의 피크는 본 실험에서의

다이아몬드 카본 상이 전형적인 sp^2 , sp^3 결합을 소유함을 알 수 있다. 광학적 특성분석을 위해 합성된 아연황화합물/다이아몬드 카본 선형 이중구조 나노와이어에 적외선 투과 실험을 진행하였다. 순수한 아연황화합물 나노와이어와 다이아몬드 카본 박막이 코팅된 이중구조의 나노와이어 모두 90~98% 정도의 적외선 투과 특성을 보였으며, 2100cm^{-1} ~ 3000cm^{-1} 구간에서 다이아몬드 카본 상을 가진 이중구조 나노와이어가 1.1~2.8% 정도 증가된 투과가 관찰되었다.

6장에서는 산화아연 마이크로와이어와 은 접착제 전극 사이의 전기적 물성에 관한 연구를 진행하였다. 산화아연 마이크로와이어 표면에 은 접착제를 떨어 뜨리고 온도를 높이면서 경화 시킨 소자는 선형 전류-전압 특성을 나타내는 반면 산화아연 마이크로를 가열한 상태에서 은 접착제를 떨어 뜬 소자에서는 비선형 전류-전압 특성을 나타내는 것을 확인 할 수 있었다. 전자 현미경 및 음극선발광장치의 실험 결과 계면 사이의 결합 및 전하 트랩 사이트에 의하여 산화아연 마이크로와이어 전극과 은 접착제 전극의 접촉 계면 특성에 서로 다른 영향을 미치는 것을 보여주며, 산화아연 마이크로와이어와 다른 유형의 은 접착제 전극의 접촉에 대한 전하 수송 메커니즘을 설명하기 위해 에너지 밴드 모델이

제안되었다.

Keywords: 나노기술, 1차원 나노구조체, 나노와이어, 기상-액상-고상, 기상-액상, 성장거동, 이중구조, 다이아몬드 카본, 아연황화합물, 산화아연, 전자현미경, 3차원 단층 촬영, 3차원프린팅, 고주파 플라즈마 화학기상증착법, 라만분광법, 푸리에 변환 적외분광법, 광 발광, 음극선발광장치

Student Number 2007-20690